Fall 2009

Monte Carlo Model of Light Propagation in Tissues and the Effects of Phase Changes on the Light Intensity

Rakesh Choula
Old Dominion University

MONTE CARLO MODEL OF LIGHT PROPAGATION IN TISSUES AND THE EFFECTS OF PHASE CHANGES ON THE LIGHT INTENSITY

by

Rakesh Choula
B.Tech. May 2007, Jawaharlal Nehru Technological University, India

A Thesis Submitted to the Faculty of
Old Dominion University in Partial Fulfillment of the
Requirement for the Degree of

MASTER OF SCIENCE

ELECTRICAL ENGINEERING

OLD DOMINION UNIVERSITY
December 2009

Approved by:

_____
Ravindra P. Joshi (Director)

_____
Frederic D. McKenzie (Member)

_____
Linda Vahala (Member)

ABSTRACT

MONTE CARLO MODEL OF LIGHT PROPAGATION IN TISSUES AND THE EFFECTS OF PHASE CHANGES ON LIGHT INTENSITY

Rakesh Choula
Old Dominion University, 2009
Director: Dr. Ravindra P. Joshi

Lasers, due to their unique properties, have a wide range of applications in the medical field. For accurate laser treatments that focus on bio-tissues, prior knowledge of the amount of laser power, spot size and its irradiation time are necessary. In order to predict the effects of lasers on tissues and their bio-effects, a first necessary step is the creation of a model that can predict the temperature distributions within the tissue following laser excitation. This involves modeling light propagation through the tissue with inclusion of internal scattering, and assessment of the energy deposited by the incoming photons. The next step is the thermal diffusion of this deposited energy leading to heat production and temperature increases within the surrounding tissue.

A three-dimensional, computer-based Monte Carlo model was developed to simulate laser tissue interactions and study the effects of laser heating of bio-tissues. In this model photons were treated as a stream of neutral particles having discrete energies. This numerical approach has been used for calculating the energy deposition by the incident laser onto a heterogeneous tissue as a function of depth. Next, the heat re-distribution and corresponding changes in tissue temperature were evaluated based on the Pennes bioheat transfer equation. Suitable results and discussions of energy deposition and time-dependent temperature changes in multi-layered tissue are presented in this thesis.

Finally, for completeness, numerical implementations for including the wave-particle duality of light were discussed. The intent was to understand the effects of phase changes and include the phase information in laser photons propagation within the bio-material. A two dimensional Monte Carlo simulation model based on Huygens Fresnel principle was developed to present the effects of phase changes, and provide quantitative predictions of the laser's energy and intensity.

Dedicated to my dear parents Ramesh Choula and Sunandha Choula,

and brother Rupesh Choula

ACKNOWLEDGMENTS

I express my sincere gratitude to my advisor Dr. Ravindra P. Joshi for his continuous support, insightful advice, and motivation over the past two years. Without his constant guidance and support, it would not have been possible to complete this thesis. I feel very lucky to be associated with him.

I thank Dr. Frederic Mckenzie and Dr. Linda Vahala for serving as my committee members and for putting in their valuable time. I thank Dr. Ashutosh Mishra for his valuable suggestions and help whenever needed.

I am grateful to my parents for their unconditional love and support throughout my life and having faith in my abilities. I also thank my friends for being with me whenever needed.

My special thanks goes to my supervisor April Brecht for her support, encouragement and valuable advices. I would also like to thank my supervisors Sharon Joyner, Laurie Radford, and Dr. Joshua Behr during my school life at Old Dominion University for their support and confidence in me. My thanks also goes to the Office of Computing and Communication Services (OCCS) of Old Dominion University for providing computing services and for their quick responses.

TABLE OF CONTENTS

Chapter Page

LIST OF TABLES

LIST OF FIGURES

Figure Page

Figure Page

Figure Page

Figure Page

Figure Page

CHAPTER I

INTRODUCTION

1.1 Introduction

Lasers have unique properties such as high spatial coherence, low divergence and a very well-defined frequency (i.e., mono-chromaticity). Hence, they can propagate in a well-defined beam. Due to these properties, lasers have great potential for a number of medical applications, especially in the area of micro-surgery. The transverse electromagnetic family of modes usually describes the spatial character of the laser beam. The Gaussian beam is the most common mode, being the diffraction limit for a given wavelength. However, the beam angular characteristics are effectively randomized immediately upon entering a scattering medium such as a bio-tissue due to heavy angular deflections in the medium. Only the spatial energy distribution of the beam which can be expressed as the spot size and spot shape remains important. Beam temporal character or pulse width is determined by the operating regime of the laser [62]. A variety of regimes can produce pulses with differences in widths and peak powers. The spatial distribution of the laser power and the different operating modes is depicted schematically in figure 1.1.

Thesis document format: IEEE Transactions on Biomedical Engineering.

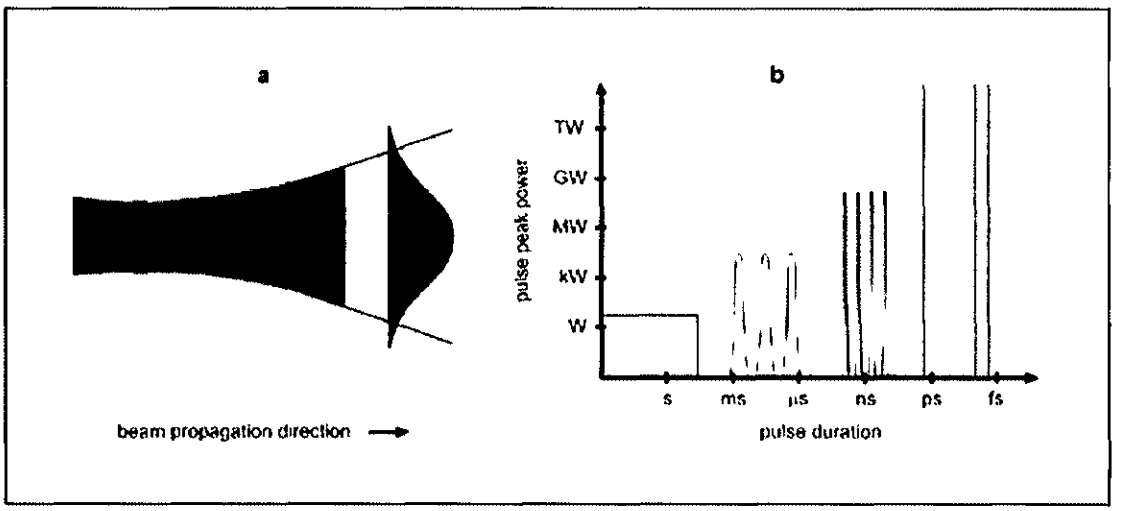

Fig 1.1. Some features of lasers. (a) Spatial parameters of laser beams are its angular (green) and radial (dark green) distributions of power. For Gaussian beams, the first depends on wavelength, waist size (w_0) and divergence (θ). The latter follows a Gaussian distribution. (b) Different operating modes: continuous wave (blue), free-run (red), Q-switched (green) and mode-locked (violet) [62].

Laser beams can be focused on to a microscopic dot with an extremely high-energy density. This is very convenient and useful for a range of medical applications (e.g., elective ablation of specific tissues, micro-surgery etc.) and many other uses (e.g., localized drilling, atmospheric remote-sensing, molecular detection using laser-induced breakdown spectroscopy, nuclear fusion, initiating photo-chemical reactions, materials processing, defense-related counter-measures etc..). In this context, it may be mentioned that a focused laser can act as an extremely sharp scalpel for delicate surgery that also cauterizes as it cuts. Today, the use of lasers is already an established practice in ophthalmology, dentistry, dermatology and other related fields. The exact details of all the effects that a laser beam can have on the tissue, and their causes and mechanisms are still elusive. The complexity of living tissue structure is reflected in the intricacy of laser-tissue interactions [62].

One of the direct consequences of laser beams interacting with bio-tissues is the localized increases in temperature. Such temperature changes can, in turn, affect several bio-physical and bio-chemical processes. For example, nerve stimulation and the firing of "action potentials" neurons can result from elevated temperatures. Some of these changes and the associated bio-effects can be predicted by modeling the processes that control and determine the temperature distributions within the tissue following excitation by incident laser beams. This involves modeling light propagation through the tissue with inclusion of its scattering, and the thermal diffusion of the heat produced due to interactions with the surrounding tissue.

1.2 Motivation

The laser as a tool is available to a growing number of physicians. Non-invasive methods, like Optical Tomography, for diagnosis in medicine have shown considerable promise and have drawn attention in recent years. Due to the tissue complex geometry, multilayer geometry of the inherent structures, and the highly scattering medium, the propagation of light is not confined to a straight line. Hence, it is difficult to analyze light transport in tissue and so computer simulations typically have to be used.

Laser treatment is based on the distribution of light (i.e., optical energy) in the tissue. Very small differences in any of the laser parameters such as beam power, a spot size, and an irradiation time can determine whether an application is efficacious or disastrous. Hence, for accurate treatment, it is necessary to have *a priori* knowledge of the effects and range of each parameter. This information usually can only be provided by mathematical models. This makes mathematical modeling and the subsequent numerical

simulations an important tool for the predictive analyses of laser-tissue interactions and their possible bio-effects.

Many methods (e.g., Kubelka-Munk [65], diffusion theory of light transport, etc..) have been developed to solve the radiative transport equation and to model the propagation of light transport in tissues. However, the above techniques involve a number of approximations and are not very accurate. By comparison, a computer-based model "Monte Carlo model of light propagation in tissues" provides more accurate results, although it is time-consuming. Also, almost all models developed and the approaches taken so far for describing laser propagation in bio-tissues have not considered phase changes in the photons as they propagate. Since photons exhibit a dual wave-particle nature, it is often important to include their phase. For example, in situations involving multiple photon sources wherein both constructive and destructive interferences could play a dominant role, the phase of each photon packet needs to be assessed and tracked. Since this is an important aspect, such phase changes during photon propagation in bio-tissues have also been taken into account and modeled.

1.3 Thesis Outline

The thesis is organized as follows:

Chapter 2 provides a background discussion and literature review. Details on the different layers of the skin tissue and the parameters affecting the propagation of light in such media are introduced. Different types of lasers and their importance in the medical field is presented by providing few applications of lasers in medicine. The Monte Carlo model, which is a more accurate technique to estimate input power and predict the

temperature rise due to the incident laser energy, is mentioned. Finally, the generated heat flow within the tissue due to diffusion and evaluation of temperature rise is discussed briefly. This latter aspect becomes necessary and important since the energy deposited by the laser into the bio-tissue immediately works to raise the local temperature. These temperature variations, in turn, influence several bio-physical, bio-chemical and bio-electrical processes. Hence, an accurate predictive model for tissue bio-effects under laser irradiation needs to include such thermal aspects at the very minimum.

Mechanical and bio-medical effects of lasers on tissues are then discussed briefly in chapter 3. This provides a broader background of laser effects on tissues. Different mechanisms of stress-wave generations and formation of cavitations bubbles, and their role in cell killings and other biological effects are presented. The formation of plasma, low-density plasmas and their chemical effects, and the implications of laser effects on biological cells and tissues are also been covered in this chapter. Thus, this part of the thesis aims to provide a brief background on some of the laser-induced effects and internal processes.

The Monte Carlo (MC) model for light propagation in tissues to estimate energy deposition by an incident laser pulse is discussed in detail in chapter 4. The details of this numerical approach are provided and the steps involved in the model calculation are given. As a part of this chapter, method to calculate the amount of incident laser energy absorbed in the tissue is modeled, and then the heat generation due to the absorbed energy and its internal distribution due to the thermal diffusion process are discussed. Later in part 2 of chapter 4, phase changes in the photon as it propagates are discussed. The necessary changes from the conventional MC model are discussed and a model is

developed for light propagation in a two-dimensional (2D) medium. The simpler 2D geometry has been used to both demonstrate the photon phase concept and to model its changes as the light propagates in the bio-tissue. This aspect is an important contribution of this thesis work.

The simulation results of the Monte Carlo models and the relevant discussions are presented in chapter 5. Chapter 6 provides the conclusions of the present work and an overall summary of the thesis. Scope for future work and possible extensions on study in this field are also discussed in this chapter.

1.4 Some Salient Thesis Contributions

This thesis work centers around the use, application, and development of the stochastic-kinetic, Monte Carlo (MC) technique to the problem of laser-pulse induced tissue heating. Some of the relevant aspects and contribution of this thesis work are outlined below.

1. The MC approach has been used and implemented for the calculation of energy deposition by an incident laser pulse on bio-tissue. In particular, the skin is taken as a specific example. This development work is important within the group as it stabilizes the capability of such MC analyses for laser-biomatter interactions. It establishes a basis on which more complicated models, intricate geometries and time-dependent bio-effects resulting from such laser-induced heating could be probed in the future.

2. The MC method has been tested for some simple cases to demonstrate its validity and accuracy of implementation. Energy deposition as a function of the tissue depth has been obtained. The numerical code developed is general, and can be applied to tissues

containing multiple layers of tissue. The only requirement is that user-specified tissue parameters be made available for the numerical code processing.

3. The energy deposition obtained from the MC code has been used to compute temperature variations and their time-dependent changes. This aspect is based on coupling a thermal-diffusion model with the energy-deposition prediction obtained from the MC. This allows for quantitative calculations of the internal temperature as a function of time.

4. Most importantly, this thesis work develops a simple model for the inclusion of photon phase information that has not been reported previously. This is a new contribution, and opens the doorway for analyses of optical phenomena involving the wave nature of light. This includes constructive and destructive interference effects, and variations in energy deposition over small spatial lengths. Such interference and intensity modulation can be expected to occur not only in instances involving multiple sources, but also in cases when scattering breaks up an incident beam into multiple paths and these individual rays then mutually interfere.

CHAPTER II

BACKGROUND AND LITERATURE SURVEY

2.1 Introduction

A laser is an optical device that emits light by stimulated emission of radiation. The characteristics of the laser make it very special and useful in a wide range of applications. It transfers light of various frequencies into an extremely intense, small, and nearly non-divergent beam of monochromatic radiation, with all the waves in phase. It produces immense heat and power when focused at close range. Laser power may range from milli-Watts (in CD-ROM drives and laser pointers) to dozens of Watts (industrial and medical applications) and over trillions of Watts (pulsed lasers in scientific and military applications). It is possible to deliver large amounts of optical (laser) energy to small targets on the surface or below the surface. The energy that is absorbed by the tissue can change its properties in a way that was found to be beneficial in many fields of medicine. Different types of lasers and their applications in the field of medicine are discussed in this chapter.

Although lasers have been used in many fields for decades, their use in fields like medicine is still relatively new and emerging. As the propagation of light in tissues is not a straight line due to its interactions with the host material, the need arises to understand the behavior of light propagation in tissues and to develop a method for modeling light transport. In order to model the laser tissue interactions, it is very important to understand the tissue layers and the parameters that effect the light propagation in the layers. This chapter introduces different layers of tissue in a human skin and the different types of lasers and their applications. The details on light transport and its simulation are based

on the Monte Carlo numerical model. A discussion of the Monte Carlo technique and its use in estimating the thermal response of tissue to laser radiation will be given in the following chapters.

2.2 Cross-section of the Tissue

Skin is the human body's largest organ, with a range of functions that support biological survival, and performs many vital roles. For example, it acts as both a barrier and a regulating influence between the outside world and the controlled environment within our bodies. It is composed mainly of three layers, namely: (a) Stratum cornea, (b) Epidermis, and (c) the Dermis.

A simple structure of skin with these different layers is shown in figure 2.1.

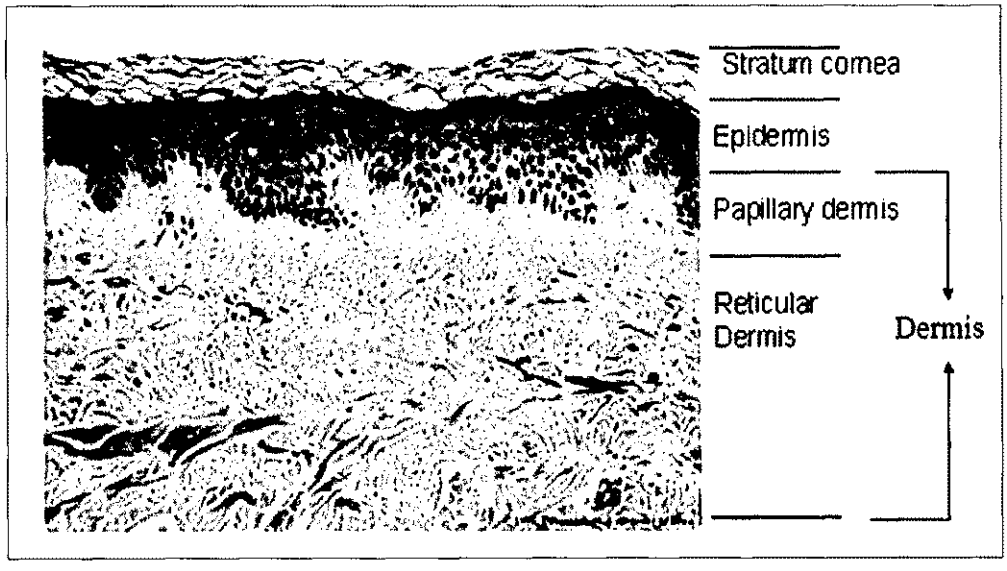

Fig 2.1. Structure of Skin [32].

Stratum cornea which is mostly composed of dead, flat skin cells practically does not absorb light, but instead diffuses it. The next skin layer is the epidermis, and it consists of cells that produce the pigment melanin. Melanin strongly absorbs light wavelengths towards the ultraviolet. Unlike epidermis, a much thicker dermis layer is richly supplied with blood and nerves. Most of the dermis is made of two proteins: collagen and elastin, providing the skin's strength and elasticity. Collagen fibers scatter light strongly. Dermis is again split in to two sub layers: papillary layer and reticular layer.

The upper, papillary layer, contains a thin arrangement of collagen fibers and the lower, reticular layer, is thicker and made of thick collagen fibers that are arranged parallel to the surface of the skin [2].

The propagation of light in each layer depends on the following parameters of a layer [3]:

i. Thickness.
ii. Refractive index. This includes details of the material above the tissue (e.g., air or a different tissue type), the tissue itself and its adjoining tissues.
iii. The absorption co-efficient.
iv. Scattering co-efficient, and
v. The anisotropy factor.

Each of the above factors is discussed in greater detail below.

2.2.1 Thickness

The extent to which light remains in a particular layer characterized by its optical properties is determined by the thickness of the layer. It takes more time for the light to

penetrate through the layer whose thickness is more, and hence, the photons experience the layer characteristics for a longer time. In a laser treatment, the depth to which light penetrates in a tissue is a critical limiting factor and is directly proportional to the wavelength of the light [4].

2.2.2 Refractive Index

When light travels from one medium to another it is either reflected or refracted as shown schematically in Figure 2.2. The bending of light towards the normal at the boundary between two media, when it passes from a rarer medium into a denser medium is called Refraction. The amount of bending depends on the indices of refraction of the two media. A larger disparity leads to greater bending.

The refractive index (or index of refraction) of a medium is a measure for how much the speed of light is reduced inside the medium. It is defined as the ratio of speed of light in vacuum to the speed of light in that medium. Thus:

$$\text{n(refractive index)} = \frac{\text{C(Speed of light in vaccum)}}{\text{V(Speed of light in medium)}}. \qquad (2.1)$$

If the angle of incidence of a ray travelling from a medium with higher refractive index to a medium with lower refractive index is greater than the critical angle, then total internal reflection occurs. Critical angle is the angle of incidence for which the refracted light travels along the boundary.

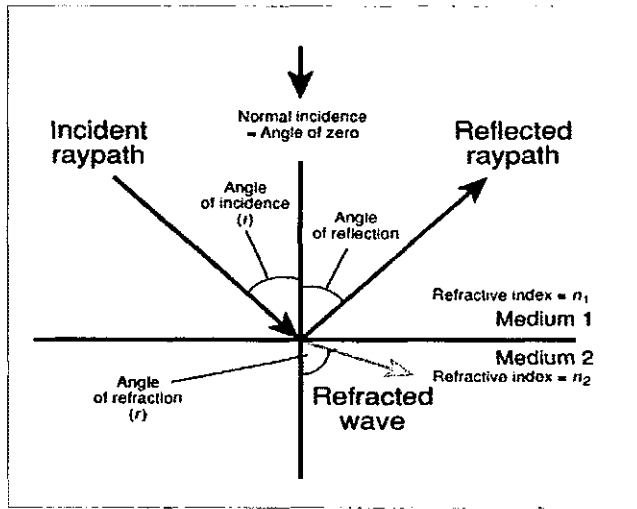

Fig 2.2. Incident, Reflected and Refracted rays [27].

The relationship between the angle of incidence and the angle of refraction, when referring to light passing through a boundary between two different media, is described by Snell's law. This law states that the ratio of the sine of the angle of incidence to that of the refraction is a constant that depends on the media.

According to Snell's law:

$$n_1 \sin(i) = n_2 \sin(r) \tag{2.2}$$

2.2.3 Absorption Co-efficient

The fraction of light absorbed per unit distance in a medium is referred to as its absorption co-efficient (μ_a). It is also defined as the probability of photon absorption per unit infinitesimal path length [3]. The standard unit of the absorption co-efficient is fraction per meter (/m).

The absorption co-efficient determines how far into a material a light of a particular wavelength could penetrate before being completely absorbed. In a medium with a low

absorption co-efficient, light is poorly absorbed and much of the incident energy can be expected to pass through as a transmitted beam. The absorption co-efficient is a characteristic of the medium (material) and also depends on the wavelength of light that is being absorbed. Figure 2.3 below shows the variation of the absorption co-efficients with wavelength for different skin layers.

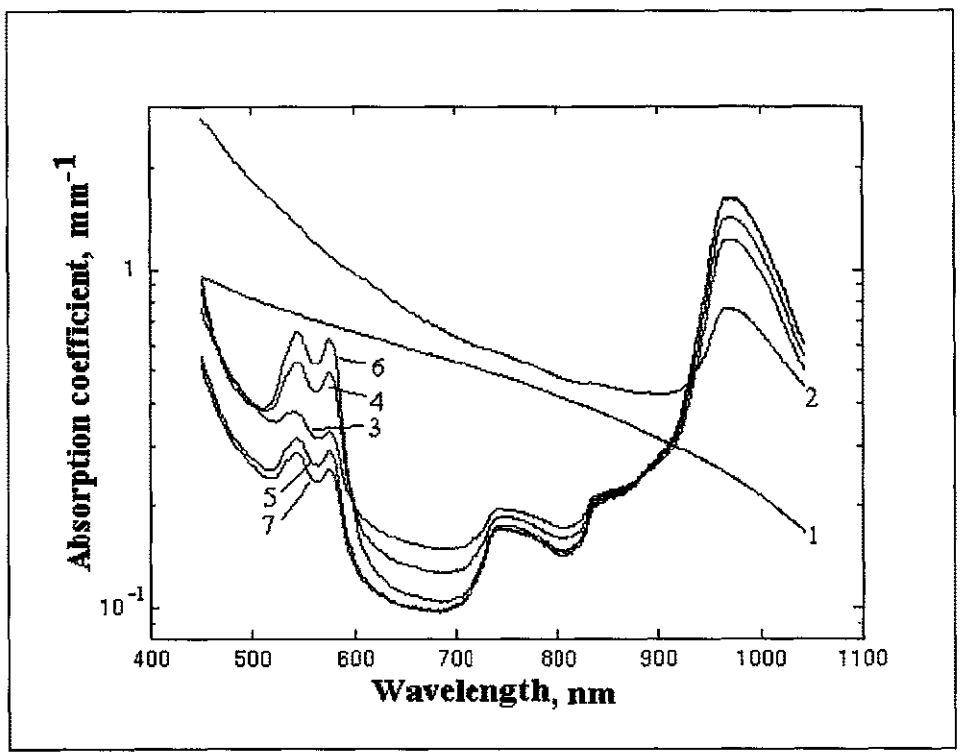

Fig 2.3. Simulated absorption coefficients of skin layers: 1- stratum cornea, 2- living epidermis, 3-papillary dermis, 4- upper blood net dermis, 5-recticular dermis, 6-deep blood net dermis, and 7-subcutaneous fat [5].

2.2.4 Scattering Co-efficient

The scattering co-efficient (μ_s) is the statistical average number of scattering events over the distance travelled by light in a material. It is also defined as the probability of photon scattering per unit infinitesimal path length. Standard unit of the scattering co-efficient is a fraction per meter (/m).

Light Scattering is the process of a photon, elastically bouncing off a microscopic obstacle. Scattering only changes the direction of propagation but the photon is not changed in the process. Scattering occurs on microscopic boundaries inside a heterogeneous material, for instance at the cellular and sub-cellular components of the tissue.

The sum of absorption co-efficient and scattering co-efficient is defined as the total attenuation coefficient (μ_t) [3, 6] and is given as:

$$\mu_t = \mu_a + \mu_s , \tag{2.3}$$

where μ_a and μ_s are the absorption and scattering coefficients, respectively.

2.2.5 Anisotropy Factor

The anisotropy factor, g, is defined as the average cosine of the scattering angle. Thus: $g = \langle \cos\theta \rangle$, where θ is the scattering angle. This parameter is a direct measure of the scattering anisotropy. This parameter 'g' varies in the [0, 1] range. Larger 'g' values imply more scattering in the forward direction [6 - 8], while a g=0 process signifies complete randomized scattering.

2.3 Laser Tissue Applications and Issues

A laser beam consists of a coherent, monochromatic and highly collimated beam of light. Focusing such a beam onto tissues results in energy absorption by molecules within the tissue. The energy absorption leads to subsequent heating, vaporization, necrosis, and coagulation. While such outcomes can be viewed as detrimental in most instances, there are, nonetheless, a number of applications and uses for such tissue-laser interactions. Here, some of the many uses of lasers arising from bio-interactions are briefly discussed below.

2.3.1 Port Wine Stains

Port Wine Stains (PWS) which often occur on the face and neck are capillary malformations that afflict 1–2% of newborns. PWS produces a reddish brown mark owing to enlarged vessels in the skin. With age, the color becomes bluish-red and the surface of the skin becomes rough. Blood inside the vessels is the target to treat PWS [9]. Many treatments have been tried to reduce the visibility of port-wine stains including freezing, surgery, radiation, and tattooing but all with unfavorable results. Without significant damage to the overlying skin, laser treatment is the sole method of destroying the cutaneous capillaries. A layered representation of the skin is presented in figure 2.4. The goal is to pass laser light through the epidermis and dermis layers, and reach the blood vessels to maximize heat generation within the blood vessels [9].

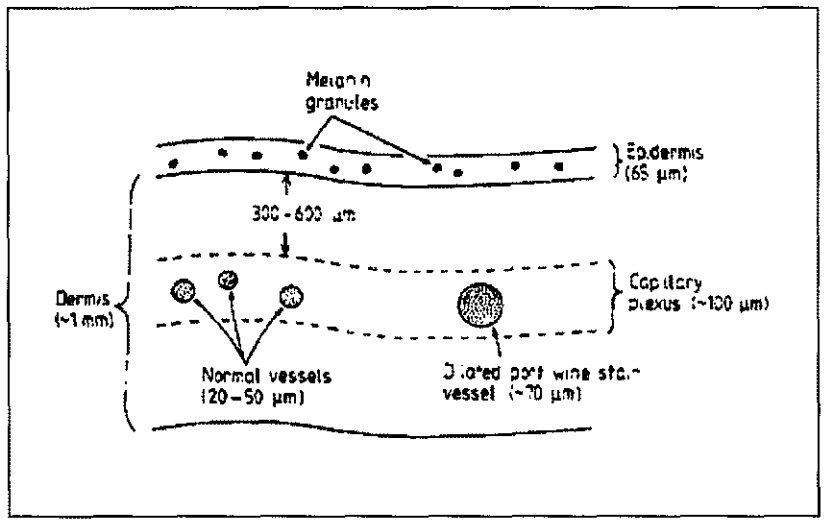

Fig 2.4. Schematic diagram of skin showing typical dimensions commonly used in mathematical models [9].

In the 1970s and 1980s, PWS was treated with argon lasers which emit light at multiple wavelengths. However, in children, serious scarring was reported with this technique, making it less attractive. Later, various lasers such as pulsed dye lasers, copper vapor lasers and long-pulsed lasers were developed for selective vascular destruction. The flashlamp pumped dye laser (FPDL), a yellow light laser, has been most successful at destroying stains in infants and young children [4, 10].

The critical limiting factor in laser treatment is the depth at which light penetrates in a tissue and it is directly proportional to the wavelength of the light. To produce thermal injury that remains confined to the targeted vessels, the laser's wavelength and the pulse's duration need to be chosen judiciously (selective photothermolysis). It is predicted from histological data that in FPDL-laser treated skin, the penetration depth for 50% energy deposition at the 585 nm wavelength is roughly 0.8 mm. The dermis of facial skin is approximately 0.6 mm deep in children and approximately 0.9 mm deep in adults.

Hence, the FPDL provides adequate penetration for cutaneous vascular lesions [4]. For optimal results, up to 10 or more treatments are necessary. Figure 2.5 shows a patient with port wine stains treated with a flash lamp, pumped-pulsed Dye laser [11]. To reduce the duration of treatment as well as the side effects, second-generation dye lasers are equipped with a dynamic cooling device (DCD) that effectively cools the skin surface and reduces pain.

Fig 2.5. A 17-year-old patient before treatment (left-hand side) and 1½ years later, after six treatments (right-hand side). The degree of lightening is 84 percent [11].

But the blood vessels in adult patients and dark PWS, may be located deep in the dermis making FPDL treatment somewhat ineffective. For the treatment of those PWS

that are resistant to FPDL treatment, frequency-doubled Nd:Yag laser (KTP laser) can be used. This can lighten the PWS quite effectively [12].

In many other vascular lesions, lasers have exceeded expectations and provided advantages compared to conventional therapies.

2.3.1 Soft Tissue Vaporization

A laser beam can be used to evaporate bacteria, viruses and fungi, by which local infections are decreased. Also, very small incisions need be made by focusing a laser beam on tissue. In soft tissue laser surgery, a highly focused laser beam vaporizes the soft tissue with high water content [13]. Of the many solid-state and diode lasers in the visible and near infrared wavelength range (600-2,000 nm), the Carbon Dioxide (CO_2) laser wavelength (10,600 nm) are highly absorbed by soft tissues containing water.

When soft tissue temperatures reaches 100° C, cell water begins to boil and then the steam escapes by disrupting the cells explosively. In the case of CO_2 laser radiation, cell debris is blown from the surface of the tissue by the force of the ejected steam. It was observed that such debris may be ignited by the laser radiation as it transects the beam. As the CO_2 laser radiation penetration depth is low and the latent heat required for vaporization acts as a heat sink limiting the temperature to 100° C in normal circumstances, the thermal damage beneath the vaporized surface is minimal. Therefore the CO_2 laser is used for tissue vaporization, either to ablate soft tissue or to incise it like a scalpel [9, 14].

Mckenzie's three zone model explains CO_2 laser damage to soft tissue [9, 14]. The model has three zones – a carbonized zone, the vacuolated zone and a coagulate zone.

The outer carbonized zone is of carbonized material. The vacuolated zone is made of cavities that have been formed by the explosive conversion of water to steam, which either escapes through fissures or condenses after the laser exposure. It has a sponge-like appearance under the microscope due to the formation of steam. The coagulated zone is formed at temperatures below 100° C. A schematic diagram of all three zones in CO_2 laser irradiated tissue is given in figure 2.6.

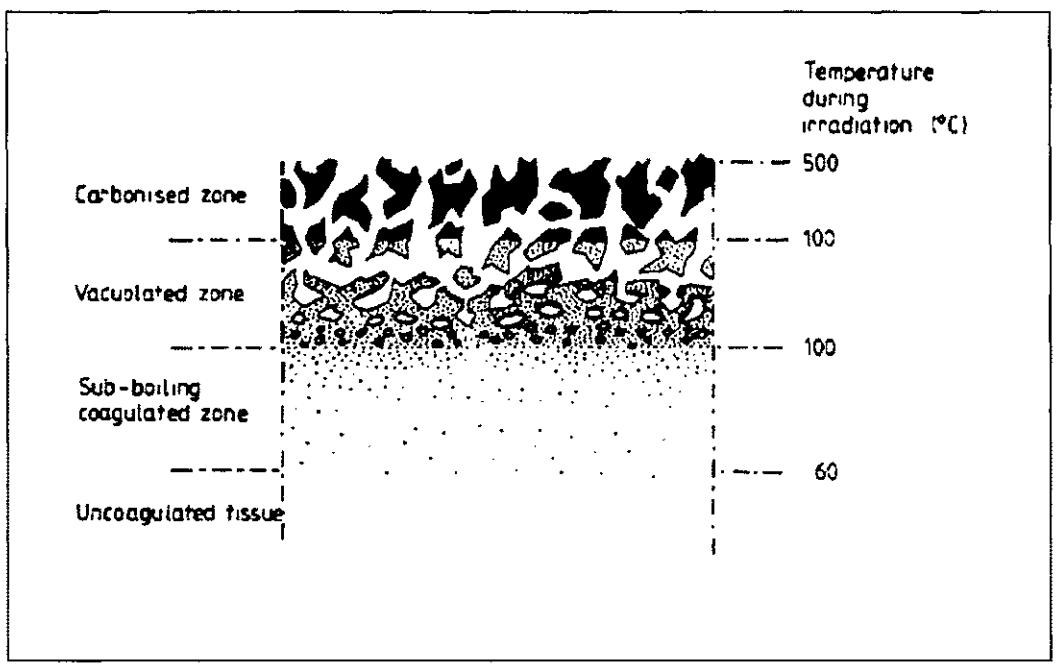

Fig 2.6. Three zones of thermal damage in CO_2 laser-irradiated soft tissue [9, 14].

The condensed or effective thickness 'ξ' is the thickness of the vacuolated zone without the bubbles, and is given by:

$$\xi = \frac{1}{\mu_a} \ln\left(\frac{c\Delta T + L}{c\Delta T}\right), \tag{2.4}$$

where μ_a is the absorption co-efficient of CO_2 laser radiation within tissue, 'c' is the specific heat of soft tissue, L is the latent heat of vaporization (=2256 Jg^{-1} for water) and 'ΔT' is the tissue temperature to rise from ambient temperature 37° C to the boiling point of 100° C.

The thickness 'ξ' depends upon the tissue's absorption co-efficient but not on the incident irradiance. It is shown that the carbonized zone's thickness and the depth of the sub-boiling coagulated zone decrease with increasing irradiance, and depend on the penetration of laser radiation through the soft tissue to some extent [9, 14].

One of the attractive features of the surgical CO_2 laser beam is that the coagulation damage beneath the excised surface of soft tissue is minimal.

2.3.3 Tumor Ablation

When radiated, the laser energy is absorbed by the molecules in the tissue with consequent heating, vaporization, necrosis and coagulation. Laser-induced thermotherapy (LITT) is a laser thermal treatment that has been used to treat tumors and other diseases of organs such as the liver, brain, prostate and breast, through high temperatures generated by the local absorption of laser energy. The LITT procedure is generally done by placing a specific scattering laser applicator into the pathological tissues in a minimally invasive manner. It is very important for laser-induced thermotherapy to exactly destroy all tumor cells within a desired region [15]. A schematic showing the mechanism of laser thermotherapy is shown in Fig. 2.7.

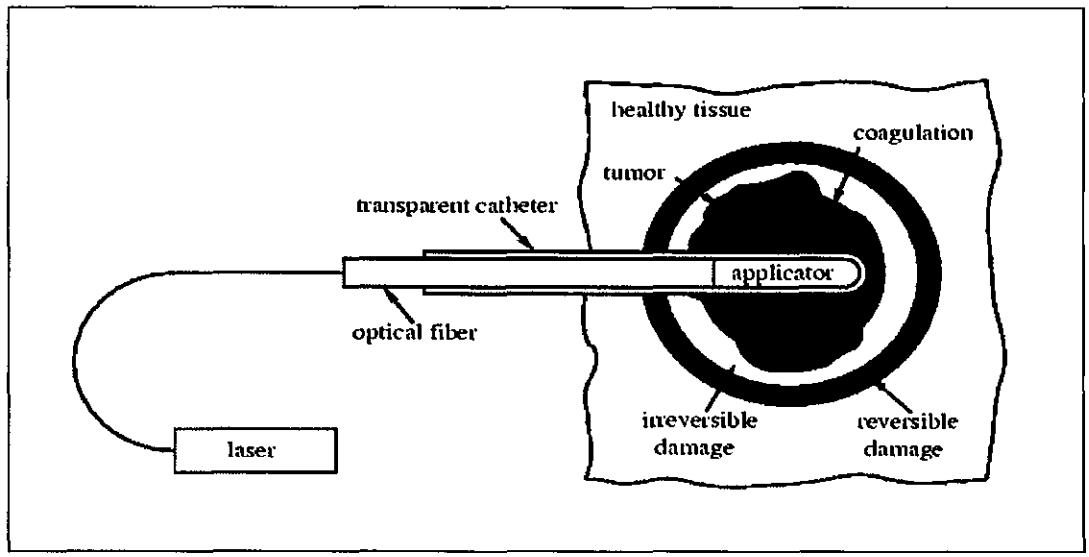

Fig 2.7. Mechanism of laser thermotherapy [28].

LITT is also referred to as Interstitial laser Photocoagulation (ILP) where intraoperative laser fibers are induced directly into the liver tumor followed by heating for 20±60 minutes. The treatment can be repeated and larger tumors can be treated by repositioning the laser fiber. Low powers (2-20 W) are used for the heating since high powers may cause rapid increases in local temperatures, resulting in tissue vaporization and extensive tissue damage [16].

The Neodymium Yttrium Aluminum Garnet (Nd:YAG) system is the most commonly used martial system for generating lasers. It has recently been demonstrated that to enhance absorbance of near infrared light, nano-particles accumulated in tumor tissue are helpful [15].

2.3.4 Photodynamic Therapy

In Photodynamic Therapy (PDT), or photoradiation therapy, laser light is delivered to the cancer site through a fiberoptic device to kill cancer cells. Depending on the part of the body being treated, certain drugs called photosensitizers or photosensitizing agents, are injected into the bloodstream or applied to the patient's skin. Over time, the photosensitizer is absorbed by cells all over the patient's body. It remains in or around tumor cells for a longer time than it does in normal tissue. Photosensitizing agents are activated by certain wavelengths, e.g., that of argon lasers. The light which is applied only to the area to be treated causes the drug to react with oxygen forming a chemical that destroys the cancer cells.

The photosensitizers should have the following properties:

1. Selective accumulation in the target malignant tissue.
2. Non-toxic to normal tissue.
3. Efficient activation with light between 600-900 nm, and
4. Fluorescence to permit the tumor's localization.

Photosensitizers such as hematoporphyrin derivative (HpD) which can accumulate in tumors are used in cancer treatment. Red light (625-632 nm) by an argon ion laser or copper vapor pumped dye lasers, or by gold vapor lasers (628 nm) have been used for PDT. The excitation probability of HpD as a function of wavelength is shown in figure 2.8.

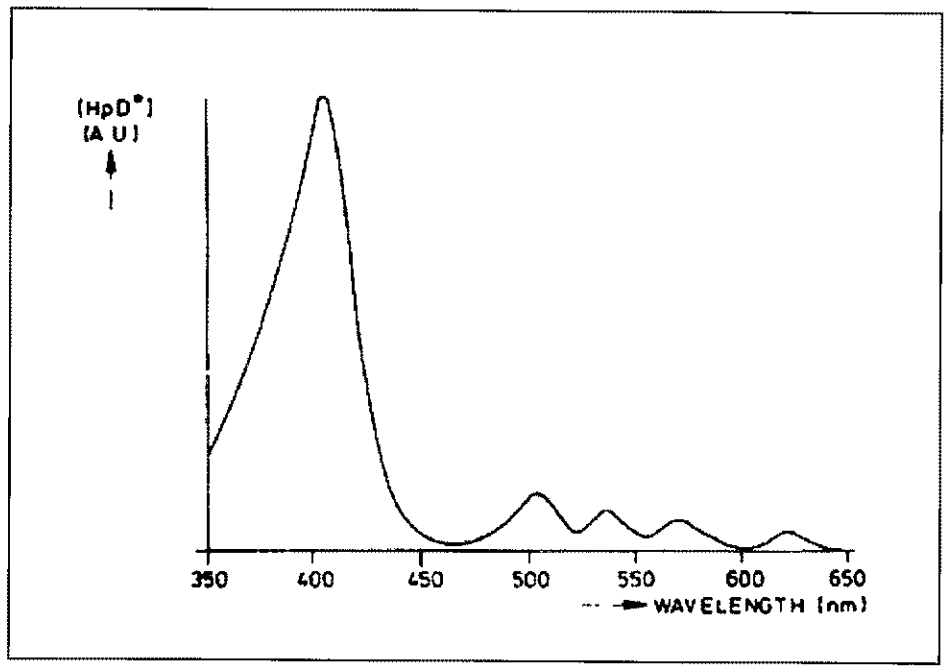

Fig 2.8. Excitation probability (in arbitrary units) as a function of wavelength for HpD [17].

From the figure it is clear that the most efficient wavelength to excite HpD is around 405 nm. However, for PDT the light should be able to penetrate into the malignant cells. As the violet light (405 nm) can only superficially penetrate into the tissue, it is not suitable for PDT. Therefore red light (625-632 nm) which penetrates much more deeply into tissue is widely used for PDT [17].

The main advantage of PDT is that the cancer cells can be singled out and destroyed while most normal cells are spared. PDT may also work by destroying the blood vessels that feed the cancer cells and by alerting the immune system to attack the cancer. PDT is sometimes used to treat cancers and pre-cancers of the esophagus, and certain kinds of lung cancer that can be reached with endoscopes.

2.3.5 Laser Angioplasty

Laser angioplasty is a technique that opens coronary arteries blocked by plaque which is the build-up of cholesterol, cells and other fatty substances in an artery's inner lining. Figure 2.9 shows the blood flow in a normal artery and in an artery that has been narrowed due to plaque.

In Laser angioplasty, a thin, flexible plastic tube called a catheter with a laser at its tip as shown in figure 2.10 is inserted into an artery through a cut in the upper leg or the arm. It is then advanced through the artery to the blockage in the coronary artery. By positioning and emitting pulsating beams of laser light, plaque can be vaporized.

This procedure has been used alone and with balloon angioplasty. In the latter case, the balloon is inserted first to attack the hard plaque. In order to keep an artery open after it has been widened, stents are used often these days. Depending on where the blockage is, the number of blockages and extent of the blockages, laser angioplasty with or without stents or with balloon angioplasty can be used. Figure 2.11 below shows a blocked artery before and after angioplasty with two stents.

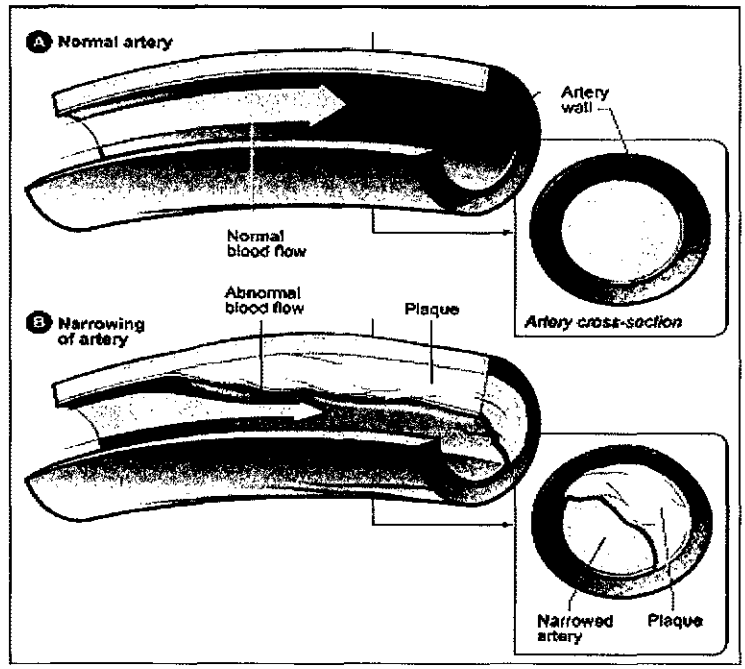

Fig 2.9. (a) Normal artery without any plaque, and (b) Narrowed artery due to plaque [29].

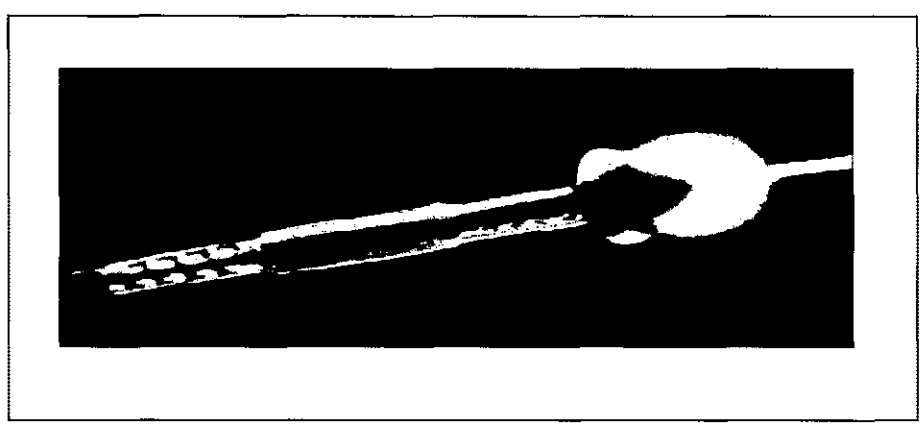

Fig 2.10. Laser Catheter [30].

Fig 2.11. A 94% blocked main artery (left), after laser angioplasty and 2 stents (right).

Lasers which create microscopically precise cuts without thermal injury, such as argon laser and excimer laser are used.

2.3.6 Tissue Welding

Laser welding of biological tissues is a soft thermal treatment in which laser energy is used for wound closure. Laser radiation is absorbed by the tissue either directly from its principal absorbers such as water or from exogenous chromophores applied topically to the wound area. Upon heating new bonds are formed between adjacent molecules and are stabilized upon cooling. Figure 2.12 shows the thermal changes in an extracellular matrix of the connective tissue when temperature is raised, leading to wound welding.

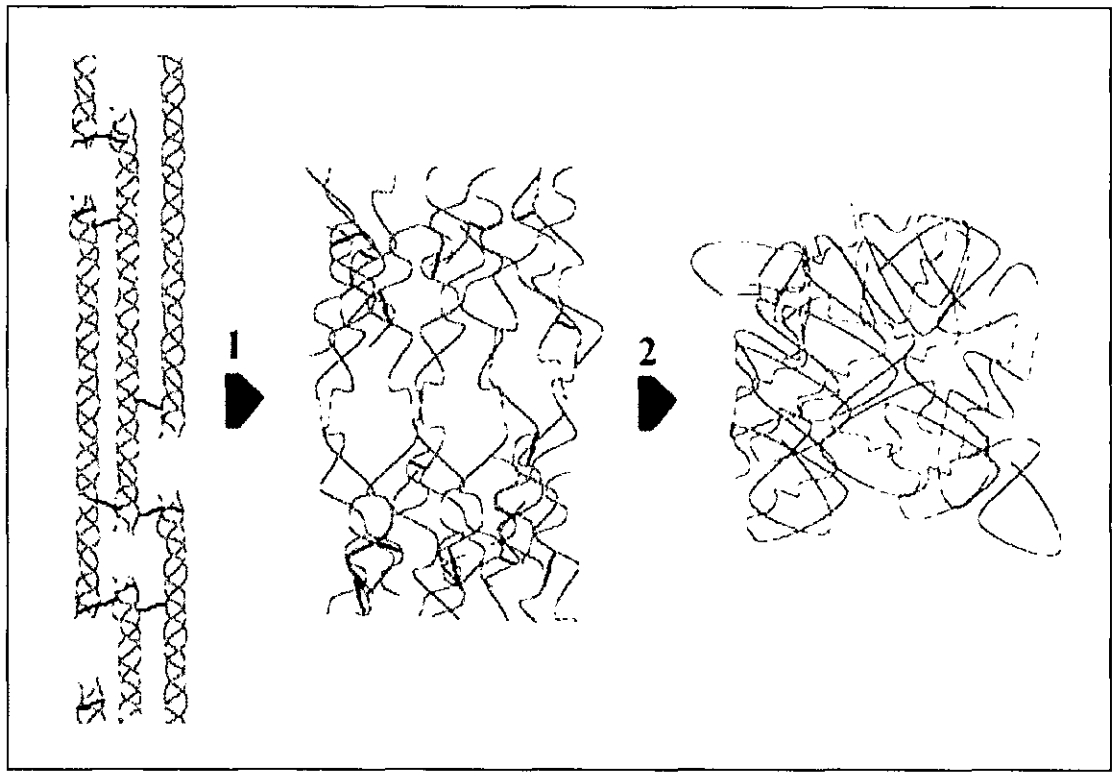

Fig 2.12. Structural modifications induced in fibrillar collagen of connective tissue by temperature rising. Normal triple helix collagen molecules are packed in a quarterstaggered manner and connected by covalent bonds to form a collagen fibril (*left*). When heat is applied, hydrolysis of intramolecular hydrogen bonds occurs, which results in the unwinding of the triple helices (*middle*). The first step (1) leads to a shrinkage effect parallel to the axis of the fibrils. At higher temperatures, covalent cross-links that are connected to collagen strands break, thus resulting in a complete destruction of the fibrillar structure (*right*) and causing the tissue's relaxation (step 2) [18].

The strength of bonds formed depends on the extent of laser radiation. If it is used excessively, there may be an undesired thermal damage in the surrounding area and the strength of the weld may be poor. On the other hand, if the energy density is too low, no welding effect is achieved. Based on the light emission parameters (wavelength, time emission mode, specific light density, penetration depth into tissue, etc.) and the type of absorber in the tissue (exogenous or endogenous chromophores), light dosimetry is calibrated.

Figure 2.13 below shows the most common technique used in tissue welding. The supporting needle shown in the figure is removed when the tissue is welded.

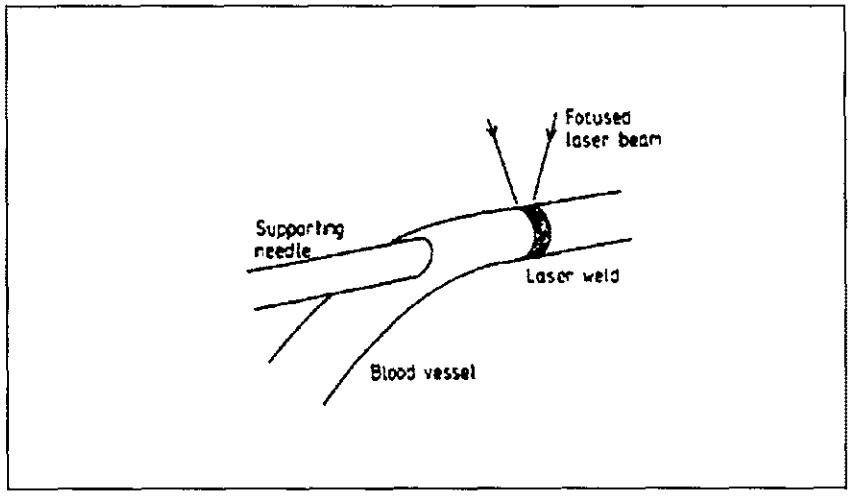

Fig 2.13. Commonly used technique for laser anastomosis of blood vessels [9].

Laser tissue welding has several advantages compared with conventional closure methods. These include reduced operation times, fewer skill requirements, watertight bonding and decreased foreign-body reaction which can lead to reduced inflammatory responses, faster healing, increased ability to induce regeneration and an improved cosmetic appearance [17]. It is suited in applications in which sutures and staples cannot be used, such as in microsurgery, laparoscopy or endoscopy, or for the treatment of extremely thin tissues. As laser welding develops its potential to form complete closures, it can be used for making immediate watertight anastomosis, which is important in the case of vascular, genito-urinary tract and gastrointestinal repairs. Also, a watertight closure prevents the exit of regenerating axons and the entry of fibroblasts.

Different laser types with wavelengths exhibiting high optical absorption in water have been used for laser tissue welding. Infrared and near-infrared sources include carbon dioxide (CO2), thulium–holmium–chromium, holmium, thulium, and neodymium rare-earth-doped-garnets (THC:YAG, Ho:YAG, Tm:YAG, and Nd:YAG, respectively), and gallium aluminium arsenide diode (GaAlAs) lasers. Visible sources include potassiumtitanyl phosphate (KTP) frequency-doubled Nd:YAG, and argon lasers [18].

More recently, an infrared temperature feedback control system is being used to monitor the surface temperature. For the control of energy delivery, it is very important to monitor the surface temperature. Such an arrangement is shown in figure 2.14 below.

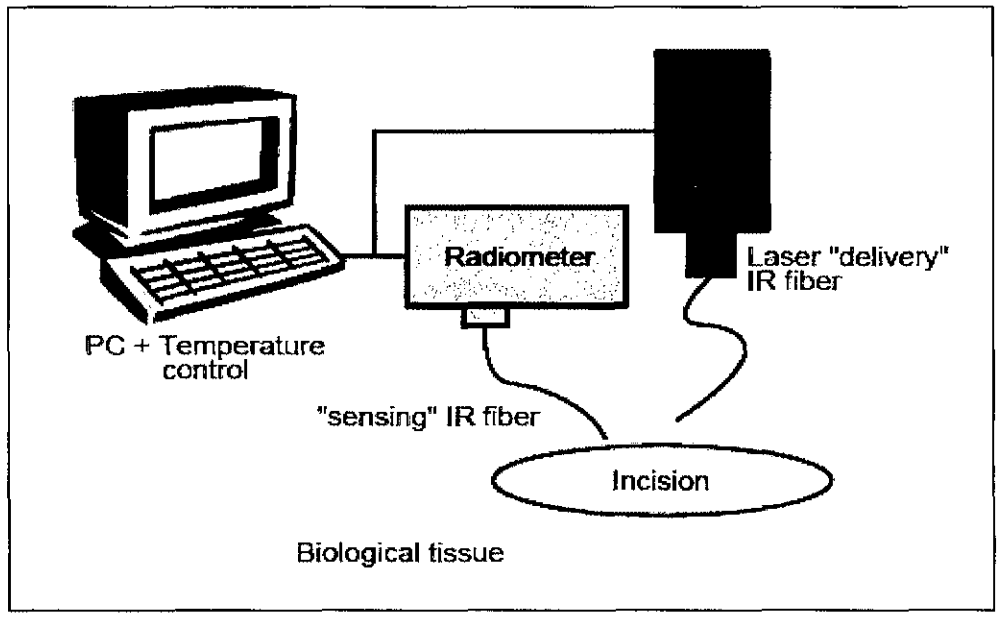

Fig 2.14. Laser welding with feedback control system [31].

This welding system has two optical fibers: one is used to carry laser energy to heat a spot on tissue and the other is part of a fiber optic radiometer that is used to determine the exact temperature of the heated spot. Using the signal obtained from the radiometer, the computerized system is used to control the temperature within 5 degrees.

2.3.7 Hyperthermia and Thermal Damage

Hyperthermia is a heat therapy used in tumor treatment, often in conjunction with chemotherapy or radiation. Hyperthermia acts as a cytotoxic agent at temperatures higher than 41° C because cells die after heating in a time-dependent manner. In hyperthermia, cells that are heated to temperatures ranging from 40° C to 45° C can sustain reversible injury that becomes irreversible (death) after exposure from 25 minutes to several hours, depending on the tissue type. Laser light transmitted through thin flexible fibers directly into the tumor's center can be used to raise the temperature and treat the cancer cells in the internal organs [19].

Lasers such as Nd:Yag laser which can penetrate to a depth of 4-7 mm, are being used to raise the temperature of living skin containing the diseased tissue from its normal level to about 45° C. Nd:Yag hyperthermia is especially useful when basal cell carcinoma (BCC) is located in areas such as the eye and the nose, and are harder to treat by the other modalities. It is an efficient, easy, bloodless alternative procedure to treat BCC. Figure 2.15 shows the effect of laser hyperthermia on the nodular BCC. Laser-assisted hyperthermia has the advantage of not leading to edema and erythema, and is not associated with excessive tissue damage. Advantages include tolerable burning sensation and pain and therefore no need for local anesthesia [20].

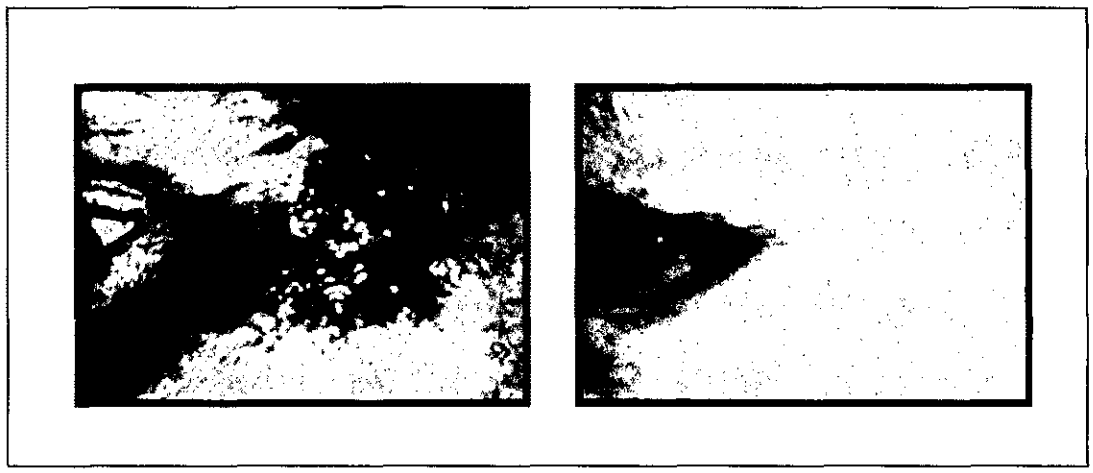

Fig 2.15. Nodular BCC before treatment (left), Complete disappearance after 4 sessions of Nd:Yag laser hyperthermia (right) [20].

2.3.8 Dental Applications

The laser's heat energy is being used to improve dental procedures by controlling power output and the duration of exposure on the tissue (whether gum or tooth structure). Lasers are helpful in cracking, melting, charring, fissuring or crazing of tooth surfaces and in inefficient material removal [21]. When used for surgical procedures, lasers act as a cutting instrument or as a vaporizer of tissue that is being contacted. When used for curing a filling, they assist the process of strengthening the bond between the filling and the tooth. Lasers enhance the effect of tooth bleaching agents, when used in teeth whitening procedures.

The lasers that are most frequently associated with dentistry are the carbon dioxide lasers, the Nd:YAG lasers, and the argon lasers (either ArF or argon flouride) [22]. The laser wavelengths such as holmium: YAG, or Ho:YAG, neodymium:yttrium- lithium-fluoride or Nd:YLF and Er:YAG are also used in dentistry. The development of high-

average-power, high-repetition-rate, sub-picosecond lasers has refocused interest in laser treatments, due to the highly efficient tissue ablation and minimal collateral damage offered by using such lasers in the appropriate parameter regime [21].

Recently Er:YAG laser operating at a wavelength of ~2.9μm, has begun to be used in conjunction with a water spray. Waterlase uses laser energy and a gentle spray of water to perform a wide range of dental procedures – without the heat, vibration and pressure associated with the dental drill. The water spray not only helps in cooling the tooth (treated area) during ablation, but it also increases the efficiency of the ablation. Figure 2.16 demonstrates the application of waterlase on the tooth.

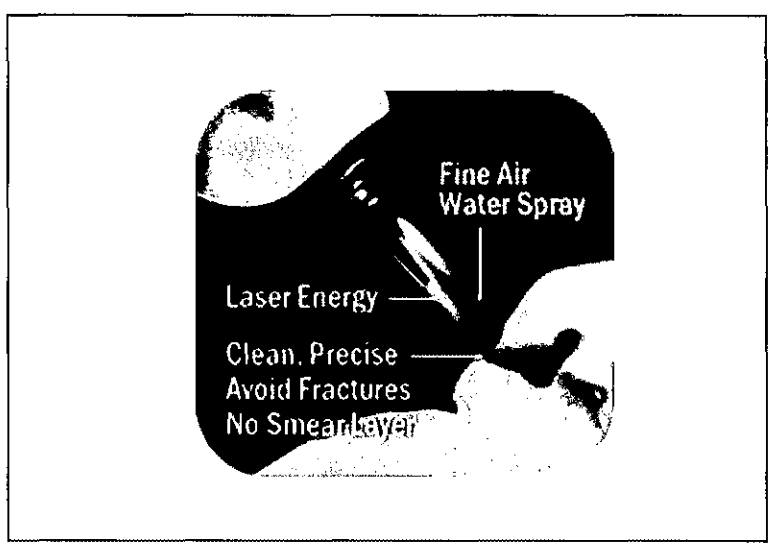

Fig 2.16. Waterlase on a tooth.

Advantages of using the waterlase instead of a drill are given below.

- The laser's pinpoint accuracy is precise enough that more healthy teeth may be preserved, during cavity removal.
- As most dental procedures can be performed with no pain, there is no need for anesthesia.
- The method effectively performs numerous soft tissue (gums) procedures with little or no bleeding, leaving behind stitches and healing packs.
- The method avoids many common problems of the dental drill, including cracks in the teeth from the vibration and rapid turning of the drill burs, which can weaken your teeth, creating future problems.
- The waterlase sterilizes as it cuts, leaving less chance for bacterial contamination.
- A dental laser maximizes the bonding of tooth-colored fillings, allowing them to last longer.
- The waterlase can effectively treat canker and cold sores, thus killing the viruses that cause cold sores and allowing rapid healing.

2.4 Different Types of Lasers

There are various kinds of lasers available today depending on the source producing the laser. Each of them has a specific range of utility, depending on its wavelength and penetration. Various types of lasers and their positions in the electromagnetic spectrum are shown in figure 2.17. The laser medium can be a solid, liquid, gas or semiconductor.

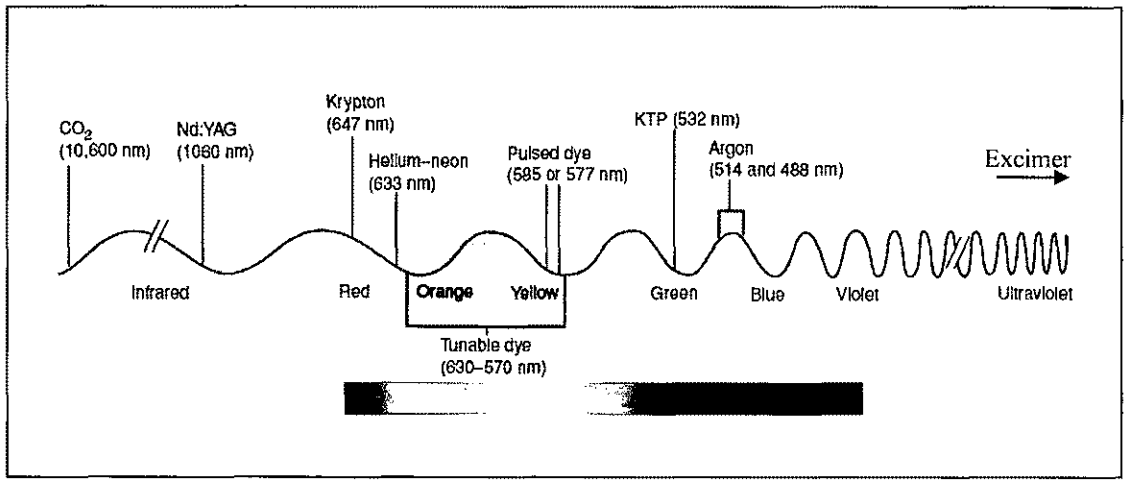

Fig 2.17. Relative positions of various types of lasers on the electromagnetic spectrum [54].

In this section only a few of the commonly used lasers are discussed.

2.4.1 Neodymium: Yttrium-aluminum-garnet (Nd:YAG) Lasers

Nd:YAG laser is a laser whose active medium is a crystal of yttrium, aluminum, and garnet doped with neodymium ions. It can be used to produce very high powers and has the capability to reach deeper layers of skin tissue. It has a wave length of 1064 nm. It can be used to cut or coagulate tissue and also it can be effective for laser hair removal and treatment of vascular lesions including leg veins. The Q-Switched Nd:YAG is used for the treatment of tattoos and certain pigmented lesions. Nd:YAG has a second transition at 1320 nm, whose wavelength can be used for tissue heating, soft tissue coagulation, and endovascular treatment of varicose veins.

Neodymium-YAG lasers are used in pulse mode in laser oscillators for the production of a series of very short pulses for research with femtosecond time resolution.

2.4.2 Carbon Dioxide (CO_2) Lasers

The carbon dioxide laser is a gas laser which emits an infrared beam at 10,600 nm. It is the most efficient laser (30% efficiency) and is capable of continuous output powers more than 10 kW.

It is strongly absorbed by water. As the water constitutes 80% or more of soft tissue, the CO_2 laser is used as a cutting or vaporizing tool to incise or ablate soft tissue. Some of the uses of CO_2 lasers are:

- Removal of skin lesions such as moles, warts, and keratoses,
- Use as a laser scalpel in patients or body areas prone to bleeding,
- Non-contacted removal of tumors in neurosurgery,
- Cosmetic ablative laser resurfacing for photoaging and wrinkles, and
- Shaving, dermabrading and resurfacing scars, rhinophyma and skin irregularities.

2.4.3 Excimer Lasers

The term Excimer is a shortened form of 'excited dimer', denoting the fact that the lasing medium in this type of laser is an excited diatomic molecule. Excimer lasers produce intense output at very short wavelengths which can be focused to a very small spot diameter (~ 40 times smaller than the CO_2 laser beam with the same beam quality) in the Ultra-Violet (UV) spectrum in short pulses. The excimer lasers are usually formed by inert gas atoms and halogen atoms which are bound in excited states. The lasers in this family are XeFl (351 nm), XeCl (308 nm), KrF (248 nm), KrCl (222 nm), ArF (193 nm), and F_2 (157 nm) [23].

As the emitted wavelengths are very short, each individual photon carries a large amount of energy and hence is useful in breaking the bonds between molecules in material that absorbs the radiation. Each pulse contains a large number of photons, since it has a very high peak power. Thus, the laser can be used as a perfect cutting tool for almost every material. These lasers are capable of:

- Cutting biological tissue without harming the surrounding healthy tissue,
- Correcting vision disorders – used to cut very delicate layers from the outer surface of the cornea during eye surgery,
- Photolithography - Material processing at a very high degree of accuracy, and
- Marking on products – used to mark on all kinds of materials, such as plastics, glass, metal, etc.

2.4.4 Pulsed Lasers

Pulsed lasers emit light in the form of optical pulses with "on" and "off" periods. They are used in applications where a large amount of heat is required in a very short time. There are a number of methods to achieve pulsed mode of operation. Q-switched lasers emit nanosecond pulses; a modelocked laser emits extremely short pulses with durations in picoseconds or femtoseconds domain. In the UV spectral region nanosecond pulses are generated by excimer lasers. Pulsed pumping is also used to emit pulsed lasers where the laser material is pumped with a source that is itself pulsed. Pulsed pumping is generally used with dye lasers.

The excimer laser and the copper vapour laser are only operated in pulsed mode but never in the CW mode. Depending on the pulse duration, pulse energy, pulse repetition

rate and wavelength required, different types of pulsed lasers are used. The pulsed dye laser is one among them.

2.4.5 Pulsed Dye Lasers

This type of laser uses a liquid dye (Rhodamine 64) and produces yellow light at 577-585 nm which is delivered in short flashes. As it is absorbed by the hemoglobin present in the blood, it is especially useful for the treatment of vascular lesions like spider veins, strawberry birthmarks and port wine stains especially in infants and children, nevus flammeus, hemangiomas, keloids and hypertrophic scars. It is also used to treat pigmented nevi.

Long pulsed dye lasers are used to treat fine veins, telangiectasia and blushing.

2.5 Laser-Tissue Interaction Models and Brief Overview of Quantitative Assessment Techniques

For the analysis and optimization of the parameters governing planned laser surgical procedures, the modeling of laser–tissue interactions become very useful. In modeling of laser tissue interactions, the irradiance distribution within the tissue first needs to be determined. Next, the temperature distribution in the tissue caused by the laser energy deposition has to be obtained quantitatively by solving the bioheat transfer equation. Lastly, thermal damage is predicted from this spatial and temporal temperature distribution [7]. Usually, if the local temperature increases due to the external laser irradiation and exceed a critical threshold, then multiple outcomes such as protein denaturation and bio-mass destruction result.

2.5.1 Heat Deposition in Bio-Tissues -- Monte Carlo, Green's Function and Analytical Methods

A variety of models have been developed to estimate thermal response of tissue to laser radiation. Many of these models are based on analytical solutions. Typically the models incorporate the Green's function, or if simple closed form solutions cannot be obtained, then numerical solutions involving the finite difference method or the finite element technique are used.

The advantages of analytical solutions are usually their transparencies. Besides, it is much easier to predict and evaluate scaling effects or the impact of changing parameter values. The numerical solutions, on the other hand, are harder to interpret or gauge solutions. However, they can be programmed by just using a Personal Computer (or sometimes even a pocket calculator) with a few scientific functions [7].

Monte Carlo methods have been used to model systems and solve problems where obtaining analytical solutions to physical questions becomes too complex. Solutions to these problems are obtained by constructing a stochastic model (e.g., for simulating the energy transfers from incoming photons due to continuous interactions with the host tissue) in which the expected value of a random variable is used to represent a physical parameter. For example, the path length of incoming photons between collision events with the tissue mass may be a random variable. In the Monte Carlo method, the photon is treated as a neutral particle, instead of propagating wave entity. This method simulates the random walk of individual photons from one interaction to another. The method is based on a set of rules that govern the movement of a photon in tissue. The key decisions

that are in this stochastic simulation scheme include: (i) determination of the mean free path leading up to a scattering or absorption event, and (ii) the scattering angle.

This method is basically statistical in nature and requires a computer to calculate the propagation of a large number of photons. The number of photons required in a simulation depends on the precision needed for reducing the statistical deviations below a tolerable limit, and the spatial or temporal resolution desired [7].

To find the internal energy distribution from light beam incident onto a medium, the Green's function may also alternatively be used. The Green's function obtained for the heat flow equation is independent of the source term [24] and depends only on details of the tissue, its geometry and heterogeneous material parameters. Physically, this technique relies on the following concept: as unscattered light propagates through the medium, it is scattered and becomes diffuse. The initial scattering event acts as a source of the light's diffusion. The Green's function describes the distribution resulting from a point source of diffuse light. Since the unscattered light decays exponentially with increasing depth according to Beer's law, the Green's function for an irradiation point on the surface may be obtained by convolving the Green's function with the proper exponential function. Again using superposition, the response for an arbitrary source distribution can then be obtained by adding the contributions of all point irradiances [7]. Based on the Greens function, many models like finite difference model have been developed.

2.5.2 Introduction to Pennes Bioheat Equation and its Parameters

In 1948, Pennes proposed a model to describe the effects of metabolism and blood perfusion on the internal temperature distribution. Details of this will be given in Chapter

4. Briefly, the Pennes bioheat equation is based on the heat diffusion equation and is routinely used as an approximation for heat transfer in biological tissue [25]. The bioheat equation was deduced from power balance arguments considering the changes associated with the heat source term Q, including the metabolic rate of tissue, Q_m the thermal energy transformed from chemical energy caused by partial metabolism, the blood flow term $W_bC_b(T_p-T)$ which denotes the thermal energy transmitted from in/out controlled volume blood, and the volumetric heating Q_r. For heat incident only on the skin surface, Q_r can be considered to be 0.

The Pennes bioheat transfer equation is given as:

$$\nabla.[K\nabla T(r,t)] + W_b C_b (T_b - T) + Q_m + Q_r = \rho C \frac{\partial T(r,t)}{\partial t} \quad . \tag{2.5}$$

where K [W/(m.K)] is the thermal conductivity, W_b [kg/(m^3.s)] is the blood perfusion rate, C_b and C [J/(kg.K)] are the specific heats of blood and tissue, T_b and T (^oK) are temperatures of blood and tissue, respectively; Q_m (W/m^3) is the metabolic rate of tissue, Q_r (W/m^3) is the volumetric heating rate, and ρ (kg/m^3) is the tissue density [33].

2.6 Summary

In this chapter, different layers of skin tissue and the parameters that effect the propagation of light in the tissue have been introduced. The power of laser energy has been demonstrated by exhibiting few applications of the laser in the medical field and also few commonly used lasers and their properties have been presented. It is shown that providing enough input power at a particular wavelength is the key in laser treatment as

excess heat causes undesired thermal damage; on the other hand, insufficient heat does not affect the tissue. In order to estimate the input power and predict the temperature rise due to the laser heat within the irradiated tissue, a model is needed. Monte Carlo model serves as the starting point for evaluating the energy deposition by the incident laser into the tissue. This technique has been introduced. Next, some of the other aspects relating to heat flow and evaluation of rising internal temperature have been briefly mentioned. A more detailed discussion of the Monte Carlo model along with heat related temperature increases within the tissue is presented in the next chapter.

CHAPTER III

MECHANICAL EFFECTS OF LASERS INCIDENT ON TISSUES

3.1 Introduction

Laser-induced mechanical effects in tissue pertain to ophthalmology as in photodisruption (or phacoemulsification) and urology, and have been subjects of extensive research. These procedures are promoted by optical breakdown and the subsequent formation of plasma, bubble and shock waves. Shock-wave generation, for example, has been viewed as a possible therapeutic recourse for kidney-stones based on the "Extracorporeal Shock Wave Lithotripsy."

During the focusing of a Q-switched laser pulse, water absorbs energy from the incident photons and vaporizes almost instantly to form plasma clouds. This sudden plasma formation generates a spherical underwater shock wave. For very short laser pulse duration, free electrons absorbing laser light energy are further accelerated due to the process called 'inverse Bremsstrahlung,' thus promoting the process of shock formation [56]. Inverse Bremsstrahlung is a well-known mechanism for accelerating electrons through the absorption of radiative energy. The propagation of such shock-waves and their biological effects are governed by the mechanical properties of the irradiated tissue. Shock-wave therapy was developed for the revascularization of cerebral embolism, drug delivery and other therapeutic methods. Extracorporeal shock-wave lithotripsy (ESWL) succeeded in noninvasive removal of urinary tract stones [56].

The salient feature of a shock wave is a discontinuity in stress (pressure), density and particle velocity (the displacement velocity of the medium behind the shock front), and internal energy. Stress waves affect the linear and nonlinear acoustic properties of the

medium through which they are propagating. The linear attenuation attenuates the high-frequency components, thus decreasing the bandwidth with corresponding increase in the rise time. On the other hand, the rise time is decreased due to the nonlinear properties of the medium and the nonlinear behavior of the particle velocity which depends on the stress. This nonlinear behavior causes the leading edge of the stress wave to steepen, thus forming a discontinuity (shock wave). Thus, shock waves are waves with high peak stress and these waves propagate at speeds substantially higher than the sound velocity [55].

Stress waves have been successfully applied to medical therapy. They can also induce deleterious effects during medical procedures of high power and short pulse lasers; hence, care needs to be taken. Some of the deleterious effects include tissue fracture, localized cell killing, decrease in cell viability and increase in the permeability of the plasma membrane. These have also shown promise for use in drug delivery and gene therapy.

3.2 Generation of Stress Waves

Laser-induced stress waves can be generated by one of the following mechanisms: optical break down, ablation, or rapid heating of an absorbing medium (thermoelastic generation) [55]. Details of these various processes are given below.

3.2.1 Plasma-Induced Stress Waves

The high field intensity from a Q-switched or mode-locked laser pulse causes ionization (optical breakdown) of the medium and plasma formation. The generated plasma expands rapidly due to the high temperature and pressure of the plasma (mainly

the high-energy mobile electrons), thus creating a high pressure front. As the plasma's temperature decreases, the plasma expansion slows down and the high pressure front separates to form a shock wave. The localized bubble continues to expand until the pressure reduces to the point that it cannot support the hydrostatic pressure. Subsequently, the bubble implodes under the external pressure of the liquid. The temperature and pressure inside the bubble rise again, and thus a second shock wave is formed following a second explosion. The generation of a shock wave and the bubble generated by optical breakdown is shown in figure 3.1. Thus, the process is dynamic and usually involves a series of shock-waves.

Fig. 3.1. Generation of the shock wave and bubble expansion generated by optical breakdown. A pulse from a Q-switched Nd:YAG laser (pump), 1.064 pm, 6-ns pulse duration, and 1 mJ pulse energy, was focused onto water to produce plasma. A second pulse (probe), 532 nm, was used as a strobe flash to photograph the event. The pump pulse is incident from the right. The time delay between pump and probe pulse is indicated on each picture. Bar scale equals 100 pm [55].

3.2.2 Ablation-Induced Stress Waves

Tissue ablation involves the decomposition of polymers into small fragments caused by the incidental ultraviolet radiation. These fragments move away from the surface at high speed, almost like projectiles ejected from the tissue. Though the amount of the material removed is small, stress waves of high peak stress can be generated through the imparted recoil momentum.

3.2.3 Thermoelastic Stress Generation and Stress-Induced Bubble Formation

When an absorbing medium is irradiated to short laser pulses, rapid thermal expansion of that medium occurs and the thermal expansion propagates as a stress wave. In general, the thermoelastically generated stress waveform is complex and depends on the geometry of the source, the laser beam profile, the laser pulse duration (T_L) and the acoustic transit time (T_S). The acoustic transit time is defined as the optical penetration depth divided by the sound velocity. The waveform also depends on the surface boundary conditions when the source of the stress wave is on the tissue surface. The rise time of the stress waves is determined by the relative values of T_L and T_S. If $T_L << T_S$, then the rise time of the stress wave is equal to T_S; else if $T_L > T_S$ the rise time of stress wave follows the rise time of the laser pulse. Thus, by varying the wavelength of the laser or by the absorber stress, waves can be generated with adjustable rise times to control the optical penetration depth.

The trace of thermoelastically-generated stress waves with different rise times is presented in figure 3.2 after Lamb et al. [59]. These stress waves were generated by

tuning the free electron laser (FEL) to 3.21 pm and 3.78 pm, respectively, and are normalized to maximum stress values.

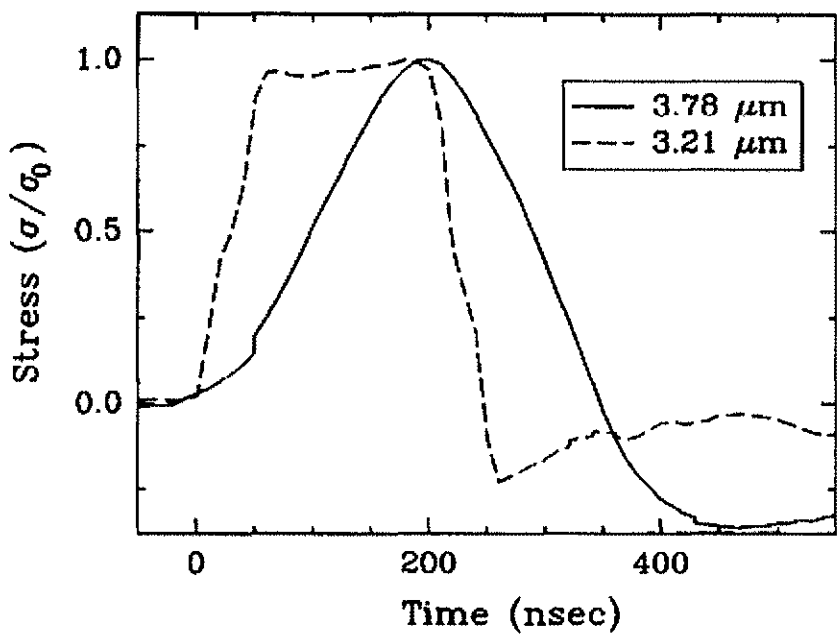

Fig 3.2. Thermoelastically generated stress waves with different rise times [55].

Within the focal volume, the temperature rise occurs during thermalization of the energy carried by the free electrons, i.e., within a few picoseconds to tens of picoseconds. As this time interval is much shorter than the acoustic transit time from the center of the focus to its periphery, there is no possibility for acoustic relaxation during the thermalization time. Hence, the thermoelastic stresses stay confined in the focal volume, leading to a maximum pressure rise. Due to the conservation of momentum, the emitted stress wave must contain both compressive and tensile components such that the integral of the stress over time vanishes. The tensile stress causes the formation of a cavitation

bubble by a relatively small temperature rise in the liquid. The tensile stress wave may induce the fracture of the material for a very small temperature rise. For pulse durations longer than the thermalization time, large amounts of energy are transferred from the free electrons to the heavy particles during the laser pulse, resulting in a temperature of several thousand degrees Kelvin, bubble formation, and a bright plasma luminescence.

A very small bubble formation makes the dissection mechanism compatible with intracellular nanosurgery. Femtosecond pulse lasers produce very small size and short lifetime bubbles, and hence they can be used predominantly than nanosecond pulse lasers. The small bubble size corresponds to a small energy of the expanded bubble. Membrane damage can also be induced by bubble oscillations that occur largely outside the cell, such as in laser optoporation [35].

3.2.4 Stress-Wave Generation in Tissue Targets

Due to ablation or rapid heating, stress waves are generated in tissue. Below the ablation threshold, tissue irradiation (e.g., by a 248 nm KrF laser) produces stress waves by rapid heating. Above the ablation threshold, thermoelastic stress waves are dominated by the stress waves generated by ablation. On the other hand, irradiation of tissue by ArF laser (193 nm) produces stress waves by ablation. Here, because of the low ablation threshold, thermoelastic waves have not been observed [55].

3.3 Biological Effects of Stress Waves

Tissue damage due to stress waves was first noticed by Marshall in 1970 [57] who attributed some of the damage to retinas to stress waves produced during laser irradiation.

He divided the induced tissue damage into two classes, namely, tissue fracture which is caused by: 1) passage of high pressure front; and 2) localized bulk displacement. Many researchers like Dehm et al. [58] investigated cell injuries and attributed the cell killing to mechanical damage caused by stress waves. They also hypothesized that the 248-nm (higher wavelength) irradiation caused substantial cell injury which produced stronger stress waves than the 193-nm (lower wavelength) irradiation. Cells exposed to stress waves sustain structural and functional injuries that increase with the peak stress and the number of pulses applied. Also, it is shown by Doukas et al. (1995) that the degree of cell injury is influenced by the rise time of the stress wave. Furthermore, they showed that the cell injury correlated better with stress rate (stress gradient) than the peak stress [55].

Since the stress waves are capable of killing cells, they are used to treat tumors. The delay of tumor growth has been noticed with laser-induced stress waves. It was also observed that fast growing tumors were more responsive to treatment than slow-growing tumors. Stress waves when used in combination with chemotherapeutic drugs retarded a variety of tumors with varying degrees of success. However, it has been observed that stress waves enhance the cytotoxicity of a number of compounds when present in the extracellular medium during stress wave applications. The stress waves induce a transient increase of the membrane permeability which results in the diffusion of molecules present in the medium (including drugs) into the cells. The synergism of stress waves and drugs is similar to photodynamic therapy where the combination of light and photosensitizers are used for beneficially enhanced outcomes.

3.4 Plasma Formation

In various fields of laser medicine, laser-induced plasma formation has been used for photo-disruption, ablation, or lithotripsy and it has become especially important in intraocular microsurgery.

With nanosecond pulses, where irradiance values are below the optical breakdown threshold, no free electrons are formed because the irradiance is too low to provide seed electrons by means of multiphoton ionization (a mechanism that governs photoionization). In theoretical investigations, the breakdown threshold is defined by the irradiance (or energy) required to produce a certain critical free-electron density at the laser focus. Once the irradiance is high enough to provide a seed electron, the ionization cascade can start and proceeds very rapidly owing to the high irradiance. Within a small fraction of the laser pulse duration, the electron density can shoot up by nine orders of magnitude until its rise is stopped by recombination. The breakdown threshold is extremely sharp – thus either a highly ionized plasma is produced, or no plasma at all [35].

3.4.1 Low-Density Plasmas and their Chemical Effects

In low-density plasmas, the energy density remains below the level required for cavity formation in the medium. Below this optical breakdown threshold, free electrons are produced in a fairly large irradiance range with a deterministic relationship between free-electron density and irradiance. Thus, by varying the irradiance, low-density plasmas can deliberately produce chemical changes, heating, and thermomechanical effects.

Plasma-mediated chemical effects in biological media can be classified into two groups: (i). Changes of the water molecules by which reactive oxygen species (ROS) such as OH* and H_2O_2 are created that affect organic molecules. These species are known to cause cell damage. (ii). Direct changes of the organic molecules in resonant electron–molecule scattering [35]. Capture of electrons into an antibonding molecular orbital causes fragmentation of biomolecules, as shown in figure 3.3.

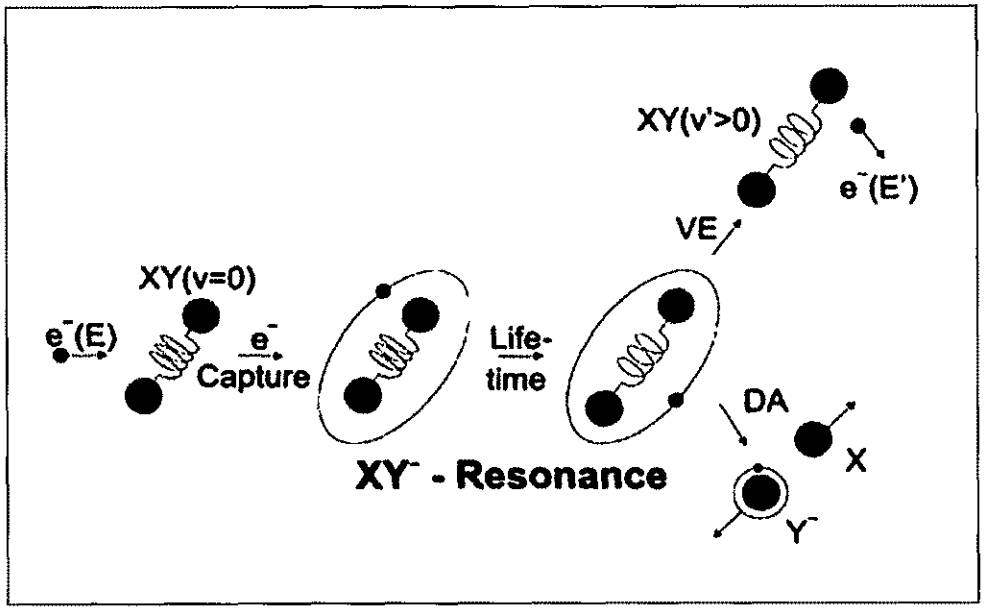

Fig 3.3. Dynamics of vibrational excitation and dissociative electron attachment in resonant electron–molecule scattering [35].

3.4.2 Implications for Laser Effects on Biological Cells and Tissues

Femtosecond laser nanosurgery is done using two techniques: one technique uses long pulse series from femtosecond oscillators with repetition rates of the order of 80MHz, and pulse energies well below the optical breakdown threshold. To achieve the

desired dissection or membrane permeabilization, pulses from 40000 to several million have been applied at one specific location. In the second technique, amplified pulse series at 1-kHz repetition rate with pulse energies slightly above the threshold for transient bubble formation are used. In this technique, the number of pulses is typically varied from about 30 to several hundred [35].

The effects of different low density plasma and the physical breakdown phenomena induced by femtosecond laser pulses based on the above-mentioned two nanosurgery techniques is presented in figure 3.4. An experimental damage, transfection, and dissection thresholds on cells is presented in this figure. The different effects are scaled by the corresponding values of free-electron density and normalized irradiance. The irradiance values are normalized to the optical breakdown threshold I_{th} defined by a critical electron density of $Q_{cr} = 10^{21}$ cm^{-3}.

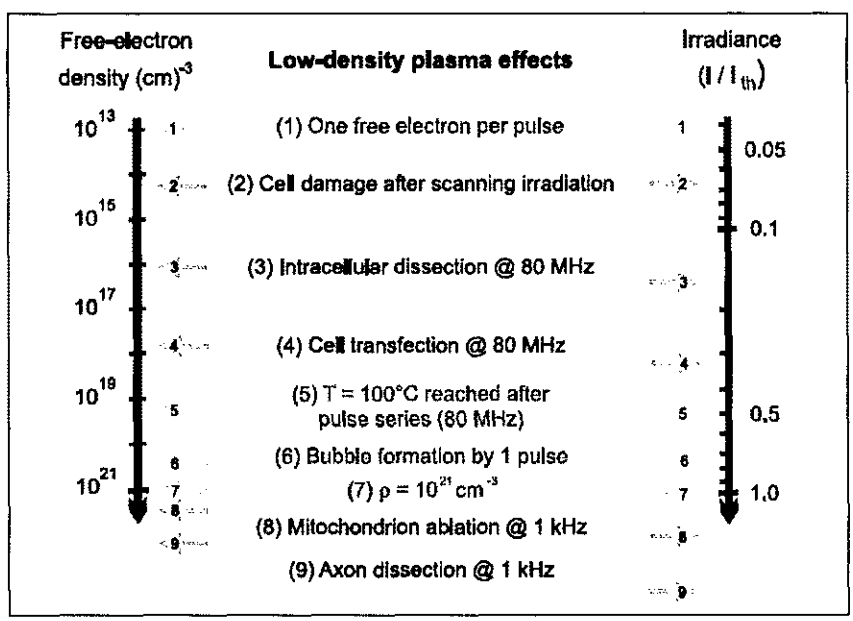

Fig 3.4. Overall view of physical breakdown phenomena induced by femtosecond laser pulses and effects of different low density plasma [35].

In the above figure, chemical cell damage after scanning irradiation (2) of PtK2 cells with 800-nm pulses at 80-MHz repetition rate refers to membrane dysfunction and DNA strand breaks leading to apoptosis like cell death. Chromosome dissection (3) relates to the intranuclear chromosome dissection, and (4) to cell transfection by transient membrane permeabilization, which are performed using 80-MHz pulse trains from a femtosecond oscillator. Mitochondrion ablation (8) refers to the ablation of a single mitochondrion in a living cell using 1-kHz pulse trains, and axon dissection (9) applies to axotomy in live *C. elegans* worms carried out with sequences of pulses emitted at 1-kHz repetition rate from a regenerative amplifier. Points (1), (5), (6) and (7) refer to physical events or threshold criteria [35].

3.5 Summary

The role of mechanical effects such as laser induced waves and cavitation bubble formation in killing cells and their various biological effects have been presented in this chapter. Also, the different ways of stress wave generations including plasma-induced stress-wave generation, ablation induced and thermoelastic generation of stress waves has been briefly discussed. Plasma formation, low density plasmas and their chemical effects, and the implications for laser effects on biological cells and tissues have been covered. These details are meant to provide a more broad background into possible optical effects and mechanisms of lasers on bio-tissues. While some processes can be used for therapeutic purposes, other could be harmful, and so care with laser irradiation needs to be taken.

CHAPTER IV

MODELING OF LIGHT PROPAGATION IN TISSUE

4.1 Introduction

As the absorbed light produces heat, thermal effects of a laser beam incident upon tissues (e.g., the skin, dermis and interior) can be predicted by determining temperature distribution within the skin and interior tissues. A model is required for both light propagation through the tissue and the related energy deposition to estimate the internal temperature distributions. Monte Carlo simulations of photon propagation offer a flexible yet rigorous approach toward photon transport in tissues. In this method, the incident laser beam is represented as a stream of photons, each having a set of initial coordinates, direction and energy weight. This method consists of recording photons histories as they are scattered and absorbed. Thus, in this kinetic, time-dependent approach, the photons are treated as billiard balls that continually undergo free-flight peppered by random scattering events. The scattering events change the direction, momentum and possibly energy, and are associated with interactions between the incoming photons and the host lattice. In cases where the photons lose energy, the scattering process is referred to as "inelastic," while elastic scattering processes merely change momentum but preserve the photon energy. The number of photons required in the simulation depends largely on the precision needed and the spatial or temporal resolution desired [7]. As more of the number of photons is used, then more accurate is the model with lower statistical uncertainties. However, the requisite computation times increase significantly as the number of photons increase. Thus, there is a delicate trade-off between accuracy and computational burden. In this chapter, which contains two parts, the particle-based Monte

Carlo method for modeling light transport in tissues is discussed in part I, while part II discusses the wave nature of light.

Monte Carlo models rely largely on the generation of random numbers which are uniformly distributed over the interval (0, 1). To simulate propagation it is required to generate random numbers repeatedly and randomly-based on a pseudo-random number generator provided by the computer. In this model, a random number can be used to determine the propagation step size, or to determine the deflection angle due to the scattering process, or to choose between a set of competing scattering processes.

Part I – The Traditional Monte Carlo Modeling Scheme

In this part of the chapter, the photon is considered as a neutral particle and its propagation in tissues is discussed.

4.2 Monte Carlo Method

Steps involved in the Monte Carlo method for light propagation in tissue are discussed in detail in the following sections.

4.2.1 Photon Initialization and Initial Conditions

The Monte Carlo simulation begins by launching a photon packet of weight 'w' at a specified angle on a multilayer tissue. For concreteness, only photons having perpendicular incidence are discussed here and are shown in the figures. Also, only three layers are considered in our present simulations, but can be extended to any number of layers. At each step of propagation, some portion of photon energy is absorbed, and this

is mimicked by reducing the weight of the photon packet at every step. For simplicity here, each layer of the tissue has been considered to be parallel to the other layers. It is also assumed to be infinitely wide (i.e., in the transverse directions) on the condition that it is much wider than the spatial extent of the photon distribution along the transverse dimension. Each layer is described by the parameters: layer thickness, refractive index, absorption co-efficient μ_a, the scattering co-efficient μ_s, and the anisotropy factor g, which are initialized and specified as the input. Also, the refractive indices of the ambient medium above the tissue (air) and below the tissue need to be specified.

A Cartesian coordinate system is used to trace the photon movements. The z-axis is taken to be normal to the surface pointing into the tissue and the xy-plane taken to coincide with the tissue surface. A schematic of a multilayered tissue and Cartesian coordinate system is presented in figure 4.1. In this figure, photons are considered to be incident normally onto a parallel surface, and so the initial location of the photon is chosen randomly on the tissue surface as:

$$x = \text{width}(x) * \xi \quad , \tag{4.1a}$$

$$y = \text{width}(y) * \xi \quad , \tag{4.1b}$$

$$\text{and} \qquad z = 0 \quad , \tag{4.1c}$$

where ξ is a random number which lies between (0,1) and the initial direction as (0,0,1).

Since the photon beam is perpendicular to the tissue surface, it has cylindrical symmetry and so a cylindrical coordinate system can be set up simultaneously to score photon absorption as a function of r and z, where r and z are the radial and the z

coordinates of the cylindrical coordinate system, respectively. The origin and the z-axis are the same for both systems.

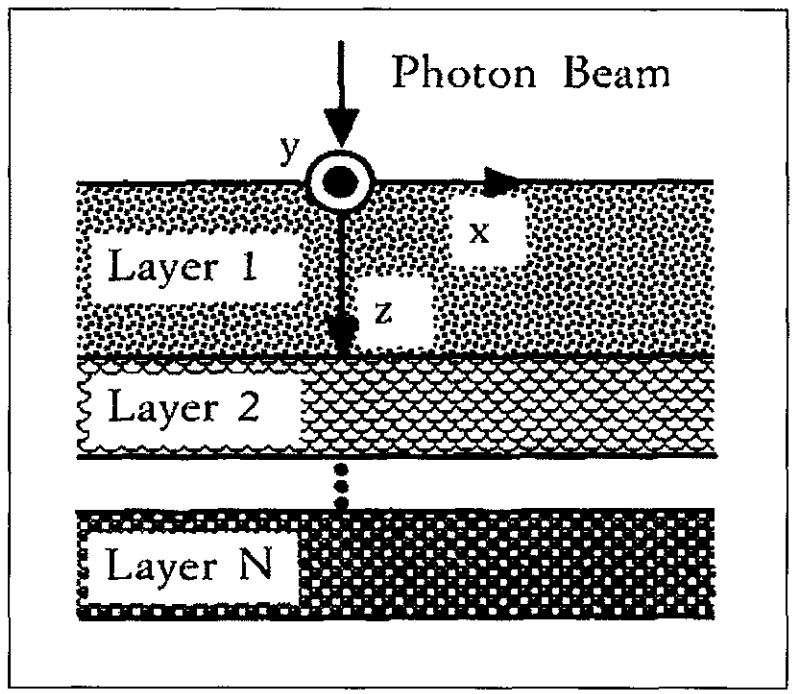

Fig 4.1. A schematic of photon beam incident on a parallel multi-layered tissue and the Cartesian coordinate system [60].

4.2.2 Generating Propagation Distance and Calculating Final Positions

The step size 'Δs' is regarded as the free path of the photon packet movement. Photons are moved through a distance "Δs", and at the end of the each spatial step, absorption and the scattering events are implemented. To be more effective, a variable step size is considered for each photon step. This is more physical and natural, since scattering is a stochastic process, and hence, each the likelihood of each event varies randomly. A uniformly distributed random variable 'ξ' is used to determine this variable step size and its length is given by:

$$\Delta s = \frac{-In\xi}{\mu_t} \quad , \tag{4.2}$$

where $\mu_t = \mu_a + \mu_s$ is the total attenuation co-efficient, and ξ is a random number uniformly distributed in the $0 \leq \xi \leq 1$ range.

Once the step size is calculated, the photon packet is moved through this distance Δs. For a photon located at (x,y,z) travelling with direction cosines (μ_x, μ_y, μ_z), the new coordinates (x',y',z') after the distance Δs are given by:

$$x' = x + \mu_x \Delta s, \tag{4.3a}$$

$$y' = y + \mu_y \Delta s, \tag{4.3b}$$

$$z' = z + \mu_z \Delta s. \tag{4.3c}$$

where (as previously mentioned) μ_x, μ_y and μ_z are the direction cosines corresponding to x, y, and z-axis, respectively. A Cartesian coordinate system showing the direction cosines is presented in figure 4.2. At this instant, one needs to check whether the traversing photon packet might have hit the boundary. This boundary can either be that of the entire simulation region, or simply the termination of a given tissue type. In the event a boundary is reached, the photon packet is checked for possible internal reflection to ascertain its next course of action as discussed in the following section. If the photon packet still remains within the tissue and does not reach any boundary, then the photon is moved through a distance Δs and the new photon positions are updated.

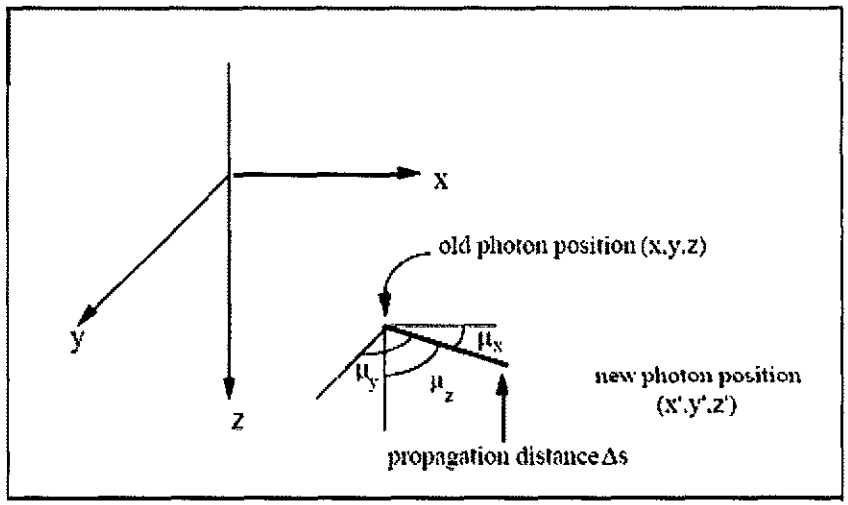

Fig 4.2. A schematic of Cartesian cordinate system showing the direction cosines and the new photon position [61].

4.2.3 Scattering

At the new position, the photon packet undergoes absorption and loses part of its energy. It is then destined to scatter and change its direction. The photon packet's new direction can be completely described by the deflection angle θ ($0 \leq \theta < \pi$) and the azimuthal angle ϕ ($0 \leq \phi < 2\pi$). The azimuthal angle is distributed uniformly over 0 to 2π, whereas the deflection angle is decided by the Henyey-Greenstein phase function. The choice of these two angles is determined based on the generation of two random numbers and the following formulae are applied:

$$\cos\theta = \begin{cases} \dfrac{1}{2g}\left[1+g^2-\left(\dfrac{1-g}{1-g+2g\xi}\right)^2\right], & \text{if} \quad g \neq 0 \\ 2\xi - 1, & \text{if} \quad g = 0 \end{cases}, \tag{4.4}$$

$$\text{and} \qquad \phi = 2\pi\xi\,. \tag{4.5}$$

where ξ is a uniformly distributed random variable and "g" is the anisotropy factor.

Knowing the deflection angle θ and the azimuthal angle ϕ, the new direction cosines (μ_x', μ_y', μ_z') for the subsequent directional movement of the photon packet after the scattering event through the angles (θ, ϕ) in terms of the original cosines (μ_x, μ_y, μ_z) is calculated as:

$$\mu_x' = \frac{\sin\theta}{\sqrt{1-\mu_z^2}}\left(\mu_x\mu_z\cos\phi - \mu_y\sin\phi\right) + \mu_x\cos\theta \tag{4.6a}$$

$$\mu_y' = \frac{\sin\theta}{\sqrt{1-\mu_z^2}}\left(\mu_y\mu_z\cos\phi - \mu_x\sin\phi\right) + \mu_y\cos\theta, \tag{4.6b}$$

$$\mu_z' = -\sin\theta\cos\phi\sqrt{1-\mu_z^2} + \mu_z\cos\theta \tag{4.6c}$$

If $|\mu_z| > 0.99999$ i.e., if the angle of incidence is too close to the normal, then the new direction can be obtained by:

$$\mu_x' = \sin\theta\cos\phi \quad , \tag{4.7a}$$

$$\mu_y' = \sin\theta\sin\phi \ , \tag{4.7b}$$

$$\mu_x' = \frac{\mu_z}{|\mu_z|}\cos\theta \cdot \tag{4.7c}$$

where (μ_x, μ_y, μ_z) are the cosines specifying the direction of the photon before scattering. A Cartesian coordinate system showing the deflection angle (θ) and the azimuthal angle (ϕ) is presented in figure 4.3.

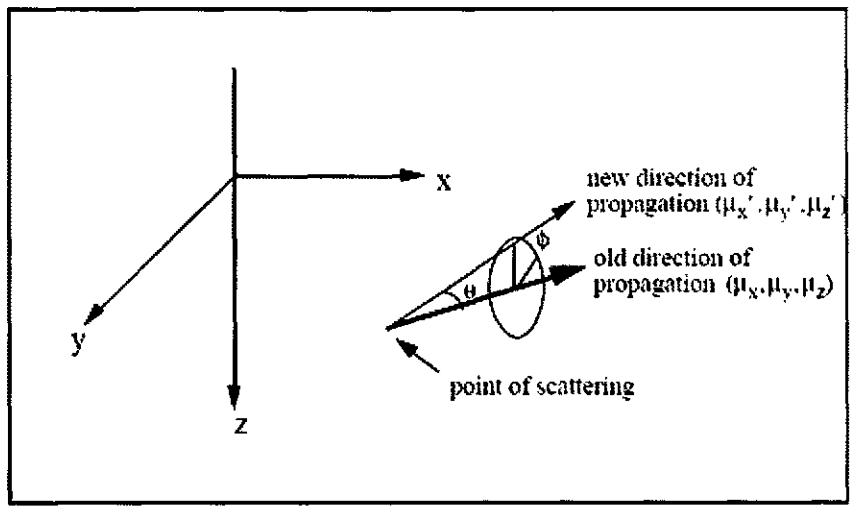

Fig 4.3. A schematic of the Cartesian coordinate system specifying θ and ϕ when a photon is scattered [61].

4.2.4 Internal Reflection

Internal reflection occurs when the photon moves from one medium to another medium having a different refractive index. During this transition, there is a chance of internal reflection when the photon propagates across the boundary of a layer. Fresnel reflection co-efficients $R(\theta_i)$ are used to determine the condition of internal reflection. This co-efficient is given by:

$$R(\theta_i) = \frac{1}{2}\left[\frac{\sin^2(\theta_i-\theta_t)}{\sin^2(\theta_i+\theta_t)} + \frac{\tan^2(\theta_i-\theta_t)}{\tan^2(\theta_i+\theta_t)}\right], \tag{4.8}$$

where θ_i is the angle of incidence at the boundary and θ_t is the transmission angle which is obtained from the Snell's law. These angles are given by:

$$\theta_i = \cos^{-1}(|\mu_z|), \tag{4.9}$$

$$and \quad n_i \sin\theta_i = n_t \sin\theta_t. \tag{4.10}$$

In the above, n_i and n_t are the refractive indices of the incident medium and transmitted medium, respectively. When the angle of incidence is at near-normal incidence to the interface ($\theta_i \approx \theta_t \approx 0$), the reflection co-efficient is given by:

$$R = \left(\frac{n_i - n_t}{n_i + n_t}\right)^2. \tag{4.11}$$

Knowing the reflection coefficient, a uniformly distributed random number '$0 \leq \xi \leq 1$' can be used to determine whether the photon is internally reflected. If '$\xi < R(\theta_i)$', the photon is internally reflected, otherwise the photon exits the layer. If the photon is internally reflected, the new position and the directions of the photon are updated. For a layer whose thickness is T along the z-direction and infinite in x and y directions, the new internally reflected photon position *(x", y", z")* is given by:

$$(x'', y'', z'') = \begin{cases} (x, y, -z) & if\ z < 0, \\ (x, y, 2T - z) & if\ z > T. \end{cases} \tag{4.12}$$

and the new photon direction (μ_x', μ_y', μ_z') is:

$$(\mu_x', \mu_y', \mu_z') = (\mu_x, \mu_y, -\mu_z). \tag{4.13}$$

Thus, the new direction (and hence, the velocity) is a mirror image about the reflecting plane. As the free path Δs is generated randomly, there is a chance of photon crossing the boundary and entering into another layer. This condition needs to be checked in the simulations. If this occurs, the photon is moved back to the boundary and once again checked for internal reflection. Depending on the outcome for possible internal reflection, the photon is either assigned a new, reflecting direction at the boundary, or continued with its original direction of traversal.

4.2.5 Photon Absorption

For each propagation step Δs, part of the photon packet energy is absorbed (viewed as an absorption event in Monte Carl parlance) and the rest is scattered within the packet. The fraction of the packet that is absorbed (FA) is:

$$\text{FA} = \text{fractionabsorbed} = \frac{\mu_a}{\mu_a + \mu_s}, \tag{4.14}$$

$$= 1 - \frac{\mu_s}{\mu_a + \mu_s}, \tag{4.15}$$

$$= 1 - a \tag{4.16}$$

where 'a' is the single particle albedo and the new photon weight w' after the absorption event is therefore:

$$w' = aw \tag{4.17}$$

At each step, the absorbed energy weight is scored into an array (say A), and hence the energy deposited due to the light propagation at each location is tracked. At this point, the new photon weight is compared with the minimum photon weight. If the photon weight falls below the minimum weight, then the photon packet is terminated, otherwise it is scattered with its new weight w'. The minimum weight is chosen in such a way that the discarded photon packet below leads to very little information loss. If the photon exits the side boundary then the photon is tracked to the boundary and the energy deposition is calculated up until the boundary, and then the photon packet is terminated.

A schematic of Monte-Carlo simulation steps of laser beam propagation in a three-layered tissue is presented in figure 4.4.

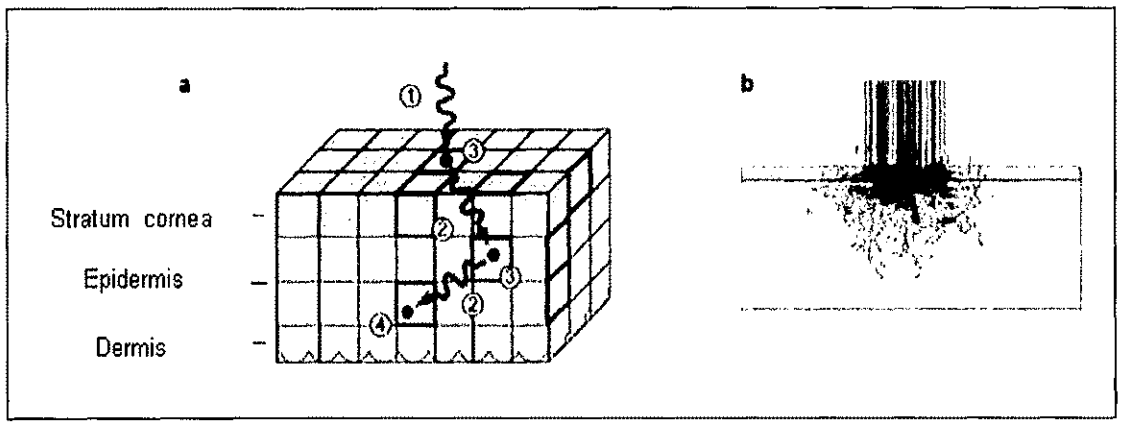

Fig 4.4. (a) A schematic representation of Monte-Carlo simulation steps of laser beam propagation in skin (1), photon generation (2), pathway generation (3), and absorption (4), termination and detector count. Black dots represent scattering events and blue squares detector cell counts. (b) Side view of actual calculation [62].

4.3 Internal Energy Distribution in Skin (Tissue)

A tissue with a uniform temperature distribution (say, 310° K) is considered initially prior to any laser beam incidence on this tissue. Upon laser irradiation, the bio-tissue is expected to undergo temperature variations. A cylindrical system is considered to score the energy deposition due to the incident laser beam. A two-dimensional, homogeneous grid system is set up in the r and z directions for scoring photon energy absorptions. Each grid is separated from the other by Δr and Δz in the r and z directions, respectively. The total number of grid elements in the r and z directions are thus N_r and N_z. The absorbed energy is scored into an array of $A_{rz}[i_r,i_z]$. Here i_r and i_z are the indices for the grid elements in the r and z directions and $1 \leq i_r \leq N_r$ and $1 \leq i_z \leq N_z$.

The above Monte Carlo procedure of tracking the movement of incident photon packets through the bio-tissue, along with the multiple scattering events, allows for the calculations and assessment of energy deposition. This energy absorption data can then be used to evaluate the temperature changes and time-dependent fluctuations due to

photon pulses or continuous laser excitation. The temperature changes within the bio-tissue due to the absorbed energy can be obtained from the Pennes bioheat transfer equation. This is given as:

$$\nabla.[K\nabla T(r,t)]+W_bC_b(T_b-T)+Q_m+Q_r=\rho C\frac{\partial T(r,t)}{\partial t}\quad , \tag{4.18}$$

where K [W/(m.K)] is the thermal conductivity, W_b [kg/(m^3.s)] is the blood perfusion rate, C_b and C [J/(kg.K)] are the specific heats of blood and tissue, T_b and T (^oK) are temperatures of blood and tissue, respectively; Q_m (W/m^3) is the metabolic rate of tissue, Q_r (W/m^3) is the volumetric heating rate, and ρ (kg/m^3) is the tissue density.

Consider the first term: $\nabla.[K\nabla T(r,t)]$. Here K is taken to be a constant, and the temperature gradient along the r and z directions needs to be calculated. In the z direction it is evaluated implicitly at the i^{th} location as:

$$\mathrm{K}\frac{d}{dz}\left(\frac{dT}{dz}\right)=\mathrm{K}\left[\frac{\left(\frac{T_{i+1}-T_i}{\Delta z}\right)-\left(\frac{T_i-T_{i-1}}{\Delta z}\right)}{\Delta z}\right]\quad , \tag{4.19}$$

whereas in the r direction and at the j^{th} location, it is evaluated as:

$$\mathrm{K}\frac{1}{r}\frac{d}{dr}\left(r\frac{dT}{dr}\right)=\mathrm{K}\frac{1}{r_j}\left[\frac{r_{j+\frac{1}{2}}\left(\frac{T_{j+1}-T_j}{\Delta r}\right)-r_{j-\frac{1}{2}}\left(\frac{T_j-T_{j-1}}{\Delta r}\right)}{\Delta r}\right]\quad , \tag{4.20}$$

where T_j , T_{j+1}, T_{j-1} are the temperatures at j^{th}, $(j+1)^{th}$ and $(j-1)^{th}$ locations, respectively.

In the second term: $W_b\, C_b(T_b - T)$, *the* W_b, C_b and T_b are assumed to be constants and are initialized, while T is the local tissue temperature at the $(i,j)^{th}$ location along (r,z).

The metabolic rate of the tissue 'Q_m' is assumed to be a constant, and Q_r is set to 0 as the heat is considered to be incident only on the skin surface. Thus, Pennes bioheat equation can be used to determine the temperature distribution inside the skin as a function of time and spatial co-ordinates. But due to the diffusion process, the resulting temperature is taken to be the average of the temperature at that location and its surrounding four locations. This "nearest-neighbor" averaging yields a more stable and accurate representation of the temperature. Therefore the new temperature at a location (i,j) is:

$$T_{new}(i,j) = \frac{T(i,j) + \frac{T(i+1,j)+T(i-1,j)+T(i,j+1)+T(i,j-1)}{4}}{2} \tag{4.21}$$

The above process of calculating the temperature at various spatial points within the discretized simulation region is carried out for a chosen simulation duration of interest. Typically, since the heat diffusion is a slow process (taking up to milliseconds for thermalization), while the optical energy transfers from the laser are typically very fast (on the order of sub-nanosecond), the photon energy deposition and the heat diffusion processes can typically be de-coupled. For example, the Monte Carlo (MC) simulation can be carried out initially for a certain duration to obtain the energy absorption and heat input rate. The MC calculations can then be stopped, while the energy deposition rates can be used to update and dynamically compute the internal temperature changes and heat flow. The MC results can easily be "frozen" up to the millisecond range, since

temperature changes do not occur prior to this characteristically typical timescale. Beyond this temporal range, the MC calculations would need to be performed again with appropriate changes in the temperature-dependent parameters to obtain the heat absorption rates corresponding to the new internal temperatures. Thus, in short, the heat flow and temperature changes at each location within the tissue due to laser irradiation (whether pulsed or continuous) can be determined via the coupled MC-Pennes heat procedure. The procedure is realistic in that it embeds photon scattering, multi-tissue variability, intricate geometries (though only the simple Cartesian geometry has been discussed here), allows for variability in the photon wavelength, spatial profile (though in this thesis only the uniform and Gaussian profiles have been considered), flux and incidence angles, and temporal characteristics. Similarly, user-specified changes in bio-tissue characteristics (e.g., the thermal conductivities, perfusion rates, specific heats etc.) can be easily accommodated.

Part II – Inclusion of Phase in Photon Simulations

4.4 Introduction to Phase Behavior in Optics

The phase of each light ray changes as it propagates. When a ray reaches the detector (observation plane), it contributes to the total energy and signal intensity. However, this total strength is the coherent addition of all other rays that have reached the same location [63, 64]. In Electrical Engineering parlance, this coherent addition amounts to a "phasor sum" of the individual rays. This implies that both the magnitude and phase-angle of each individual ray needs to be taken into account. Thus, changes in phase angles of the rays during their propagation affect the resultant intensity at any location. The Monte Carlo

model can be used to model phase changes and to find the resultant intensity of the rays at any location. This could be based on the Huygens – Fresnel principle which states that: every point of a wave front may be considered to be the source of secondary wavelets (Huygens wavelet) that spread out in all directions with a speed equal to the speed of propagation of the waves. Monte Carlo sampling of the Huygens wavelets involves launching multiple rays from the center of each wavelet and tracking the change in phase of each ray before it reaches the observation plane [64]. The phase of each ray can be found by keeping track of the distance traveled by a light pulse as it propagates in the tissue. A ray that has travelled a distance "d" will have 'kd' added to its phase where k is its wave-number given as: $k = 2\pi/\lambda$ with λ being the wavelength [63].

4.5 Model to Calculate Phase Changes

Consider a source "S" launching rays uniformly over a semicircle with this source element at the center as sketched in figure 4.5. Each ray is launched with an initial amplitude and phase specified by the field at that source element. Here, for simplicity, the initial amplitude of all the rays is considered to be unity and to have zero initial phase (reference phase value). Suppose a physical structure (aperture) with two small openings is interposed between the source and the detector. In this situation, the rays that reach the slits act as the sources (S_1 and S_2) and propagate further. This is depicted schematically in figure 4.5. This is equivalent to sampling the Huygens wavelets originating from each source. The rays that propagate from the sources reach the detector and the rays that reach the same location on the detector are added coherently.

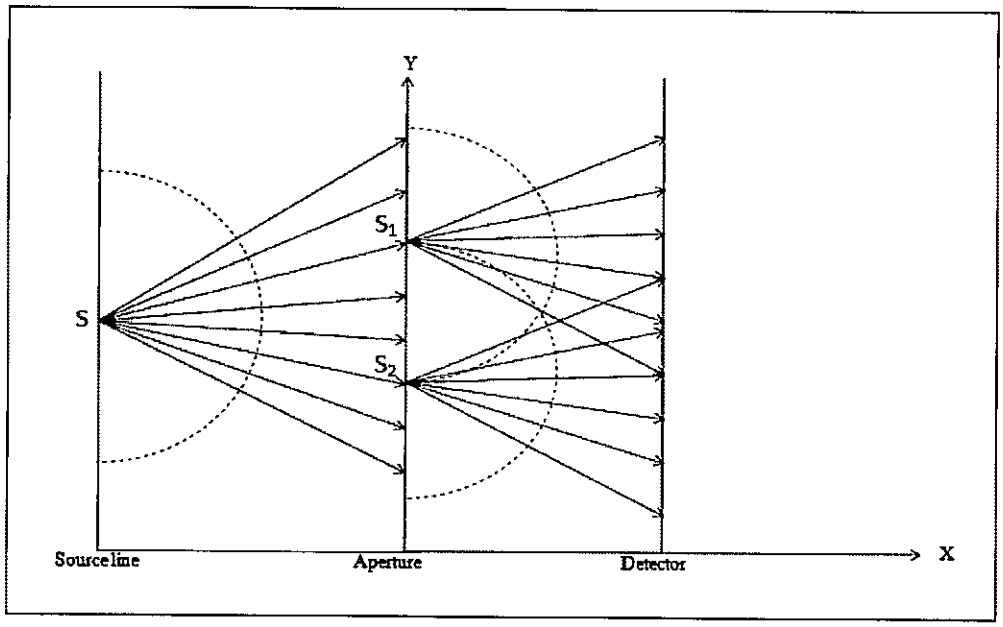

Fig 4.5. Rays used to approximate a Huygens wavelet.

Suppose the light rays whose wavelength is 'λ', originating from the different sources, travel distances (path lengths) of L_1, L_2, L_3, L_4, etc.. and reach the same point on the detector. Then if the absolute value of the differences in lengths is equal to an integer multiple of λ, then they are said to be in phase and constructive interference occurs. Otherwise if the absolute difference between the paths is some integer number of wavelengths plus half a wavelength, then they are said to be out of phase and destructive interference occurs. Thus, mathematically, if:

$$| L_1 - L_2 - L_3 - L_4 - ..... | = m\lambda \qquad \text{(Constructive Interference)} \qquad (4.22)$$

$$| L_1 - L_2 - L_3 - L_4 - ..... | = (m+\tfrac{1}{2})\lambda \qquad \text{(Destructive Interference)} \qquad (4.23)$$

where 'm' is an integer.

The final phase of each ray that has travelled a distance L is:

$$\phi = (\frac{2\pi}{\lambda})\, L \tag{4.24}$$

Suppose rays with initial intensities I_1, I_2, I_3,... and zero initial phases travel distances L_1, L_2, L_3,... and reach a location on the detector with final phases ϕ_1, ϕ_2, ϕ_3 ... respectively, then the resultant intensity I at that location due to all these rays is

$$I = I_1 e^{-i\phi_1} + I_2 e^{-i\phi_2} + I_3 e^{-i\phi_3} + ... \tag{4.25}$$

and its magnitude is:

$$|I| = \sqrt{(I_1\cos(\phi_1) + I_2\cos(\phi_2) + I_3\cos(\phi_3) + ...)^2 + (I_1\sin(\phi_1) + I_2\sin(\phi_2) + I_3\sin(\phi_3) + ...)^2} \tag{4.26}$$

where ϕ_1, ϕ_2, ϕ_3,... can be obtained from L_1, L_2, L_3,...as:

$$\phi_1 = (\frac{2\pi}{\lambda})L_1,\ \phi_2 = (\frac{2\pi}{\lambda})L_2,\ \phi_3 = (\frac{2\pi}{\lambda})L_3 \text{ and so on.}$$

If the initial intensities of all the rays are equal, i.e., if $I_1 = I_2 = I_3 = ... = I_0$ (say), then the resultant intensity is:

$$|I| = I_0 * \sqrt{(\cos(\phi_1) + \cos(\phi_2) + \cos(\phi_3) + ...)^2 + (\sin(\phi_1) + \sin(\phi_2) + \sin(\phi_3) + ...)^2} \tag{4.27}$$

4.6 Monte Carlo Simulations

In this thesis work, the Monte Carlo technique has been used to model phase changes of a moving ray with inclusion of the various scattering events. A two-dimensional (2D) model has been developed to demonstrate the influence of phase angles on the final intensity for simplicity. The primary aim is to demonstrate the inclusion of photon phase in Monte Carlo calculations. Hence, a 2D approach, rather than a full three-dimensional treatment, is attempted for purposes of demonstration. Once implemented, this could easily be expanded to a full 3D model in the future. The steps involved in this model development are discussed in detail in the following sections.

4.6.1 Initial Conditions

The method has been implemented on a specific structure for concreteness and simplicity. A physical structure (aperture) of length 1000λ with two slits separated by a distance 60λ is taken. These two slits act as the two secondary-light sources that launch rays uniformly over a semicircle with the two sources at the center. A detector of length 1000λ is assumed and taken to be at a distance of 10000λ from the physical structure. The rays (photons) emitted from the light sources are tracked at the detector and the resulting intensities calculated.

Initial amplitudes of the intensities of all the rays are all taken to be unity with a zero initial phase (reference phase value). The two sources are assumed to be located at $(0, 30\lambda)$ and $(0,-30\lambda)$, with the detector parallel to the y-axis. As the rays are uniformly distributed over the entire semicircle, the initial direction of each ray varies and depends on the initial angle "θ" between a ray and the normal to the aperture. Hence, in the

present geometry, this angle θ varies from $-\pi/2$ to $\pi/2$. Initial direction cosines are given by:

$$\mu_x = \cos(\theta), \tag{4.28a}$$

$$\text{and,} \quad \mu_y = \sin(\theta). \tag{4.28b}$$

The initial distance (path length) travelled by the photon is taken as zero i.e., L = 0.

4.6.2 Moving the Photons

Rays (photons) originating from the two sources are moved through a free mean path 'Δs' and are then scattered. Scattering events occur every time the photons travel a free mean path distance. The free mean path is calculated using the formula:

$$\Delta s = \frac{-In\xi}{\mu_t}, \tag{4.29}$$

where $\mu_t = \mu_a + \mu_s$ is the total attenuation co-efficient which is the sum of absorption co-efficient and the scattering co-efficient. In equation (4.29), ξ denotes a random number that lying between (0, 1).

Each time the photon travels free mean path the total distance travelled by the photon is updated as:

$$L = L + \Delta s \tag{4.30}$$

4.6.3 Updating Photon Positions

The positions of the photon are updated after travelling a free mean path. The new photon position (x',y') which is travelling along the direction (μ_x, μ_y) is given by:

$$x' = x + \mu_x \Delta s, \tag{4.31a}$$

$$\text{and,} \quad y' = y + \mu_y \Delta s. \tag{4.31b}$$

During the simulation, if a photon moves past the detector, then it is moved back on to the detector location and its new position coordinates are calculated as:

$$x_f = 10000\lambda, \tag{4.32a}$$

$$\text{and,} \quad y_f = y + (x_f - x)\frac{(y'-y)}{(x'-x)} \tag{4.32b}$$

Hence, the new free path Δs is:

$$\Delta s = \sqrt{(y_f - y)^2 + (x_f - x)^2} \tag{4.33}$$

This new free path Δs is used to update the total distance travelled by the photon "L." It is also the basis for updating the phase of the photon, since the differential phase change $\Delta\varphi$ is then given through: $\Delta\varphi = (2\pi/\lambda)\,\Delta s$.

4.6.4 Scattering

After travelling free mean path each time, the photon scatters and changes its direction. The deflection angle "θ" describes the photon new direction and it depends on the value of anisotropy factor 'g'. It can be calculated from Henyey-Greenstein phase function [7] as:

$$\cos\theta = \begin{cases} \frac{1}{2g}\left[1+g^2-\left(\frac{1-g}{1-g+2g\xi}\right)^2\right], & if \quad g \neq 0 \\ 2\xi - 1, & if \quad g = 0 \end{cases} , \tag{4.34}$$

where ξ is a uniformly distributed random variable and θ varies from 0 to 180 degrees.

As it is a 2D case, the photon can be deflected either upwards (positive θ) or downwards (negative θ). To decide its deflection, a random number is generated and it is compared with a value 0.5 (the average of random numbers). If 'ξ' > 0.5, θ is taken to be positive otherwise it is taken as negative i.e., $\theta = -\theta$.

Knowing the deflection angle θ, the scattered photon direction cosines (μ_x', μ_y') which was travelling in the direction (μ_x, μ_y) can be calculated using:

$$\mu_x' = \mu_x \cos\theta - \mu_y \sin\theta , \tag{4.35a}$$

$$\text{and,} \quad \mu_y' = \mu_x \sin\theta + \mu_y \cos\theta \tag{4.35b}$$

4.6.5 Energy Loss

Photons lose their energy as they propagate in an absorbing medium. At every propagation step of the MC process, a part of the photon energy is reduced. The amount of energy lost depends on the absorption and scattering co-efficients that characterize the medium. This fraction (FL) is given by:

$$\text{Fractionlost} = FL = \frac{\mu_a}{\mu_a + \mu_s} . \tag{4.36}$$

At this instant the photon travels with new energy "E" which is given by:

$$E = E_{old} - \left(\frac{\mu_a}{\mu_a + \mu_s} \right) E_{old} \quad . \tag{4.37}$$

At each propagation step this energy is updated.

4.6.6 Calculation of Intensity

After undergoing scattering events and energy losses, the photon finally reaches the detector at some location. The total distance 'L' travelled by the photon is calculated and hence the final phase of that photon (ray) can be obtained by using the formula of equation (4.24). When multiple rays reach the same location, the resultant intensity at that point is due to the additive contributions from all the rays and can be obtained by using the equation (4.26).

The above process will work well in theory. However, from a practical standpoint, as the distance between the initial source and the detector is increased, the number of photon propagation steps and the scattering events increases. The main reason for this difficulty is that one needs to take into account a large number of photons in order to achieve reasonable accuracy. Since phase changes occur on the order of a wavelength, the number of photon rays needed to yield an accurate solution scales as: L/λ, with L being the source-detector separation. With the wavelengths typically in the sub-micrometer range, distances above a few microns can entail large computational burdens. This makes the Monte Carlo technique difficult and cumbersome to implement for phase-calculations. Instead, under such conditions, a Transfer Matrix (TM) approach could be

utilized to reduce the computational time. This aspect is discussed in detail in the following section.

4.7 Transfer Matrix Approach

Transfer matrix approach is used to minimize the Monte Carlo runs for photons, include phase information, to achieve much better statistics, reduce computational time and avoid having to deal with a large number of "secondary photon entities." This amounts, in a sense, to computing the Green's function for the photon propagation problem.

Consider a volume segment of width "R" as shown in Fig. 4-6. Photons of energy E_1, E_2, ... E_N are incident from the left and pass through the volume segment shown.

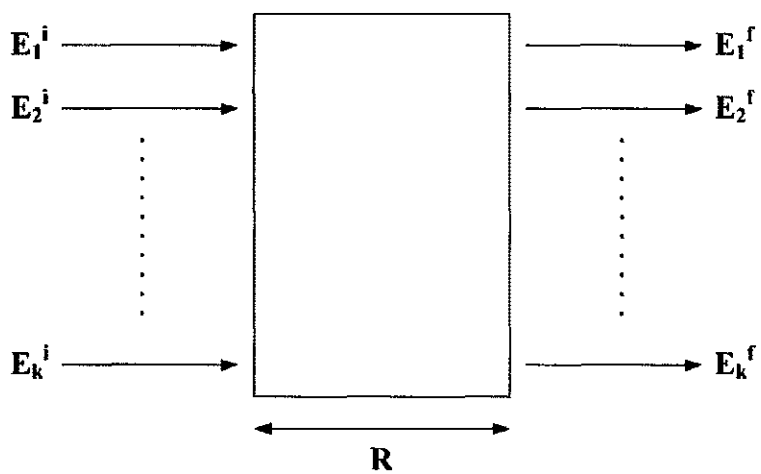

Fig 4.6. Incident and final energies in the Transfer Matrix approach.

Starting with a single input energy photon and using the usual (Jacques-type) Monte Carlo approach, energy of the outgoing photon and its phase can be obtained. This

automatically takes scattering into account. For good statistics, a large number of photons (say M) are to be launched and the energies and phase angles of all M entities that exit the differential segment of width "R" are recorded. Though a Monte Carlo scheme is to be applied, the spatial segment "R" which needs to be considered can be relatively small. In fact, only a segment as short as a mean-free path need be used. This will adequately ensure the occurrence of at least a scattering event during the traversal through the distance "R."

4.7.1 Energy Calculation

Using the transfer matrix concept the connection between the incident and outgoing photon numbers at the different energies can be expressed as: $[N_f] = [T]\,[N_i]$. In expanded form:

$$\begin{bmatrix} N(E_1^f) \\ N(E_2^f) \\ N(E_3^f) \\ .. \\ .. \\ N(E_K^f) \end{bmatrix} = \begin{bmatrix} T_{11}\,T_{12}\,T_{13}\,T_{14} \ldots\ldots T_{1K} \\ T_{11}\,T_{22}\,T_{23}\,T_{24} \ldots\ldots T_{2K} \\ T_{31}\,T_{32}\,T_{33}\,T_{34} \ldots\ldots T_{3K} \\ .. \\ .. \\ T_{K1}\,T_{K2}\,T_{K3}\,T_{K4} \ldots\ldots T_{KK} \end{bmatrix} \begin{bmatrix} N(E_1^i) \\ N(E_2^i) \\ N(E_3^i) \\ .. \\ .. \\ N(E_K^i) \end{bmatrix}$$

Here $N(E_j^{f,i})$ denotes the number of final/incident photons with energy E_j. For numerical computations, the energies (above) have been broken down into K bins. Since the MC uses "M" photon entities: $\sum_{j=1}^{K} N(E_j^i) = \sum_{j=1}^{K} N(E_j^f) = M$.

Starting with a monochromatic source of M incident photons (of say, energy E_1^i), one has $N(E_1^i) = M$, and the values of $N(E_j^f)$ can be obtained from the MC. As a result, the

values of T_{11} (=$N(E_1^f)/M$), T_{21} ,T_{31} , .. T_{K1} can all be obtained. Similarly, by launching monochromatic photons of energy E_2^i and recording the output photon numbers at the various energies, the matrix elements T_{12}, T_{22}, T_{32},... T_{K2} can be calculated. Thus, in short, all the elements of the matrix [T] can be found systematically.

4.7.2 Phase Angle Calculations

The phase angles for the exiting photons can be computed in a similar manner from the Jacques-type Monte-Carlo calculations. This involves starting from a population of monochromatic incident photons of energy E_1^i and keeping track of the total distance travelled by each photon, with scattering included.

Using the transfer matrix concept, the connection between the incident and outgoing photon numbers at the different phase angles can be expressed as: $[N_\theta^f] = [T^\theta]\ [N_\theta^i]$. In expanded form:

$$\begin{bmatrix} N(\theta_1^f) \\ N(\theta_2^f) \\ N(\theta_3^f) \\ .. \\ .. \\ N(\theta_K^f) \end{bmatrix} = \begin{bmatrix} T_{11}^\theta\ T_{12}^\theta\ T_{13}^\theta\ T_{14}^\theta \ldots\ldots T_{1K}^\theta \\ T_{21}^\theta\ T_{22}^\theta\ T_{23}^\theta\ T_{24}^\theta \ldots\ldots T_{2K}^\theta \\ T_{31}^\theta\ T_{32}^\theta\ T_{33}^\theta\ T_{34}^\theta \ldots\ldots T_{3K}^\theta \\ .. \\ .. \\ T_{K1}^\theta\ T_{K2}^\theta\ T_{K3}^\theta\ T_{K4}^\theta \ldots\ldots T_{KK}^\theta \end{bmatrix} \begin{bmatrix} N(E_1^i) \\ N(E_2^i) \\ N(E_3^i) \\ .. \\ .. \\ N(E_K^i) \end{bmatrix}$$

Here θ_j^f denotes the j^{th} discretized phase angle after the photons exit the segment "R." For numerical computations, the phase angles would be broken down into bins, with θ_j^f ranging from [0, 2π]. As before: $\Sigma\ N(\theta^f) = M$. The initial phase angle for all M incident photons is zero, though different energies are to be used. Again, the entire matrix $[T^\theta]$ can

be obtained by carrying out the MC simulations starting with different mono-energetic bunches of incident photons.

The above was discussed in the context of a small rectangular region of width "R." However, for a more realistic analysis, one needs to include (at the very least) a 2D geometry, and the various angular scattering (e.g., as given by the Henyey-Greenstein anisotropic description). This can easily be implemented by considering a quadrant of a circle (e.g., the 1st quadrant as shown in figure 4.7 below) of radius "R." The schematic shows photons incident from the origin. The outgoing photons emerge from the various angular sectors at angles α_j (with $0 < \alpha_j < \pi/2$).

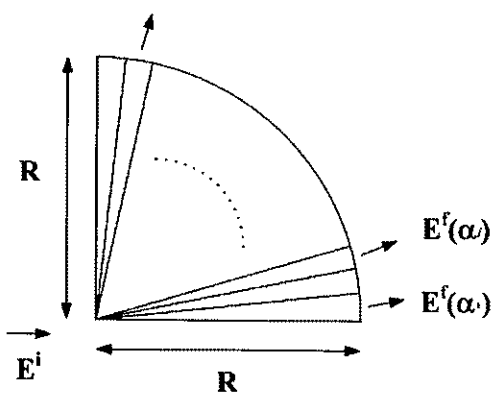

Fig 4.7. Monoenergetic photons incident from the origin. Outgoing populations along various angular segments follow Monte Carlo paths.

The energy population matrix: [Nf] = [T][Ni], remains the same, except that one would now get a sequence of such matrices for each of the different sectors α_j. Similarly, for the phase angles, the relation $[N_\theta^f] = [T^\theta]\,[N_\theta^i]$ would hold, but such matrices would need to be determined for each angular sector α_j.

In a practical implementation, the distance "R" needs to be chosen such that it does not involve an inordinate number of MC scattering events, and yet includes sufficient

scattering information. One possible selection is to keep $R \sim (2\text{-}5)/\mu_t$, where μ_t is the total maximum scattering inverse lengths. In this scheme, the Green's function $G(E_k^f, \alpha_f | E_l^i, \alpha_i)$ corresponds to the matrix element T_{kl}^{θ} connecting the incident energy E_l with the final energy E_k for the α^f angular sector starting with incoming photons that have an angle α^i. The function can $G(E_k^f, \theta^f, \alpha^f | E_l^i , \theta^f , \alpha^i)$ similarly be constructed.

4.8 Summary

Monte Carlo model for light propagation in tissues and the steps involved in the model has been discussed in detail as part I of this chapter. It has been shown that the amount of energy absorbed within the tissue as the photon propagates can be calculated. From this, the heat generated due to the absorbed energy and internal heat distribution could be evaluated as has been discussed. In this model photons are treated as neutral particles and no phase information is taken into account. But since photons exhibit a wave-particle duality, the phase information of the propagating photon also needs to be included. This aspect is discussed in part II of this chapter. Monte Carlo model based on the Huygens-Fresnel principle to include phase changes of moving photons is developed and presented for the simple 2D case. Later, towards the end of this chapter, a more efficient "Transfer Matrix approach" has been described to reduce the computational burden of a full MC. Such a TM implementation would be useful for large geometries. It is shown that this method could be used to include phase information and achieve good accuracy.

CHAPTER V

SIMULATION RESULTS AND DISCUSSION

5.1 Introduction

The simulations that have been conducted as part of this thesis and their subsequent analyses with appropriate discussions are presented in this chapter. Simulations involving the Monte Carlo model of light propagation in bio-tissues were carried out in FORTRAN; whereas, simulations to include phase angles into the model and to analyze its effects on the light intensities were done using the MATLAB® tool. Output results for both models were plotted using MATLAB due to its powerful, built-in, graphical tools. Results from the Monte Carlo model developed for light propagation in tissue and their analyses are presented in section 5.2. This includes energy absorption in different tissue layers as a function of depth. In a sense, these results provide a crude and qualitative validation of the model implementation, since energy absorption is known to follow the Beer-Lambert characteristic. In section 5.3, the energy absorbed by the tissue as predicted by the Monte Carlo simulations, is then taken as the input and used to estimate temperature distributions within the bio-tissue. In other words, predictions of internal tissue heating are performed and reported due to the incident laser stimulation. The Monte Carlo results of the energy deposition are used as the basis for heating. Next, sections 5.4 and 5.5 are devoted to the model that includes and quantitatively treats phase changes as the light rays propagate. The results are given and appropriately analyzed. In these sections, results from both a deterministic simulation of ray propagation with phase changes, as well as stochastic treatments based on the Monte Carlo technique, are presented. A comparison between the two sets of results is made with relevant

discussions. The Monte Carlo implementation can be more general in terms of allowing for random scattering of photons, and this is brought out.

5.2 Simulation Model for Light Propagation in Tissue

A three layered tissue geometry as shown in figure 5.1 was considered for the Monte Carlo simulation of light propagation in bio-tissue. Three layers for the skin (top Stratum cornea, middle Epidermis, and lower Dermis) were chosen as the bio-tissue sample for purposes of simulation. These three layers differ from each other in thickness, absorption co-efficients, scattering co-efficients, and refractive indices. It is assumed that air with refractive index n=1 is present above the topmost (Stratum cornea) layer. Also, below the lower layer dermis, an adjoining tissue with refractive index 1.44 is taken to be present. A laser beam of wavelength λ = 585 nm and energy 20 kJ per unit area (i.e., E_{total} = 20 kJ/m^2) was considered for the simulations. The laser beam was represented as a packet of N = 20,000 photons, and the photons were incidentally normally on the top layer one at a time. The lateral distribution was taken to be a Gaussian with standard deviation σ = 2.25 mm. The widths of the tissue along the x and y direction were taken as 2*σ (= widthx) and 2*σ (= widthy) respectively. Along the z direction, the total thickness was the summation of all the three layers. The model is depicted schematically in figure 5.1 below.

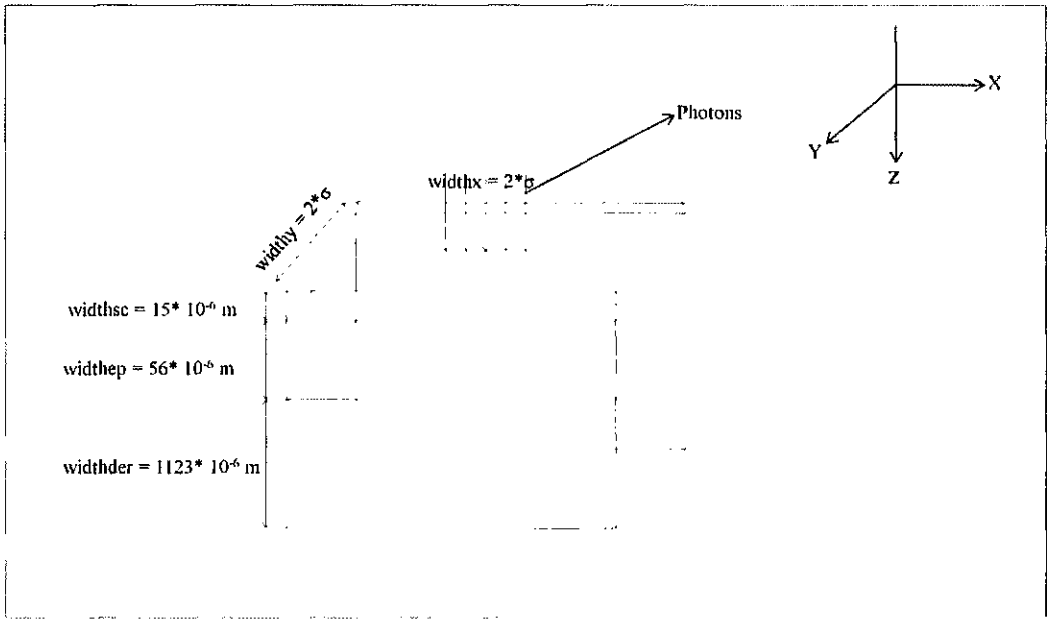

Fig 5.1. A schematic representation of Monte Carlo model.

The angle at which the photons deflects after each propagation step is a function of anisotropy factor 'g' and is generated using a random number. The range of the deflection angle depends on the value of g. Larger the g value, the more is the scattering in the forward direction. The significance of the g value on the deflection angle can be understood from the figures 5.2 to 5.5. Figures 5.2, 5.3, 5.4 and 5.5 are the histograms of the deflection angle for g = 1, g = 0.9, g = 0.79 and for g = 0.5, respectively. For g =1, the deflection angle is zero and so there is no change in the photon propagation direction (no deflection). Thus, all photons would move forward at this g=1 setting. It can be observed that as the value of g decreases from maximum value of 1 towards 0, the range of values that the deflection angle can take, increases.

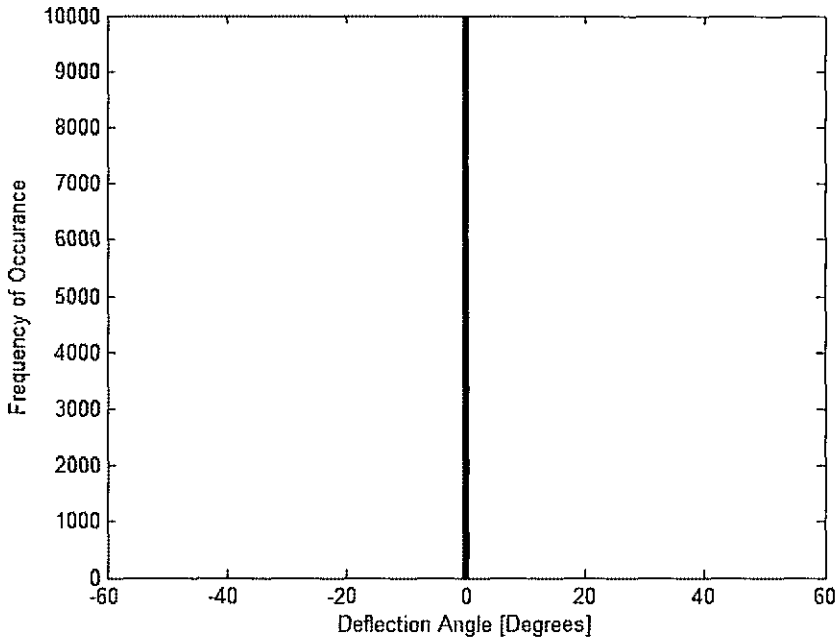

Fig 5.2. Histogram of the deflection angle for the anisotropy factor g = 1.

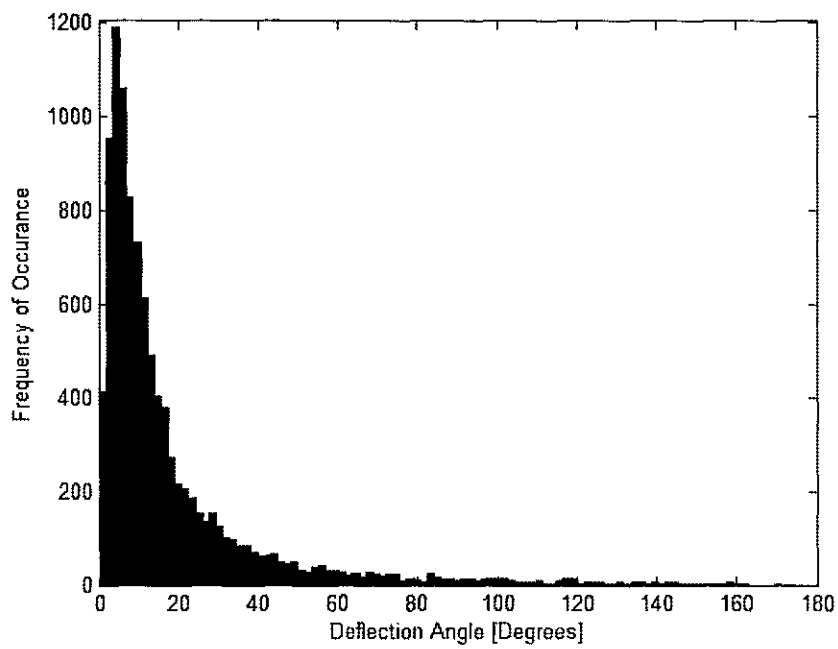

Fig 5.3. Histogram of the deflection angle for the anisotropy factor g = 0.9.

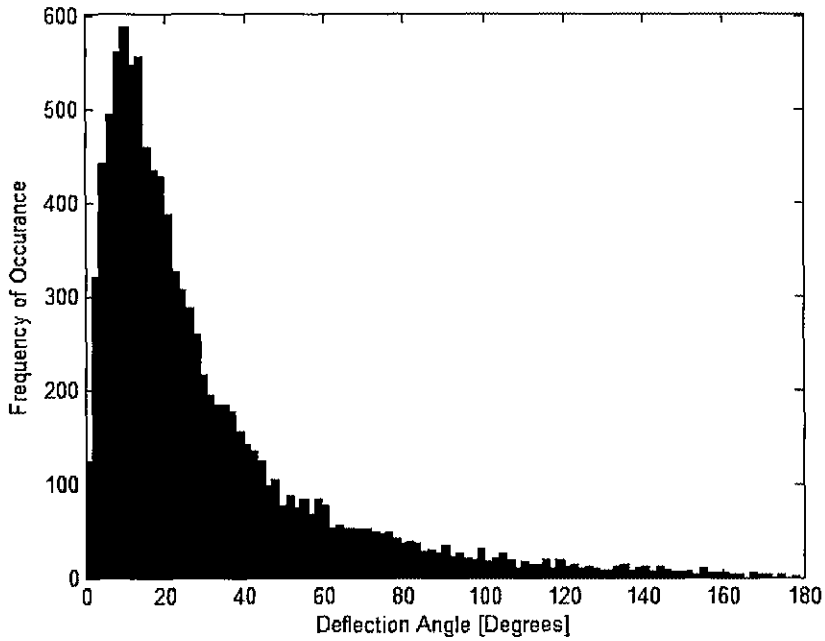

Fig 5.4. Histogram of the deflection angle for the anisotropy factor g = 0.79.

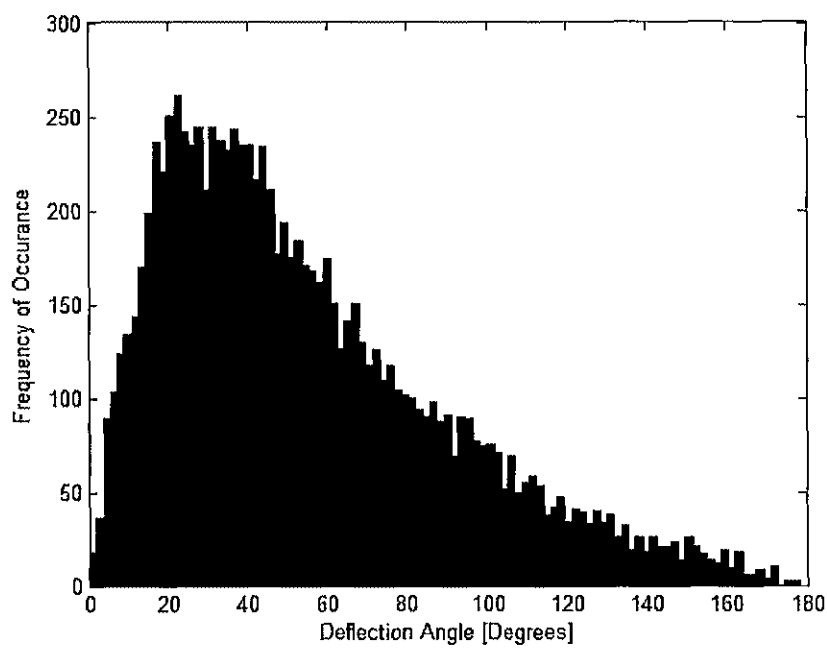

Fig 5.5. Histogram of the deflection angle for the anisotropy factor g = 0.5.

The energy of the single incident photon was calculated using its wavelength as:

$$E_{single} = \frac{hc}{\lambda}, \tag{5.1}$$

where "h" is the Planck's constant, and "c" the velocity of light.

The scaling factor that has been used for weighing each simulated photon entity was calculated as:

$$W = \frac{E_{total}}{E_{single} * N} \tag{5.2}$$

The reason for such a weighing is that each simulated photon represents, in reality, a larger number of actual physical photons. This becomes necessary for computational ease, since otherwise a very large number of actual photons would have had to be used in the simulation. For purposes of terminating the path of a traversing photon, a minimum energy E_{min} threshold for photon "death" was used and set to some low, fixed value. In these simulations, $E_{min} = W * 10^{-4}$, so that at each photon propagation step, the new scaled energy was compared with E_{min} . Thus, whenever the energy of any propagating photon fell below the E_{min} threshold, the photon was terminated and assumed to be buried at that location. This denotes a situation wherein the energy remaining with a photon is too low to cause further energy deposition or any propagation of any significance. Hence, there is no real information gleaned by tracking such a low-level photon energy-entity. The various layers parameters used in the present simulations are listed in the table 5.1.

Table 5.1. List of parameter values for different tissue layers used in the simulation.

Layers / Parameters	Stratum cornea	Epidermis	Dermis
Thickness (width)	15 x10^{-6} m	56 x10^{-6} m	1123 x10^{-6} m
Absorption Coefficient (μ_a)	200 m^{-1}	3600 m^{-1}	200 m^{-1}
Scattering Coefficient (μ_s)	10000 m^{-1}	47000 m^{-1}	20500 m^{-1}
Refractive index (n)	1.52	1.34	1.40

5.3 Calculation of Energy Absorption

Photons that are incident on the tissue propagate into it with continuous energy deposition, internal reflection at the layer boundaries and scattering events after random propagation distances (i.e., the spatial steps). At each step, the energy deposited by the photon entity is calculated using equation 4.14 presented in chapter 4. The absorbed energy can then be plotted against the distance travelled by the photons along the tissue depth (z-direction). This provides a profile of the energy source term that then leads to heating.

If the parameters, i.e., the absorption co-efficient, scattering co-efficient and also the refractive index of all the three layers, are taken to be as the same, then all the tissue layers appears as one continuous single-layer without any heterogeneity. In this case, the energy deposition can be expected to decrease with depth exponentially, satisfying the Beer-Lambert law. Given this expected result, this simple uniform tissue case was

numerically simulated, and used as a confirmation and validation of our numerical implementations. Figures 5.6, 5.7, 5.8 and 5.9 shows the energy deposited in the tissue as a function of depth when the absorption and scattering co-efficients were chosen to be: $\mu_a = 3600\ m^{-1}$ and $\mu_s = 47000\ m^{-1}$ and for anisotropy factors g = 0.9 and g = 1. To have a better picture and resolution of the changes in the energy deposition, they are plotted on both linear and logarithmic scales.

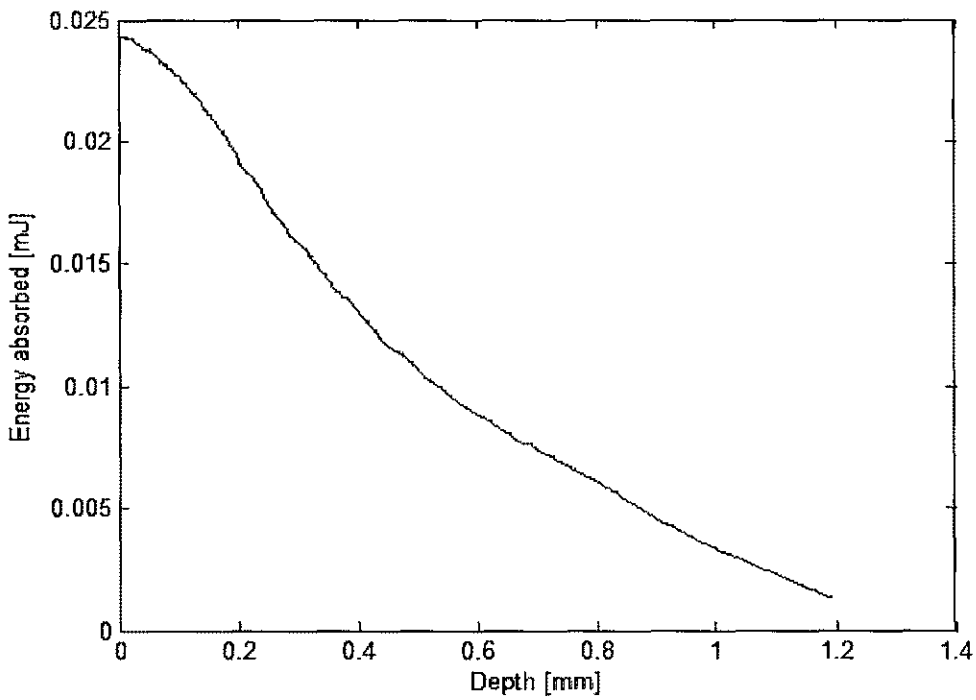

Fig 5.6. Energy absorbed by the tissue as a function of tissue depth for g = 0.9.

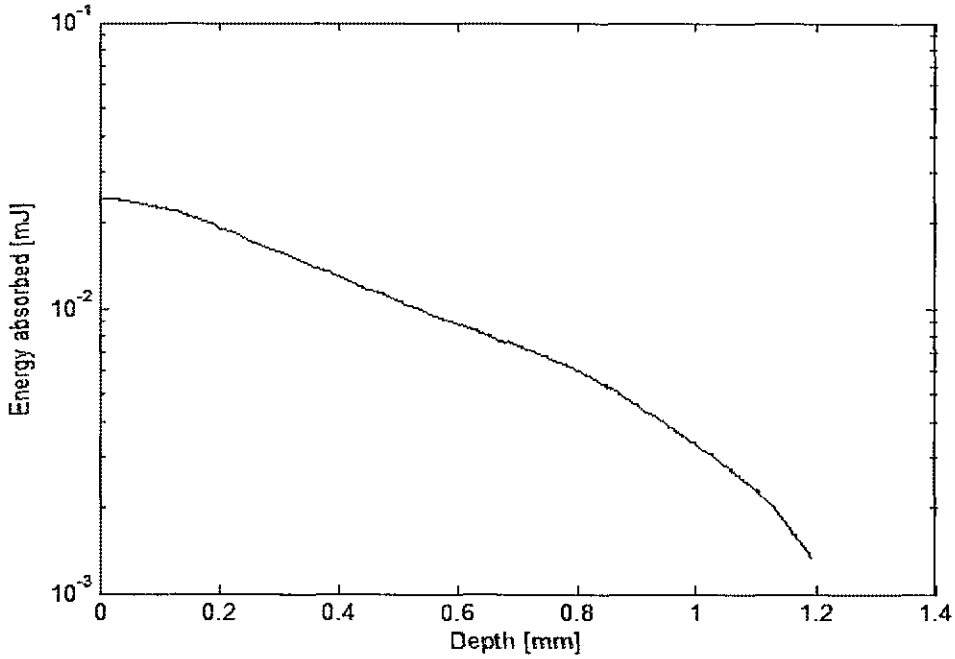

Fig 5.7. Energy absorbed by tissue (log scale) as a function of tissue depth for g = 0.9.

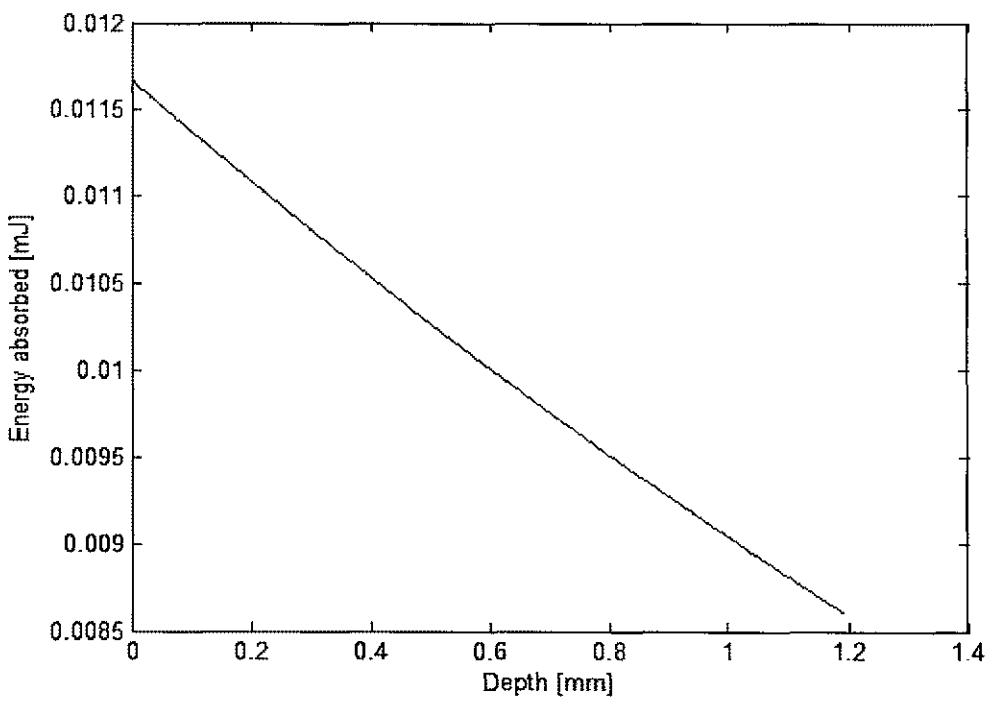

Fig 5.8. Energy absorbed by the tissue as a function of tissue depth for g = 0.9.

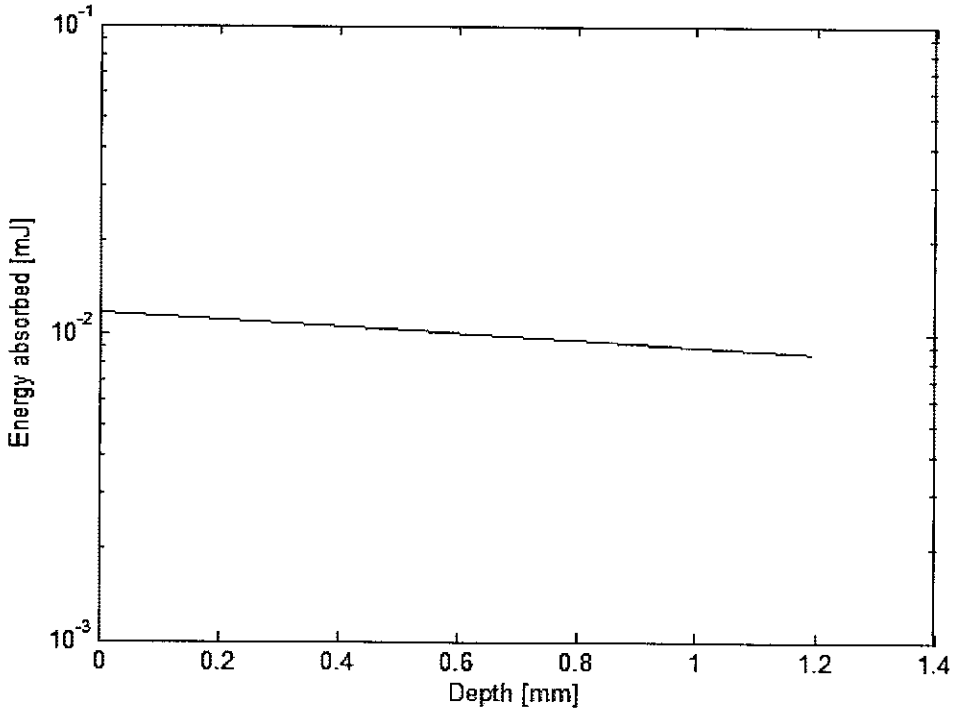

Fig 5.9. Energy absorbed by the tissue (log scale) at different tissue depths when g =1.

Next, all three layers (namely the stratum cornea, epidermis and dermis) were considered with their respective input parameters as listed in table 5.1. The energy deposited in their respective layers was calculated and the results presented in figures 5.10 and 5.11. Discontinuities in the energy deposition plot occur at the boundaries of the various layers. This is due to differences in the absorption and scattering co-efficients of the individual layers.

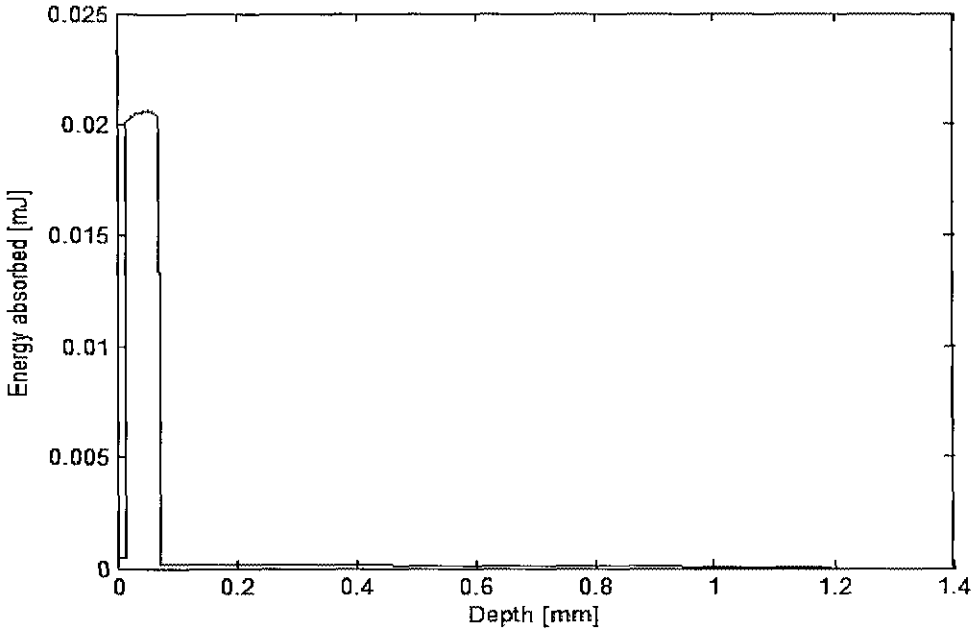

Fig 5.10. Energy absorbed by the tissue at different tissue depths with g = 0.9.

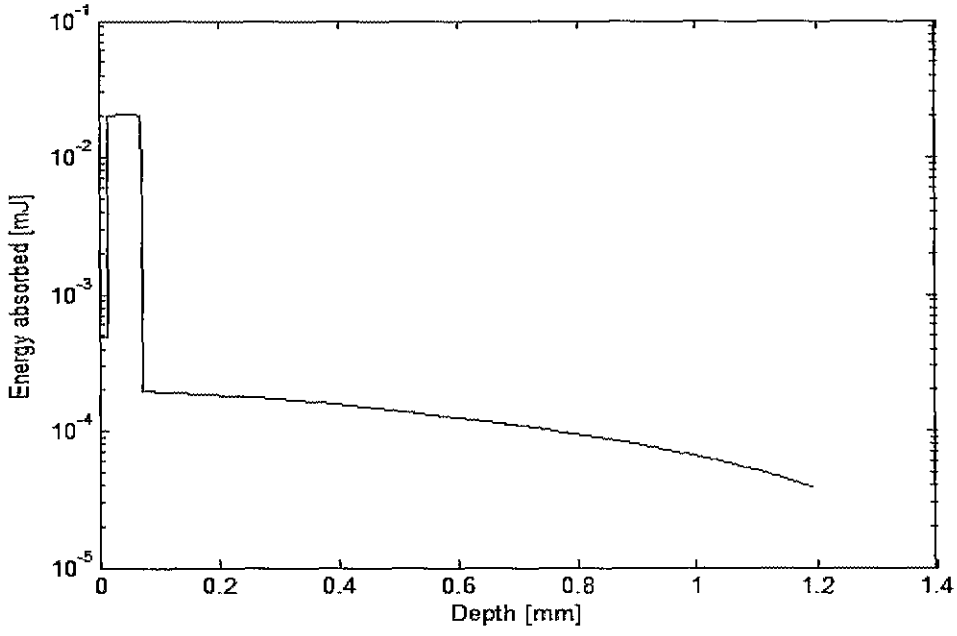

Fig 5.11. Energy absorbed by the tissue (log scale) at different tissue depths with g = 0.9.

5.4 Heat Generation and Temperature Changes due to Absorbed Energy

The energy absorbed by the tissue generates heat within the tissue. This should then lead to temperature increases within the bio-tissue region. Here a cylindrical coordinate system was used to quantify energy absorption and was tallied into an array A[i,j] with i and j denoting the indices in the z and r directions, respectively. A grid system was set up within the Monte Carlo simulation with $N_r = 200$ and $N_z = 5000$ as the number of grid elements along the r and z direction, respectively. The grid spacing was taken to be uniform and constant. As it turned out, of the total 5,000 grid points along the depth, only the first 1200 (or so) grid elements contained useful, non-zero information, with the remaining grid points having negligible deposited energy values. The latter simply reflects the relatively larger simulation thickness as compared to the absorption depths. Laser pulses of 10 ms duration were considered to be incidental on the tissue, with a lateral Gaussian distribution. Blood was considered to be flowing beneath the lower tissue layer dermis that maintained the temperature at a constant value. Similarly, the temperature above the top layer stratum cornea was assumed to be at a constant 300 ^{0}K value, representing the ambient temperature. The Pennes bioheat transfer equation, as discussed in section 4.3 of chapter 4, was used in the evaluation of the temperature changes in the tissue due to incidental laser pulse.

The computer code developed to solve the Pennes bioheat transfer equation and estimate temperature distributions was first validated by testing it for a simple case of a single layer. Different combinations of the initial tissue temperature, ambient temperature above the tissue, and blood temperature were used to generate different test cases. As a first step, laser excitation was not considered for simplicity. Thus, the tissue temperature

is affected only by the ambient temperature and blood temperature. Due to thermal diffusion, changes in temperature at each location in the tissue take place, when the blood and the ambient temperatures are different, until a steady-state is reached. If the input parameters of all three layers are set as the same, then the three layers represent a single layer. Here, for the initial purposes of testing, they were all set to equal to those of the stratum cornea layers as listed in table 5.2.

As a first case, the initial temperature of the tissue, ambient temperature, and the tissue temperature were taken to be the same (310 ^{0}K), and the temperature at different tissue depths were calculated based on the numerical bio-heat code. It was observed that there was no change in tissue temperature, as might be executed since there were no assigned differences in temperatures between the tissue. With equal temperatures for the ambient and the underlying blood, no thermal diffusion was possible and hence the tissue temperature remained stable as expected. Temperatures at different tissue depths are presented in figure 5.12 below.

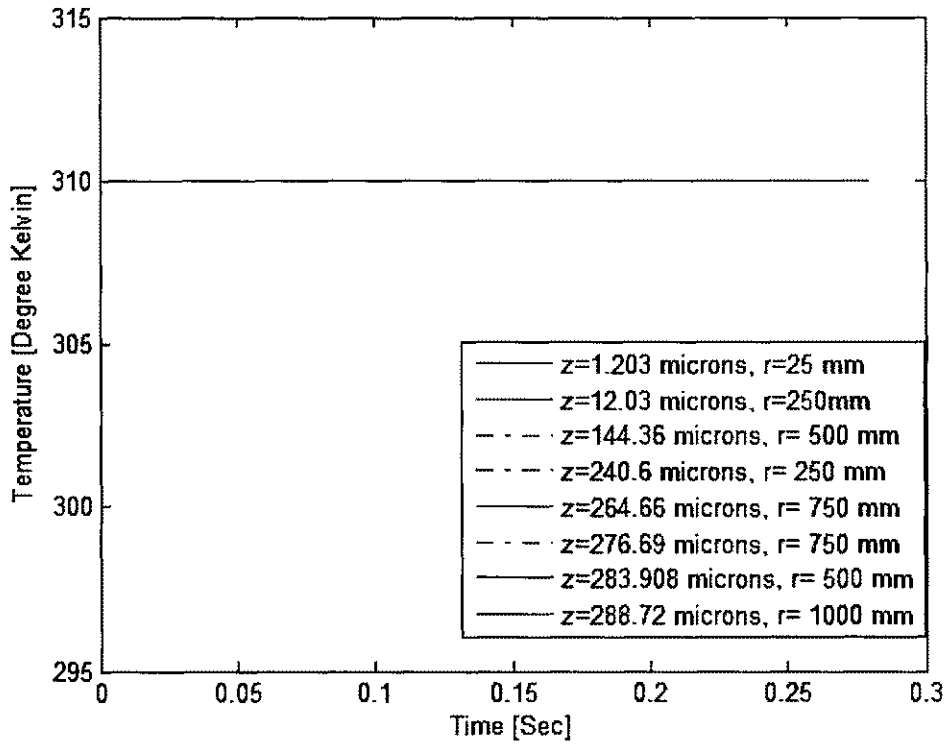

Fig 5.12. Temperature variations at different tissue depths during the simulation period of 280 ms when the ambient temperature, tissue temperature and temperature of blood were all set equal in value.

As a second case, the initial tissue temperature and the blood temperature are considered to be the same and taken to be 310 ^{0}K , while the ambient temperature was set at 300 ^{0}K. The temporal evolution of the temperature as a function of depth was simulated. It was observed that the upper part of the simulated tissue region had lower temperatures during the simulation period. Also, as the depth increased, the tissue temperatures also increased correspondingly. This is as expected since the upper part of the tissue is closer to air which is at the lower 300 ^{0}K temperature, while the bottom surface was taken to be at the higher 310 ^{0}K temperature. The results are shown in figure 5.13 below.

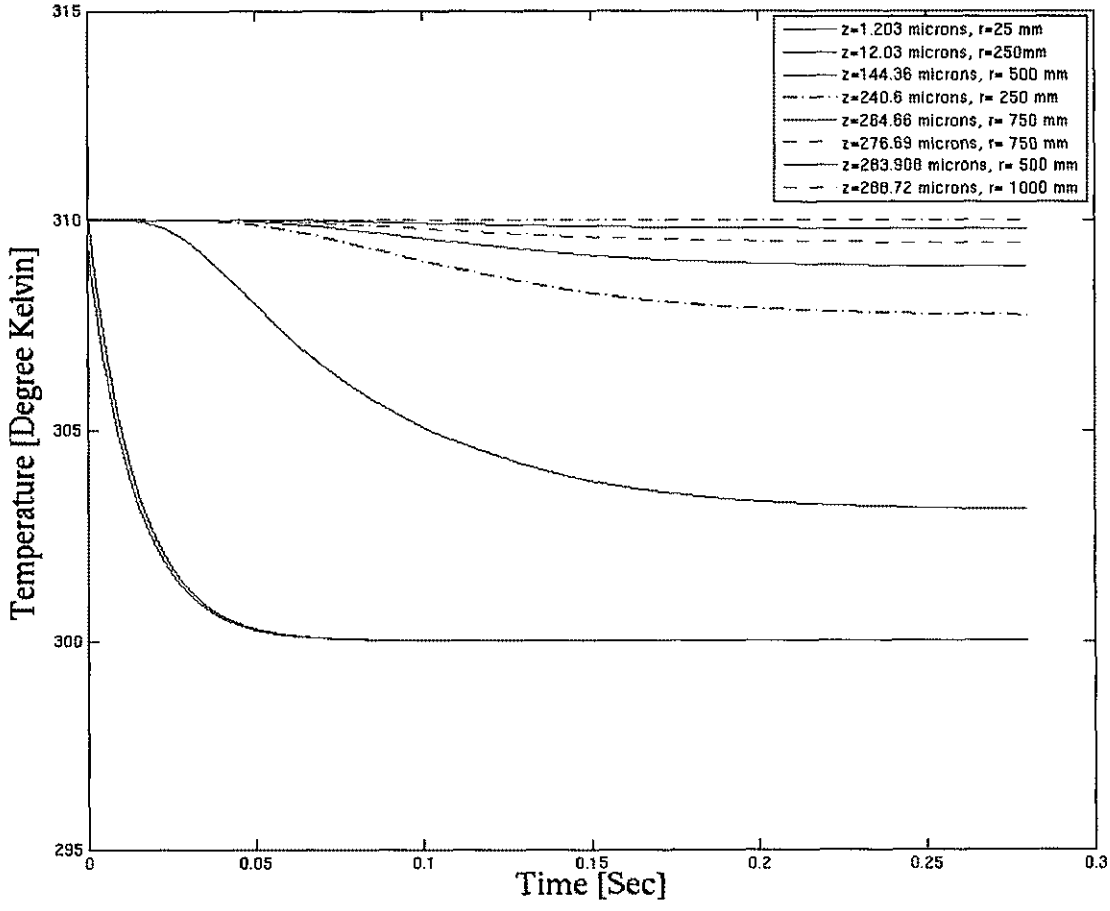

Fig 5.13 Temperature variations at different tissue depths during the simulation period of 280 ms when the tissue and blood temperatures of blood were set equal to 310 ^{0}K, while the ambient temperature was taken to be 300 ^{0}K.

In the third case, the temperatures of the tissue, the ambient and the blood were considered to be different. The ambient temperature was taken as 300 ^{0}K, the tissue as 310 ^{0}K, and the blood temperature to be 309.4 ^{0}K. Here the temperature at distances closer to the surface was low, and as the depth increased the temperature increased. Finally, towards the end of the tissue, the temperature fell somewhat due to the slightly lower blood temperature chosen. This is expected since the top surface exposed to the air

had the lowest temperature, the initial tissue temperature was the highest, while the bottom part had a fixed value slightly lower than the initial tissue temperature. The temperatures at different depths are presented in figure 5.14 below.

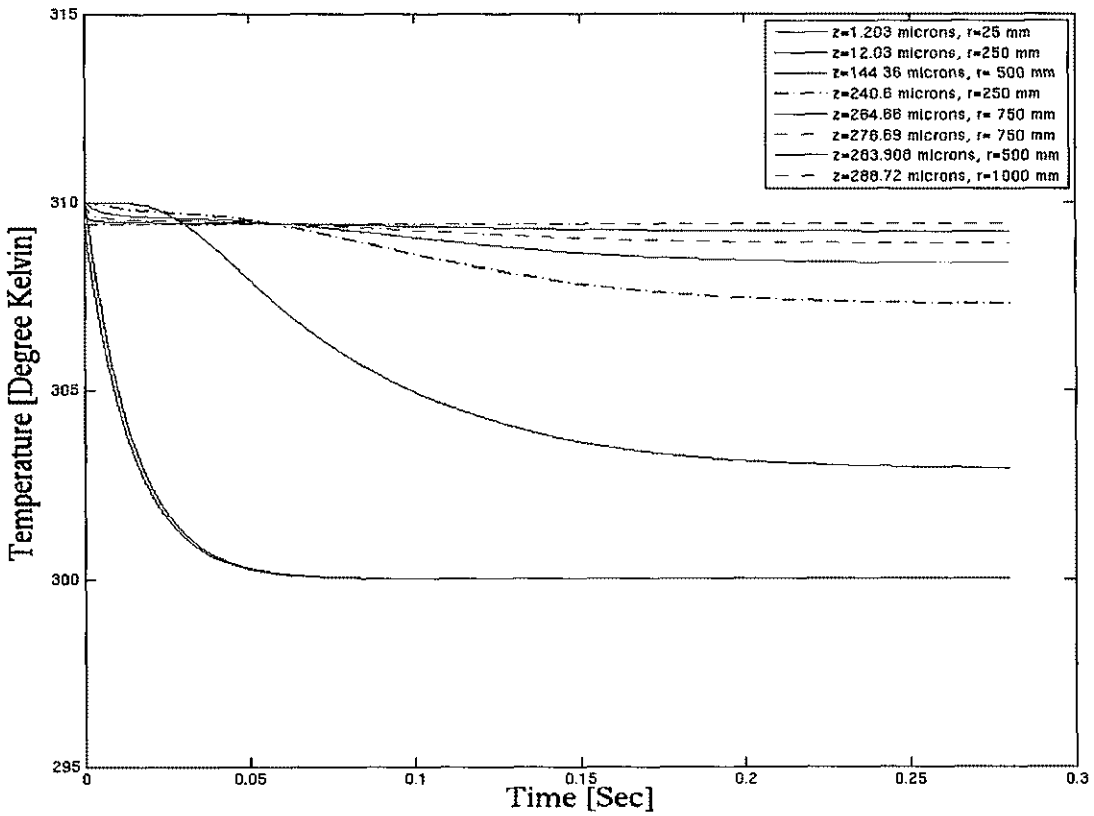

Fig 5.14. Temperature at different time instances at different depths on the tissue after a simulation time of 280 ms when the initial temperatures of ambient, tissue, and blood are all taken to be different.

From the above simulations it can be concluded that the developed computer code works fairly well and produces results that are physically expected and qualitatively correct. Hence, the bio-heat code can be applied to layered model analyses.

The above bio-heat model was then applied to a three layered tissue sample, with the input parameter values for the model listed in table 5.2. A laser pulse of pulse width 10 ms was considered to be incidental on the tissue and tissue temperature variations were observed after a simulation time period of 25 ms.

Table 5.2. List of parameter values used in the simulation to evaluate temperature distribution.

Parameters	**Value [units]**
Initial temperature (t_{init})	310 [^{0}K]
Ambient temperature (t_{amb})	300 [^{0}K]
Simulation time (t_{sim})	25 [ms]
Pulse width (t_{pulse})	10 [ms]
Width of stratum cornea (widzsc)	15x10^{-6} [m]
Width of epidermis (widzep)	56x10^{-6} [m]
Width of dermis (widzder)	1123x10^{-6} [m]
Thermal conductivity of stratum cornea(K)	0.37 [W/(m K)]
Thermal conductivity of epidermis(K)	0.26 [W/(m K)]
Thermal conductivity of dermis(K)	0.53 [W/(m K)]
Blood perfusion rate (W_b)	0.5 [kg/(m^3 s)]
Thermal conductivity of blood (K_b)	0.53 [W/(m K)]
Specific heat of tissue (C)	4.1x10^{-3} [J/(kg K)]
Specific heat of blood (C_b)	4.1x10^{-3} [J/(kg K)]

Heat transfer coefficient (h)	5000 [$Wm^{-2}K^{-1}$]
Tissue density (ρ)	$1.1x10^{-3}$ [kg/m^3]
Metabolic rate of tissue (Q_m)	1.1x ρ [W/m^3]
Volumetric heating rate (Q_r)	0 [W/m^3]

The peak temperature observed during the simulated time in the simulated area is plotted and presented in figure 5.15. The tissue temperature increases gradually for the duration of focused laser beam; and the tissue then starts to cool down as soon as the beam ends. Thus, in figure 5.15, the peak temperature increases with time until 10 ms. This duration corresponds to the laser pulse duration. The temperature starts to decrease exponentially after the pulse is terminated.

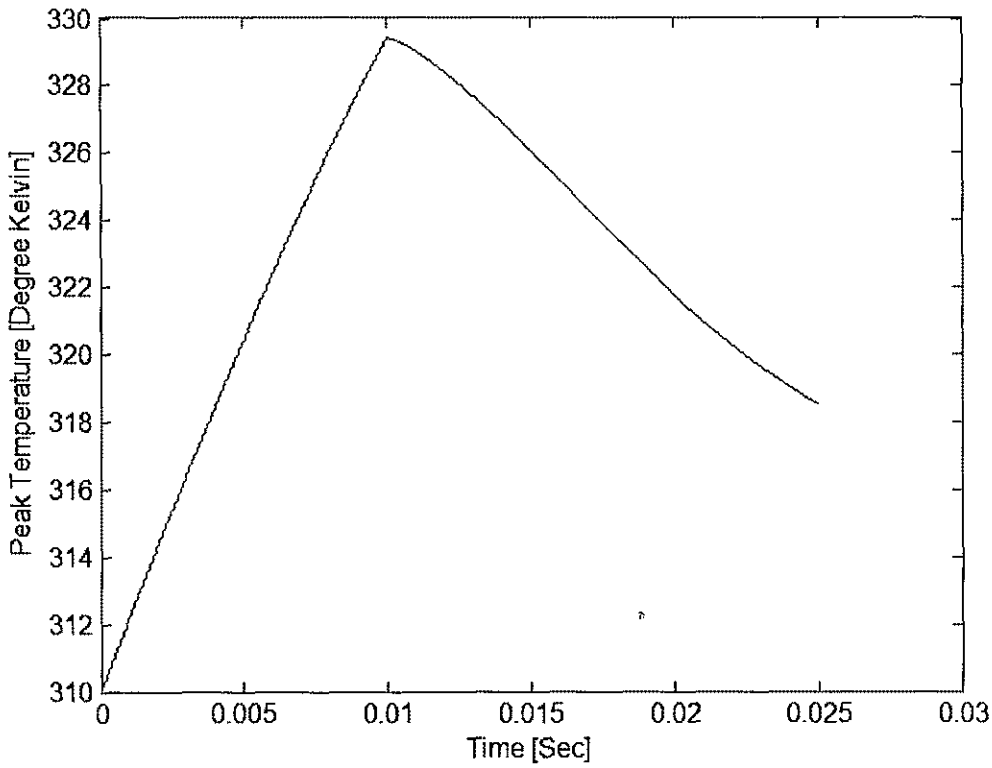

Fig 5.15 Simulation results of the peak temperature observed in the tissue as a function of time in response to a 10 ms laser pulse incident on the surface.

The temperature distribution in the tissue at the end of the simulation time period for the case discussed above, is presented in figure 5.16.

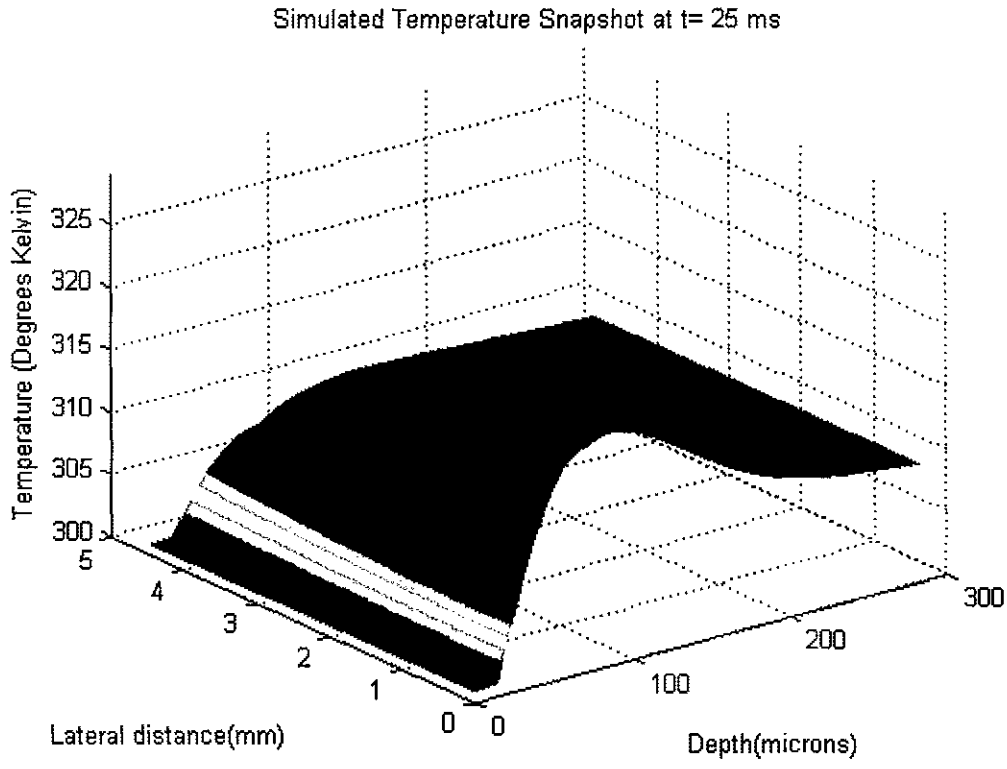

Fig 5.16. Snapshot of temperature distribution within the tissue at the 25ms instant.

In order to better see the tissue temperature evolution during the simulation period, temperature distributions in the tissue at different time instants were calculated and are presented in figure 5.18. A more complete video showing the tissue temperature at different time instances was developed, but here only the snapshots are provided for brevity.

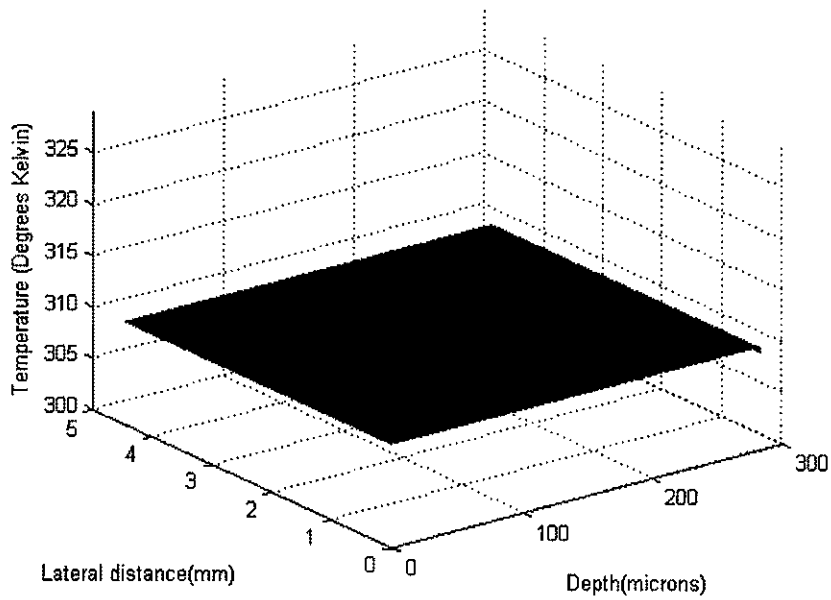

Fig 5.17(a). Snapshot of initial temperature distribution within the tissue at 5E-8 s instant.

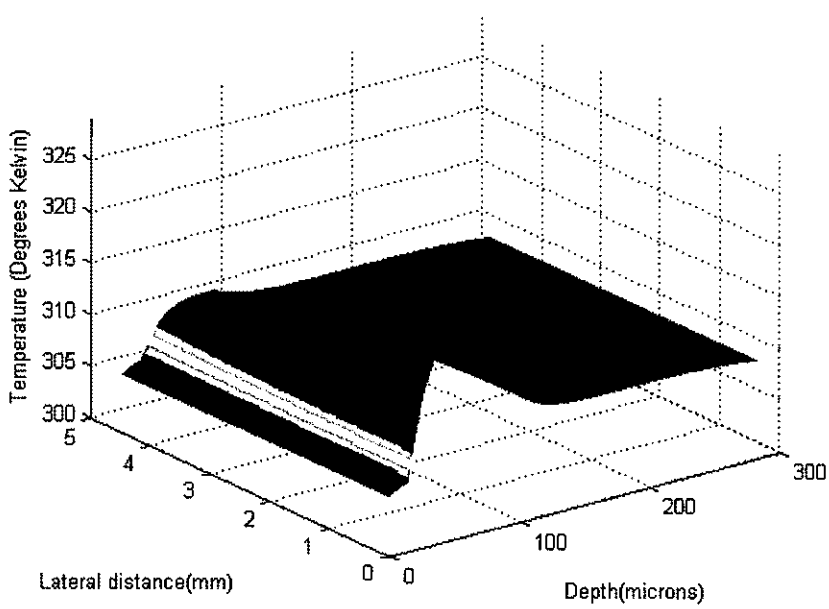

Fig 5.17(b). Snapshot of temperature distribution within the tissue at the 5 ms instant.

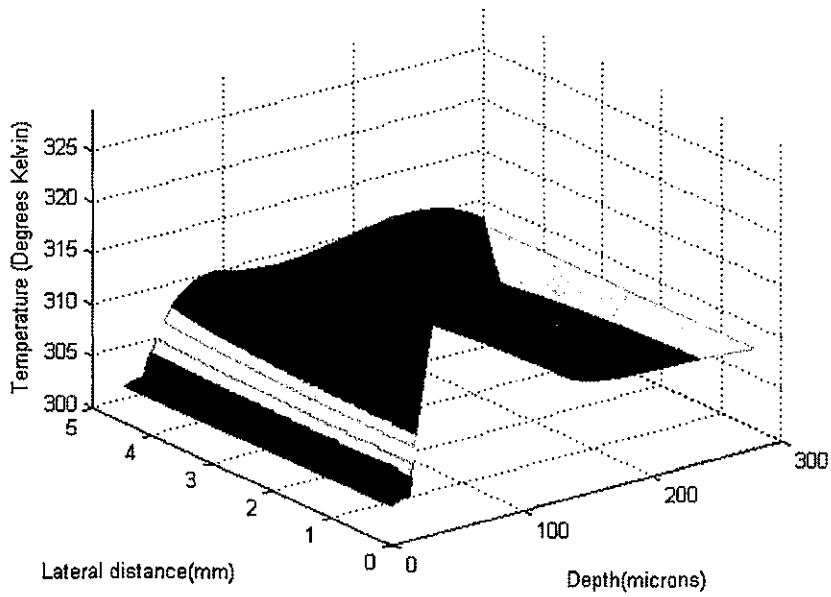

Fig 5.17(c). Snapshot of temperature distribution within the tissue at the 10 ms instant.

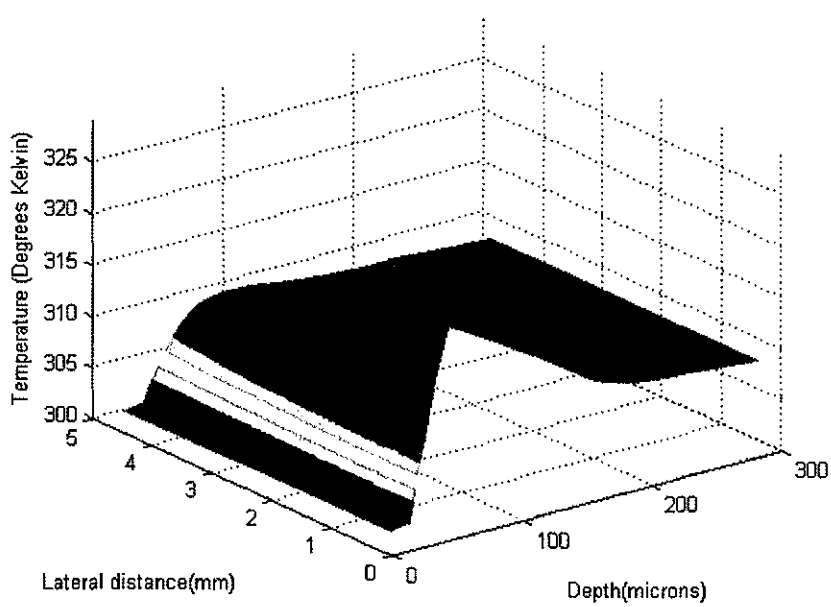

Fig 5.17(d). Snapshot of temperature distribution within the tissue at the 15 ms instant.

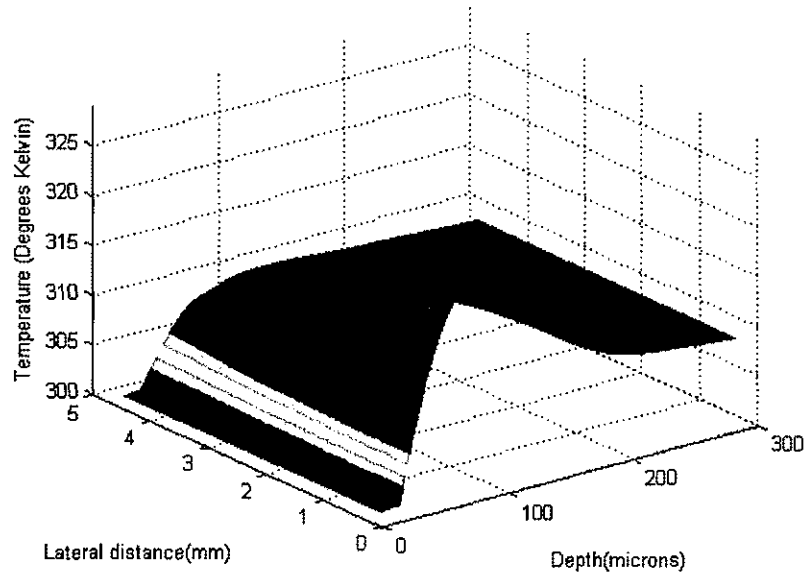

Fig 5.17(e). Snapshot of temperature distribution within the tissue at the 20 ms instant.

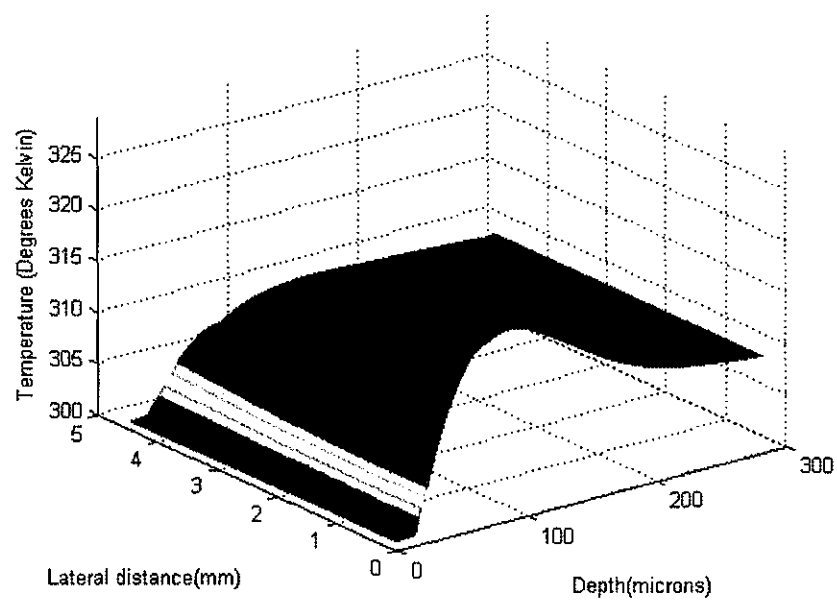

Fig 5.17(f). Snapshot of temperature distribution within the tissue at the 25 ms instant.

5.5 Results and Discussion on the Phase Behavior of Incident Photons

The model developed to include phase behavior of light, and the results obtained from it are discussed in this section.

5.5.1 Calculation of Intensity

The phase model and its implementation was applied to the following specific geometry as a concrete example. A light source "S" was taken and considered to launch rays of a given wavelength λ uniformly over a semicircle, with this source "S" being at the center. A value of λ = 585 nm was used. The rays emitted from this source reached an aperture placed at a distance 10000λ from the source line. This aperture was taken to have two openings. These two openings (slits) were separated by distances 30λ on either side of the center of the aperture. The two openings were thus considered to be present at (0, 30λ) and (0,-30λ) in a Cartesian coordinate system, with the center of the aperture located at: (0, 0). In principle, these two openings act as two sources (S_1 and S_2) and emit rays of the same 585 nm wavelength. These two points S_1 and S_2 then effectively, become two secondary sources. All the rays emitting from these sources were taken to have unit intensity and zero initial phase. The phase angles of the rays change as they move, and the moving rays finally reach the detector located at a distance of 10,000λ. This detector was considered to be placed at a distance of 10,000λ from the aperture. The model setup is depicted schematically in figure 5.19.

By tracking the distances travelled by the rays, the phase changes can be calculated and thereby, the intensities of the photon-rays at the detector points can be computed. The resultant intensity at any location is the phasor sum of all the ray intensities that reach the

same location, and are calculated by using equation (4.27) presented in chapter 4. Thus the impact of phase changes on the resultant intensities can be predicted. The intensities observed at the detector by using a deterministic model are shown in the figures below. Basically, $2x10^6$ rays were considered to be emitted uniformly over an angle ranging from $\left(-\tan^{-1}\left(\frac{530\lambda}{10000\lambda}\right), \tan^{-1}\left(\frac{530\lambda}{10000\lambda}\right)\right)$ about a normal to the source line, from each of the sources S_1 and S_2. The detector was divided into small bins and the resultant intensity at a particular bin computed as the phasor sum of all the ray intensities falling into that particular bin.

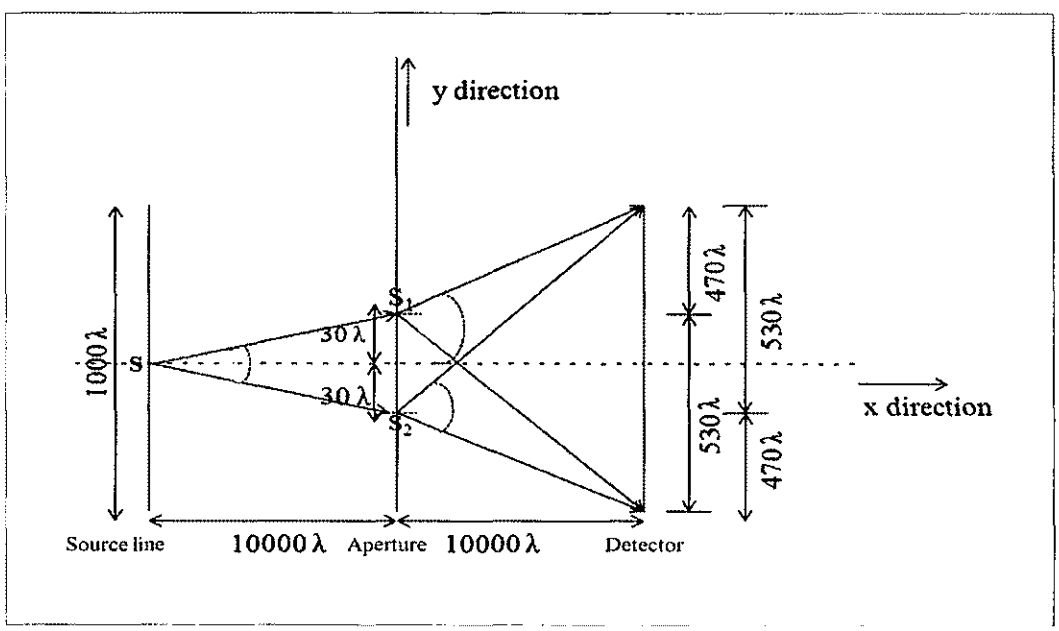

Fig 5.18. Model setup to show the influence of phase on the photon intensities.

Figure 5.20 below shows the normalized intensities at all locations on the detector when the detector is divided into 10000 bins each of length 0.1λ. Due to differences in

the rays' phase angles at different locations, the intensities at all locations on the detector are not the same. As the two sources are equidistant from the center of the aperture, symmetry about the center of the detector is expected and observed. Also not surprisingly, the maximum intensity is observed at the center of the detector.

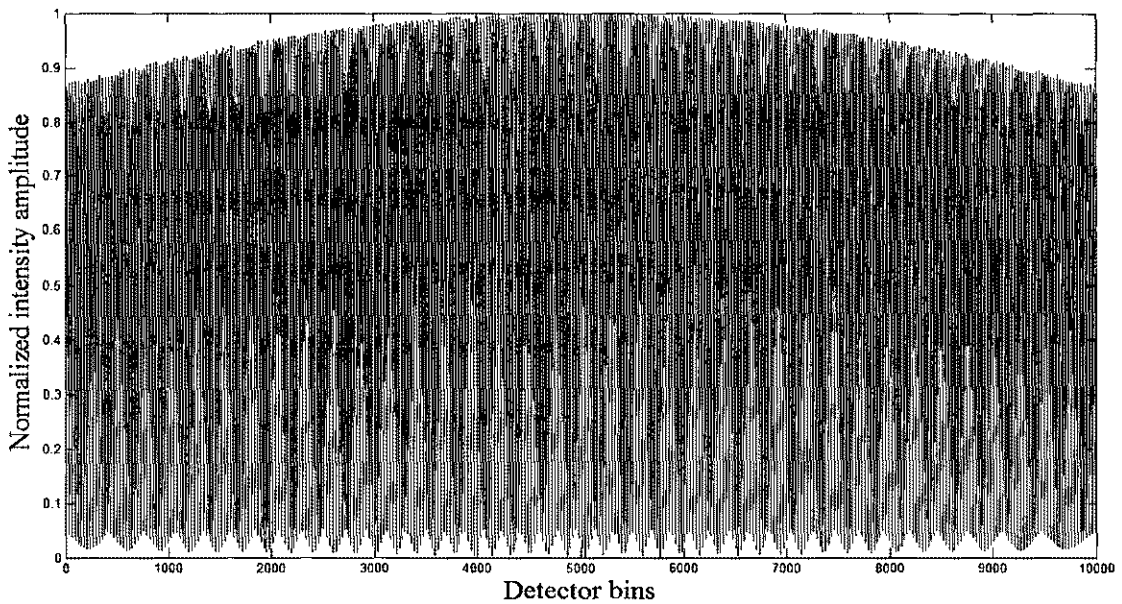

Fig 5.19. Normalized intensities observed at different locations on the detector when spatial bin size was taken to be 0.1λ.

For clarity and to show the variations in intensities and the symmetry, only the top and bottom 200 bins on the entire detector were plotted. These graphs have been shown in figures 5.21 and 5.22. From these figures, the symmetry and the affects of phase angles can be clearly observed.

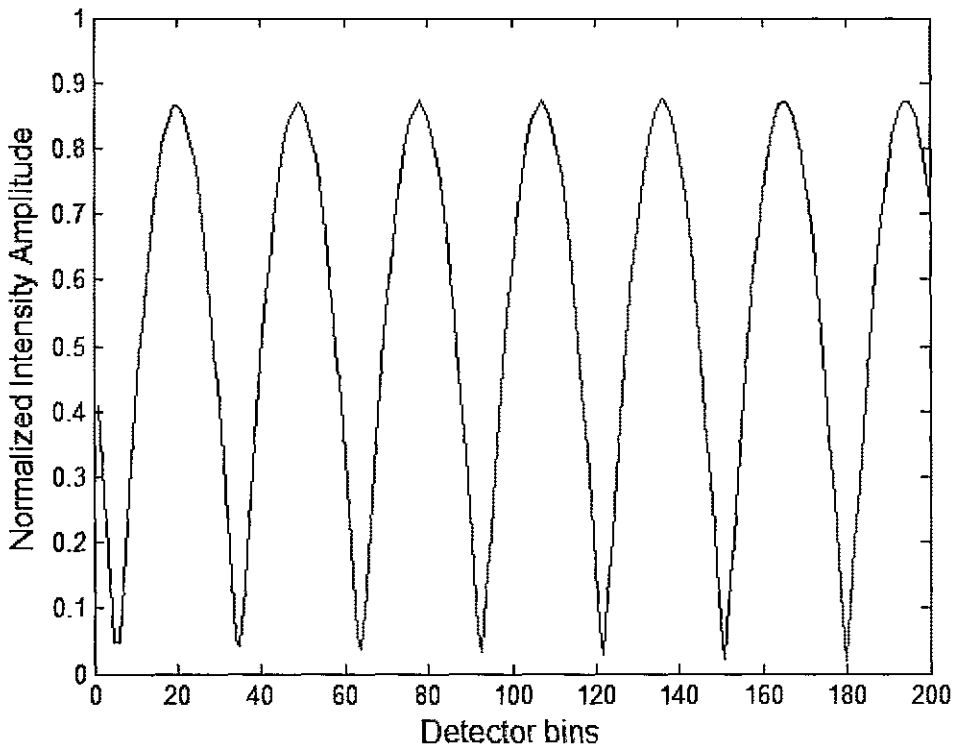

Fig 5.20. Normalized intensities observed on upper part (200 bins) of the detector when bin size was taken to be 0.1λ.

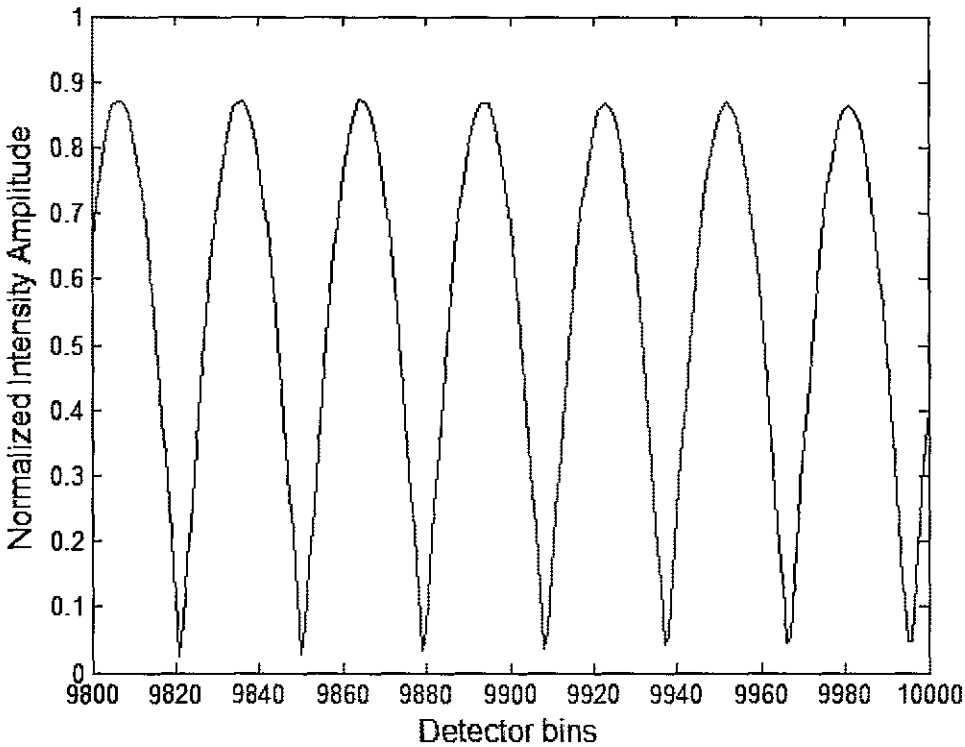

Fig 5.21. Normalized intensities observed on lower part (200 bins) of the detector when bin size was 0.1λ.

5.5.2 Monte Carlo Model

The Monte Carlo technique was used to determine the intensities stochastically as discussed in section 4.5 of chapter 4. Changes in the phases as the rays propagate, along with the scattering events, were taken into account. The calculated intensities at different locations on the detector were compared with that of the deterministic model already discussed. The model set up was the same as that used for the deterministic model discussed in section 5.5.1. In this model, after each photon propagation step Δs, its phase changes and the photon scatters. By keeping track of all the step sizes (free mean paths), the total path length of the photon to reach the detector can be calculated and hence the phase of the photon when it finally reaches the detector, can be determined. Knowing the

phase angles of the photons incident on the detector, the intensities on the detector can be obtained. Here the anisotropy factor g was taken to be g = 0.9, but our procedure is general, and any other value could easily have been used as well. The absorption and the scattering co-efficient μ_s were taken to be $\mu_a = 36$, $\mu_s = 47$. These values were chosen for simplicity to limit the number of propagation steps before the photon reached the detector, but these values can easily be changed. Here the two sources, S_1 and S_2 were considered to launch $2x10^6$ rays each, uniformly over an angle ranging from $\left(-\tan^{-1}\left(\frac{530\lambda}{10000\lambda}\right), \tan^{-1}\left(\frac{530\lambda}{10000\lambda}\right)\right)$ about a normal to the source line. The rays that were back scattered were ignored from numerical consideration. The detector was divided into 10000 bins each of 0.1λ and rays that fell into the bins were added coherently. It was observed that around 73 % of all the emitted rays reached the detector and the rest were either back scattered or were out of the detector zone. The intensities on the detector were plotted and are shown in figure 5.23 below. To show the variations in intensities more clearly, only the beam intensities of the top and bottom parts of the detector (200 bins) were plotted and are presented in figures 5.24 and 5.25.

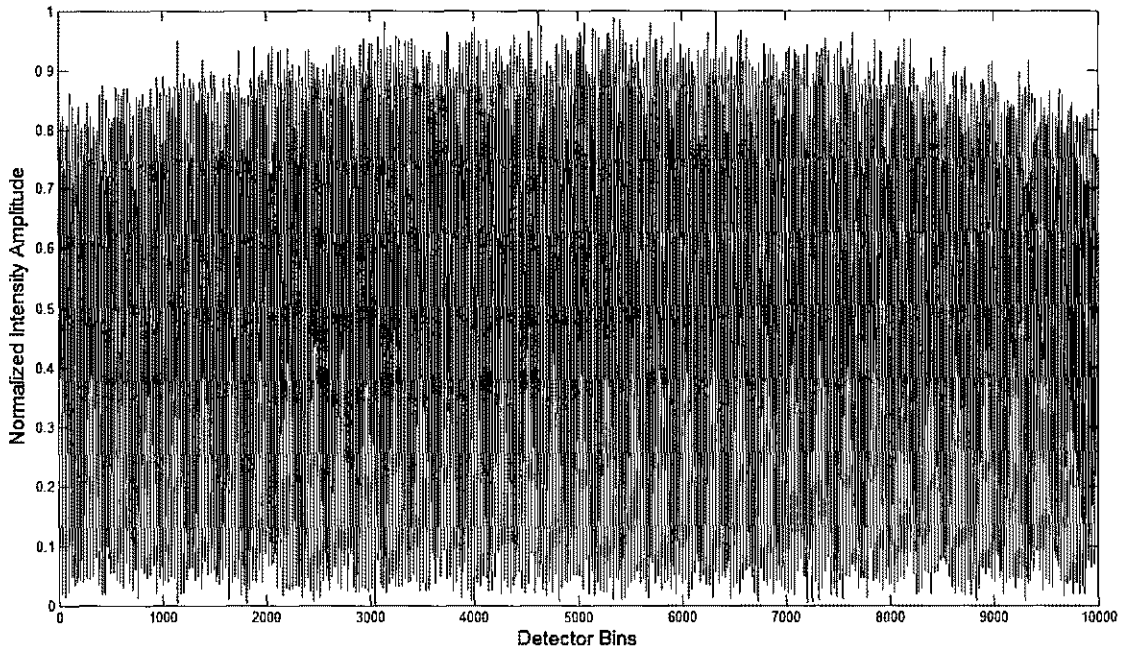

Fig 5.22. Normalized intensities observed at different locations on the detector using the Monte Carlo model for a bin size of 0.1λ.

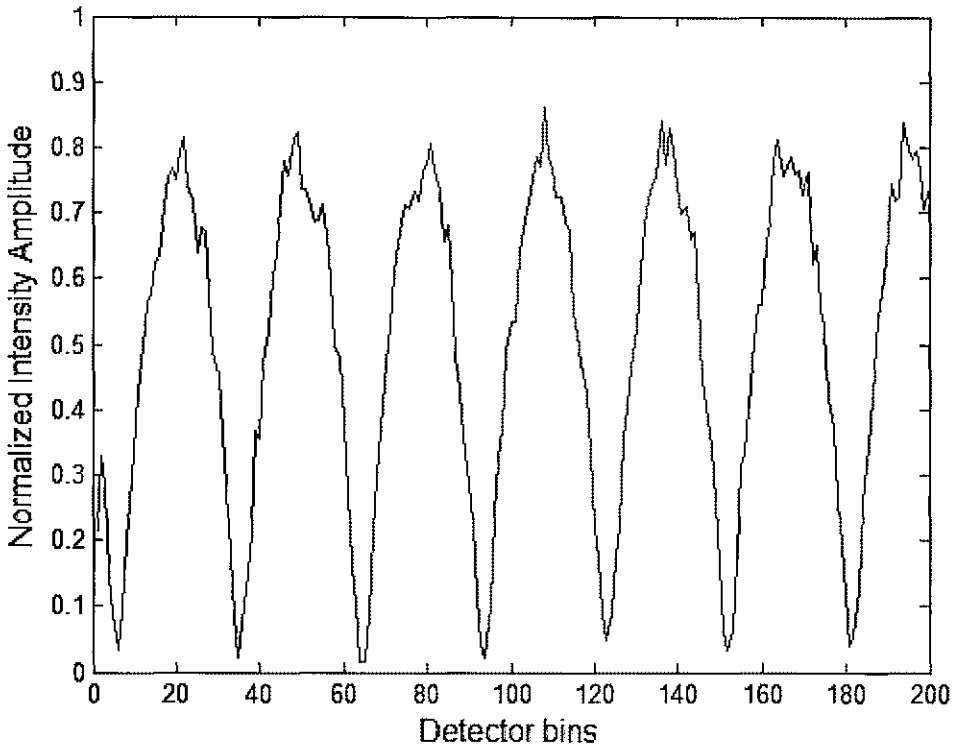

Fig 5.23. Normalized intensities observed on upper part of the detector (200 bins) whose bin size was 0.1λ.

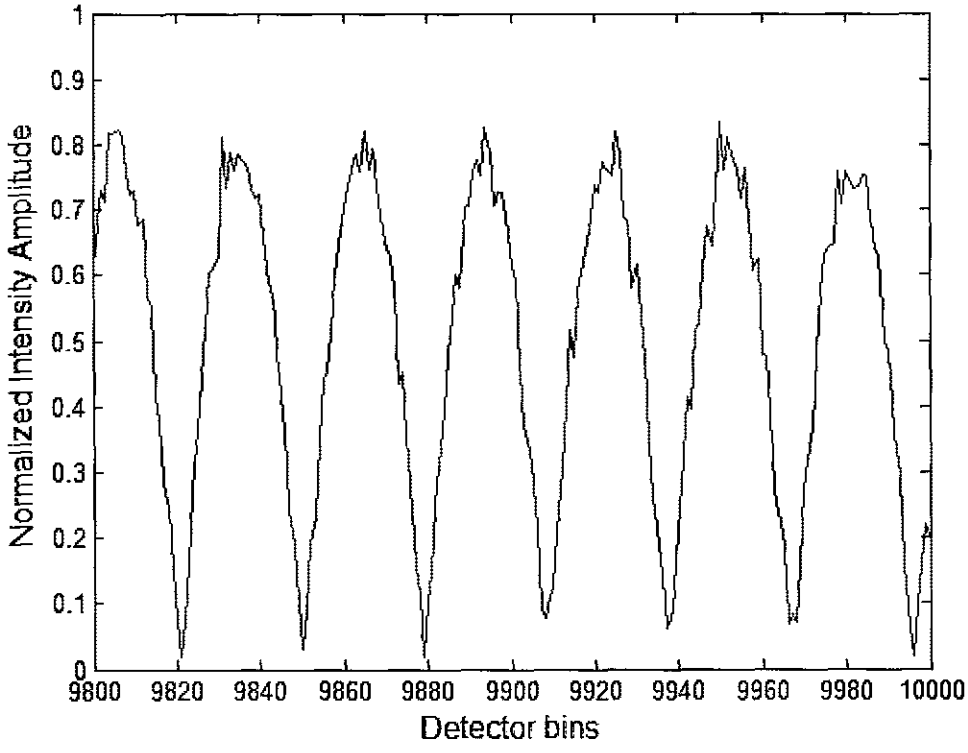

Fig 5.24. Normalized intensities observed on lower part (200 bins) of the detector whose bin size is 0.1λ.

Each ray takes multiple propagation steps to reach the detector. If the number of photons are increased and/or if the higher (or more general) values of absorption and scattering co-efficients are taken, then the overall propagation steps as well as the scattering events would greatly increase. This would increase the simulation time and increases both the computational complexity. In order to avoid this complexity a simple technique called "Transfer Matrix approach," which is based on the Monte Carlo scheme, could be used. This alternative approach for inclusion of the phase aspects of photon propagation is being proposed as a numerically simpler, yet accurate scheme, and can be implemented in future works.

CHAPTER VI

CONCLUSIONS AND FUTURE WORK

6.1 Summary

A three-dimensional, computer-based Monte Carlo model was developed to simulate laser tissue interactions and to study the effects of laser heating of bio-tissues. In this model photons were treated as a stream of neutral particles having discrete energies. The developed Monte Carlo technique has been implemented on a three layered tissue of the skin. This numerical approach has been used for calculating the energy deposition by the incident laser onto the tissue as a function of depth. Laser light of particular wavelength and energy was taken to be incidentally normal on the tissue's top layer. The top three layers of the skin tissue, namely, the stratum cornea, epidermis and the dermis were considered for the simulation. For this case, the relevant parameters, namely the layer thickness, the absorption and scattering co-efficients, the refractive indices, and the anisotropy factor were provided as user inputs to the numerical code. The significance of the anisotropy factor 'g' which can take any value between 0 and 1 was also studied. To demonstrate the model's validity and the accuracy, it was tested for a simple case of single layer tissue. It was shown that the energy deposition in a single layer followed an exponential decrease with increasing depth, thus satisfying the "Beer Lambert" law. As there were no changes in the layer parameters, in particularly no change in the absorption and the scattering co-efficients throughout the layer, the energy deposition in a single layer is exponential with increasing depth.

The laser energy deposited in the tissue generates heat, and this heat gets distributed internally due to the thermal diffusion process. This heat re-distribution and corresponding changes in tissue temperature were next evaluated through suitable simulations. A computer program was developed to observe the time dependent temperature variations within the tissue due to the incident laser pulse irradiation for specified time duration. This program was based on solving the Pennes bio-heat transfer equation. In these calculations, the ambient temperature condition was taken to be present above the tissue, and blood was considered to be flowing beneath the tissue. The energy deposition obtained from the Monte Carlo was used as input and temperature changes in the tissue due to the deposited energy were computed. To validate the accuracy of the program, it was tested for the simple case of a single layer using different combinations of ambient temperature, tissue initial temperature and the blood temperature. As a first step, temperature variations in the tissue at different tissue depths were computed without any laser pulse. The results obtained were in accordance with expectations, thereby validating the program's accuracy.

The above validation enabled the further development and use of the numerical model developed to estimate temperature changes in the tissue when excited by an external laser pulse. By estimating the temperature variations, it can be determined whether the laser power at that wavelength and irradiation duration would be efficacious, or disastrous and detrimental. The input parameters of the laser beam such as the wavelength, beam power, the spot size and the irradiation time could easily be varied in this model. Hence, effects of any laser on the bio-tissues could be predicted using this model. For accurate treatment such prior knowledge and predictions are necessary.

As is well known from basic physics, light or a laser beam exhibits a dual wave-particle nature. Hence, there is the necessity to understand the effects of phase changes and include the phase information as laser photons propagate within the bio-material. A two dimensional Monte Carlo simulation model based on Huygens Fresnel principle was developed to present the effects of phase changes, and provide quantitative predictions of the laser energy or intensity. In this model, the final phase of each photon or ray at the observation plane was found by tracking the distance travelled by that photon before it reached the observation plane (or detector). The model was implemented deterministically considering that rays emitted from the sources travelled in a straight line before reaching the detector. On the detector, the rays reaching the same point/location were added coherently and the intensities plotted to gauge the influence of phase changes on the intensities. Results did reveal a change in the intensity pattern with a periodic structure. In reality, however, the emitted rays do not travel in a straight line but instead, undergo a number of scattering events before reaching the detector. To include the scattering events and the phase information, a Monte Carlo model was developed and the intensities at the detector obtained. In this manner the effects of including scattering events on the overall changes in phase structure were analyzed. Thus effectively, a model was developed that included the dual wave-particle nature of the propagating rays. To implement the model for larger geometries and to reduce the computational burden of the Monte Carlo and achieve good accuracy, an efficient technique called the "Transfer Matrix approach" has been proposed.

6.2 Future Work

The developed Monte Carlo model of light propagation in tissue is very general and flexible in nature. A few "follow-on" tasks which could be implemented in the future are enumerated below.

1. The Monte Carlo model was implemented for only a three-layer tissue geometry for simplicity. However, the model is very flexible and versatile. Hence, it can easily be extended to any arbitrary number of tissue layers, provided the relevant parameters for the additional individual layers are user-specified. Just few minor changes in the computer program would be needed to extend to such a multi-tissue implementation.

2. In this model the boundaries separating the tissue layers were considered to be even (i.e., flat). However, in general the boundaries can be uneven. Hence, the model developed can be extended to include such unevenness and geometric irregularity. One possible method is to reduce the grid size to better approximate the curved boundaries or use piece-wise continuous approximations. As a result, much smaller tissue areas would need to be used. Alternately, curvilinear co-ordinate systems could be used.

3. The proposed Transfer Matrix approach to include scattering and phase changes can be implemented and used to increase the model efficiency. This method would reduce the computational time, especially for cases when both phase and scattering needed to be included.

4. The concept of a two-dimensional model to include phase changes within the propagating photons can be used to implement in a full three-dimensional Monte Carlo code for light propagation in tissues. This would make the model more realistic and comprehensive.

5. Finally, the temperature dependence of the various parameters used in the heat-flow model could be incorporated. Thus, the heat and laser-Monte-Carlo codes could be coupled for a self-consistent optical-thermal analysis.

REFERENCES

[1] D. Gazdaru, C. Chilom, M. A. Calin, C. Geanta, and A. Popescu, "Laser radiation propagation and heat transfer into cells and tissues," *Romanian Journal of Biophysics,* vol. 18, no. 1, pp. 73-85, 2008.

[2] M. Marozas, and R. Jurkonis, "Review on skin lesion imaging, analysis and automatic classification," *Conference Biomedical Engineering,* pp. 109-114, 2004.

[3] L. Wang, S. L. Jacques, and L. Zheng, "MCML - Monte Carlo modeling of light transport in multi-layered tissues," *Computer Methods and Programs in Biomedicine,* vol. 47, no. 2, pp. 131-146, 1995.

[4] M. Poetke, C. Philipp, and H. P. Berlien, "Flashlamp-pumped pulsed dye laser for hemangiomas in infancy," *Arch Dermatol,* vol. 136, no. 5, pp. 628-632, 2000.

[5] I. V. Meglinski, and S. J. Matcher, "Quantitative assessment of skin layers absorption and skin reflectance spectra simulation in the visible and near-infrared spectral regions," *Physiological Measurement,* vol. 23, no. 4, pp. 741-753, 2002.

[6] J. F. Dunn, and H. M. Swartz, *Oxygen transport to tissue XXIV,* New York: Kluwer Academic/Plenum, 2003.

[7] A. J. Welch, and M. J. C. van Gemert, *Optical-thermal response of laser- irradiated tissue*, New York: Plenum Press, 1995.

[8] R. Pierrat, N. B. Braham, L.F. Rojas-Ochoa, R. Carminati, and F. Sheffold, "The influence of the scattering anisotropy parameter on diffuse reflection of light," *Optics Communications,* vol. 281, no. 1, pp. 18-22, 2008.

[9] A. L. McKenzie, "Physics of thermal processes in laser-tissue interaction," *Physics in Medicine and Biology,* vol. 35, no. 9, pp. 1175-1209, 1990.

[10] W. S. Ho, H. H. Chan, S. Y. Ying, and P. C. Chan, "Laser treatment of congenital facial port-wine stains: long-term efficacy and complication in Chinese patients," *Lasers in Surgery and Medicine,* vol. 30, no. 1, pp. 44-47, 2002.

[11] C. M. A. M Van Der Horst, P. H. L. Kolster, C. A. J. M. De Borgie, P. M. M. Bossuyt, and M. J. C. van Gemert, "Effect of the timing of treatment of port-wine stains with the flash-lamp–pumped pulsed-dye laser," *The New England Journal of Medicine*, vol. 338, no. 15, pp. 1028-1033, 1998.

[12] M. Landthaler, and U. Hohenleutner, "Laser therapy of vascular lesions," *Photodermatol Photoimmunol Photomed Journal,* vol. 22, no. 6, pp. 324-332, 2006.

[13] Z. Gans, "Using the CO_2 laser for veterinary soft tissue surgery," *Israel Journal of Veterinary Medicine,* vol. 62, no. 3-4, pp. 72-73, 2007.

[14] A. L. McKenzie, "A three-zone model of soft-tissue damage by a CO_2 laser," *Physics in Medicine and Biology,* vol. 31, no. 9, pp. 967-983, 1986.

[15] W. Rao, Z. Q Sun, Y. X. Zhou and J. Liu, "Thermal infrared image to quantify nano particles enhanced laser deposition during malignant tissue ablation," *Proceedings of the 3rd IEEE Int. Conf. on Nano/Micro Engineered and Molecular Systems,* pp. 890-894, 2008.

[16] P. Moroz, S. K. Jones and B. N. Gray, "Status of hyperthermia in the treatment of advanced liver cancer," *Journal of Surgical Oncology,* vol. 77, no. 4, pp. 259-269, 2001.

[17] M. J. C. van Gemert and A. J. Welch, "Clinical use of laser-tissue interactions," *IEEE Engineering in Medicine and Biology Magazine*, vol. 8, no. 4, pp. 10-13, 1989.

[18] R. Pini, F. Rossi, P. Matteini, and F. Ratto, "Laser tissue welding in minimally invasive surgery and microsurgery," in *Biophotonics*, L. Pavesi, and P. M. Fauchet, Eds. Berlin, Heidelberg: Springer, 2008, pp. 275-299.

[19] A. C. Steger, W. R. Lees, K. Walmsley and S. G. Bown, "Interstitial laser hyperthermia: a new approach to local destruction of tumours," *British Medical Journal*, vol. 299, no. 6695, pp. 362-365, 1989.

[20] M. H. El-Tonsy, M. M. El-Domyati, A. E. El-Sawy, W. H. El-Din, T. E. A. Anbar, and H.A. Raouf, "Continuous-wave Nd:Yag laser hyperthermia: a successful modality in treatment of basal cell carcinoma," *Dermatology Online Journal*, vol. 10, no. 2, Article no. 3, 2009.

[21] A. V. Rode, E. G. Gamaly, B. Luther-Davies, B. T. Taylor, M. Gracssel, J. M. Dawes, A. Chan, R. M. Lowe, and P. Hannaford, "Precision ablation of dental enamel using a subpicosecond pulsed laser," *Australian Dental Journal,* vol. 48, no. 4, pp. 233-239, 2003.

[22] C. D. M. Todea, "Laser applications in conservative dentistry," *TM Journal,* vol. 54, no. 4, pp. 392-405, 2004.

[23] Types of lasers, Introduction to laser technology, at http://www.mellesgriot.com/pdf/X_36_16-27.pdf, Accessed Feb. 2009.

[24] Z. S. Deng, and J. Liu, "Analytical study on bioheat transfer problems with spatial or transient heating on skin surface or inside biological bodies," *Journal of Biomechanical Engineering*, vol. 124, no. 6, pp. 638-649, 2002.

[25] D. Yang, M. C. Converse, D. M. Mahvi, and J. G. Webster, "Expanding the bioheat equation to include tissue internal water evaporation during heating," *IEEE Transactions on Biomedical Engineering,* vol. 54, no. 8, pp. 1382-1388, 2007.

[26] T. Celik, A. Iyisoy, U. C. Yuksel, B. Jata, B. Bugan, and E. Kardesoglu, "The use of laser angioplasty in patients with acute myocardial infarction: A new era," *International Journal of Cardiology*, Article in Press, 2008.

[27] Diagram of reflection and refraction, Oilfield Glossary, at http://www.glossary.oilfield.slb.com/DisplayImage.cfm?ID=223, Accessed Feb. 2009.

[28] Laser-induced thermotherapy, Optimal control of surface heat treatments, at http://www.wias-berlin.de/publications/annual_reports/2003/node59.html, Accessed Feb. 2009.

[29] Faqs, Heart Disease, at http://www.dmcardiologie.com/faqs.html#, Accessed Feb. 2009.

[30] Laser assisted angioplasty, Peripheral vascular disease: diagnostic and treatment procedures, at http://www.brickcardio.com/pvd_dt.htm, Accessed Feb. 2009.

[31] A. Ravid, D. Simhon, E. Strassman, N. Loya, N. Kariv, T. Brosh, M. Halpern, D. Levanon, and A. Katzir, "Sealing the gap," *SPIE OE Magazine*, pp. 33-35, 2001.

[32] Skin structure diagram, Melanoma: Skin cancer reviewed, at http://melanoma.blogsome.com/category/skin-structure/, Accessed Feb. 2009.

[33] K. Ting, K. T Chen, S. F. Cheng, W. S. Lin, and C. R. Chang, "Prediction of skin temperature distribution in cosmetic laser surgery," *Japanese Journal of Applied Physics,* vol. 47, no. 1, pp. 361-367, 2008.

[34] P. A. Ana, W. F. Velloso, Jr., and D. M. Zezell, "Three - dimensional finite element thermal analysis of dental tissues irradiated with Er,Cr:YSGG laser," *Review of Scientific Instruments,* vol. 79, no. 9, pp. 093910.1-093910.9, 2008.

[35] A. Vogel, J. Noack, G. Huttman, and G. Paltauf, "Mechanisms of femtosecond laser nanosurgery of cells and tissues," *Applied Physics B – Lasers and Optics*, vol. 81, no. 8, pp. 1015-1047, 2005.

[36] V. K. Pustovalov, and B. Jean, "Theoretical investigations of the processes of laser interaction with ocular tissues for laser applications in ophthalmology," *Laser Physics Journal,* vol. 16, no. 8, pp. 1145-1160, 2006.

[37] A. Vogel, and V. Venugopalan, "Mechanisms of pulsed laser ablation of biological tissues," *Chemical Reviews,* vol. 103, no. 2, pp. 577-644, 2003.

[38] R. Dua, S. Chakraborty, "A novel modeling and simulation technique of photo–thermal interactions between lasers and living biological tissues undergoing multiple changes in phase," *Computers in Biology and Medicine,* vol. 35, no. 5, pp. 447-462, 2005.

[39] J. S. Nelson, and J. Applebaum, "Clinical management of port-wine stain in infants and young children using the flashlamp-pulsed dye laser," *Clinical Pediatrics*, vol. 29, no. 9, pp. 503-508, 1990.

[40] B. Greve, and C. Raulin, "Prospective study of port wine stain treatment with dye laser: comparison of two wavelengths (585 nm vs. 595 nm) and two pulse durations (0.5 milliseconds vs. 20 milliseconds)," *Lasers in Surgery and Medicine Journal,* vol. 34, no. 2, pp. 168-173, 2004.

[41] Y. Mohammed, and J. F. Verhey, "A finite element method model to simulate laser interstitial thermo therapy in anatomical inhomogeneous regions," *BioMedical Engineering OnLine,* vol. 4, no. 2, 2005.

[42] L. Brancaleon, and H. Moseley, "Laser and non-laser light sources for photodynamic therapy," *Lasers in Medical Science,* vol. 17, no. 3, pp. 173-186, 2002.

[43] S. L. Marcus, "Photodynamic therapy of human cancer," *Proceedings of the IEEE,* vol. 80, no. 6, pp. 869- 889, 1992.

[44] M. G. Mack, K. Eichler, R. Straub, T. Lehnert, and T.J. Vogl, "MR-guided laser-induced thermotherapy of head and neck tumors," *Medical Laser Application,* vol. 19, no. 2, pp. 91-97, 2004.

[45] U. G. Mueller-Lisse, M. Thoma, S. Faber, A. F. Heuck, R. Muschter, P. Schneede, E. Weninger, A. G. Hofstetter, and M. F. Reiser, "Coagulative interstitial laser-induced thermotherapy of benign prostatic hyperplasia: online imaging with a T2-weighted fast spin-echo MR sequence — experience in six patients," *Radiology,* vol. 210, no. 2, pp. 373-379, 1999.

[46] D. P. O'Neal, L. R. Hirsch, N. J. Halas, J. D. Payne, and J. L. West, "Photo-thermal tumor ablation in mice using near infrared-absorbing nanoparticles," *Cancer Letters,* vol. 209, no. 2, pp.171-176, 2004.

[47] J. A. Parrish, and T. F. Deutsch, "Laser photomedicine," *IEEE Journal of Quantum Electronics*, vol. QE-20, no. 12, pp. 1386-1396, 1984.

[48] A. B. Uzdensky, D. E. Bragin, M. S. Kolosov, and A. A. Zhavoronkova, "PDT effect of different photosensitizers on a single nerve cell: Electrophysiological and pharmacological study," *IEEE Journal on Selected Topics in Quantum Electronics,* vol. 7, no. 6, pp. 989-995, 2001.

[49] K. W. Gregory, and R. R. Anderson, "Liquid core light guide for laser angioplasty," *IEEE Journal of Quantum Electronics,* vol. 26, no. 12, pp. 2289-2296, 1990.

[50] O. J. Ilegbusi, and V. A. Nosovitsky, "A model of blood interaction with optical-fluid guide for laser angioplasty," *Annals of Biomedical Engineering,* vol. 25, no. 4, pp. 653-664, 1997.

[51] M. R. Prince, G. M. Lamuraglia, C. E. Seidlitz, S. A. Prahl, C. A. Athanasoulis, and R. Birngruber, "Ball-tipped fibers for laser angioplasty with the pulsed-dye laser," *IEEE Journal of Quantum Electronics,* vol. 26, no. 12, pp. 2297-2304, 1990.

[52] J. D. Haller, and M. H. Wholey, "The current status of laser angioplasty: coronary and peripheral results," *Proceedings of the IEEE,* vol. 80, no. 6, pp. 861-868, 1992.

[53] N. P. Furzikov, "Different lasers for angioplasty: Thermooptical companson," *IEEE Journal of Quantum Electronics,* vol. QE-23, no. 10, pp. 1751-1755, 1987.

[54] Excimer laser, The free dictionary, at http://medical-dictionary.thefreedictionary.com/excimer+laser, Accessed Feb. 2009.

[55] A. G. Doukas, and T. J. Flotte, "Physical characteristics and biological effects of laser-induced stress waves," *Ultrasound in Medicine and Biology*, vol. 22, no. 2, pp. 151-164, 1996.

[56] K. Takayama, and T. Saito, "Shock wave/Geophysical and medical applications," *Annual Review of Fluid Mechanics*, vol. 36, pp. 347-379, 2004.

[57] J. Marshall, "Thermal and mechanical mechanisms in laser damage to the retina," *Investigative Ophthalmology,* vol. 9, no. 2, pp. 97-115, 1970.

[58] E. J. Dehm, C. A. Puliafito, C. M. Adler, and R. F. Steinert, "Corneal endothelial injury in rabbits following excimer laser ablation at 193 and 248 nm," *Arch Ophthalmology*, vol. 104, no. 9, pp. 1364-1368, 1986.

[59] D. C. Lamb, A. Doukas, T. J. Flotte, R. H. Ossoff, L. Reinisch, and J. Tribble, "Free electron laser as the ideal stress-wave generator," *Proceedings of SPIE*, vol. 2391, pp. 192-201, 1995.

[60] L. Wang, S. L. Jacques, and L. Zheng, "MCML – Monte Carlo modeling of light transport in multi-layered tissues," *Computer Methods and Programs in Biomedicine*, vol. 47, no. 2, pp. 131-146, 1995.

[61] S. A. Prahl, "Light transport in tissue," PhD dissertation, University of Texas, Austin, USA, 1988.

[62] M. Gorjan, "Modelling and measurements of laser-skin thermal interaction," Graduate seminar, University of Ljubljana, Ljubljana, Slovenia, 2008.

[63] S. A. Prahl, D. D. Duncan, and D. G. Fischer, "Monte Carlo propagation of spatial coherence," *SPIE Proceedings on Biomedical Applications of Light Scattering III*, vol. 7187, pp. 71870G-71870G-9, 2009.

[64] D. G. Fischer, S. A. Prahl, and D. D. Duncan, "Monte Carlo modeling of spatial coherence: free-space diffraction," *Journal of the Optical Society of America*, vol. 25, no. 10, pp. 2571-2581, 2008.

[65] P. Kubelka, "New contributions to the optics of intensely light-scattering materials: Part I," *Journal of the Optical Society of America,* vol. 38, no. 5, pp. 448–457, 1948.

VITA

RAKESH CHOULA

Contact: (219)218-8132
E-mail: rakeshchoula@gmail.com

EDUCATION

- **Master of Science** in Electrical and Computer Engineering
  Old Dominion University, Norfolk, VA
  December 2009, GPA – 3.71/4.0
- **Bachelor of Technology** in Electronics and Communications Engineering
  Jawaharlal Nehru Technological University, Hyderabad, India
  May 2007, Percentage – 75.46%

INTERESTS

Modeling and Simulation, Digital Signal Processing, Digital Communications, and Programming in MATLAB, C, and C++.

TECHNICAL SKILLS

Languages: C, C++, FORTRAN
Tools: MATLAB & Simulink, VHDL, PSPICE
Web Technologies: Java Script, HTML, XML
Operating Systems: Windows 95/98/NT/XP/VISTA, UNIX, MS-DOS
Packages: MS-Word, MS-PowerPoint, MS-Excel

WORK EXPERIENCE

- **Graduate Research Assistant** Jan 2008 – Dec 2009
Department of Electrical and Computer Engineering, ODU
- **Graduate Assistant** Jan 2009 – Aug 2009
Experiential Learning and Testing Center, ODU
Role: The main responsibility is to administer Placement tests (WSPT, COMPASS Math, Foreign Language and EXIT exam), Correspondence tests, National tests (CLEP and DANTES) and Admissions tests (Miller Analogy).
- **Graduate Assistant** Jan 2008 – Dec 2008
Athletic Academic Center, ODU
Role: Guiding and assisting athletic students on their C, C++, and MATLAB projects. Tutoring Mathematics, Statistics, Physics and Chemistry courses.
- **Research Associate** Aug 2007 – Dec 2007
Sentara Emergency Study Project, ODU
Role: The primary responsibility of a Research Associate is to interview patients and to gather data from them for the Sentara Emergency Department.